Johannes Gutenberg-Universität Mainz

Numerical modeling of magma ascent through the lithosphere

Dissertation
zur Erlangung des Grades
Doktor der Naturwissenschaften
im Promotionsfach Geologie/Paläontologie

am Fachbereich Chemie, Pharmazie, Geographie und Geowissenschaften
der Johannes Gutenberg-Universität Mainz

Nicolas Berlie

geboren in Genf, Schweiz

Mainz, 2023

1. Berichterstatter: Prof. Dr. Boris J. P. Kaus

Tag der mündlichen Prüfung: 08.11.2023

Abstract

Magmatic systems and volcanoes are found throughout the entire world, yet the processes responsible for the ascent of magmatic melt, as well as the structure of these systems, are still poorly constrained due to a lack of direct observations. All hypotheses in this field are derived from indirect observations (geophysical surveys, fieldwork and petrological studies on fossil exhumed systems or at the surface of currently active volcanic systems) and robust physical and geochemical models need to be developed to validate, quantify or refine these ideas. We address these challenges in this thesis in two parts.

First, we study the melt depletion of a magmatic reservoir connected to the surface by a weak conduit. Using a 2D model, we simplify the rheology and structure of the system to a few parameters and determine how sensitive the velocities within the conduit are to variations in these parameters. Several modes of transport are identified and translated into analytical scaling laws. We then apply these scaling laws to the 2021 eruption of the Cumbre Vieja volcano to constrain the structure of the magmatic system located beneath La Palma in the Canary Islands.

Second, we develop tools to model magmatic systems in more detail and in a self-consistent manner across the lithosphere. One of these tools is an extension of the numerical continuum approach commonly used in geodynamics to model both shear and tensile plastic failure. This enables us to include dykes, the main form of melt transport in the elasto-plastic upper crust, in our models. The constitutive equations presented include compressible visco-elasto-plasticity with viscoplastic regularization and non-linear rheologies. A new yield function, adapted to work reliably in tensile conditions without introducing unphysical stress states into the model, is also presented. Another tool described in this thesis is MAGEMin, a Gibbs energy minimizer applied to igneous systems. MAGEMin is an efficient and highly scalable minimization package that opens up new possibilities for petrological applications as well as for use in conjunction with thermomechanical models. It uses a combination of linear programming, extended Partitioning Gibbs Energy and gradient-based minimization. The implementation of the thermodynamic dataset (Holland et al., 2018) was benchmarked against THERMOCALC.

Kurzfassung

Magmatische Systeme und Vulkane sind auf der ganzen Welt zu finden, doch die Prozesse, die für den Aufstieg magmatischer Schmelze verantwortlich sind, sowie die Struktur dieser Systeme sind aufgrund mangelnder direkter Beobachtungen noch immer nur unzureichend geklärt. Alle Hypothesen in diesem Bereich werden aus indirekten Beobachtungen abgeleitet (geophysikalische Untersuchungen, Feldarbeit und petrologische Studien an fossilen exhumierten Systemen oder an der Oberfläche derzeit aktiver Vulkansysteme), und es müssen robuste physikalische und geochemische Modelle entwickelt werden, um diese Ideen zu validieren, zu quantifizieren oder zu verfeinern. Wir gehen diese Herausforderungen in dieser Arbeit in zwei Teilen an.

Zunächst untersuchen wir die Schmelzeentleerung eines magmatischen Reservoirs, das durch einen schwachen Schlot mit der Oberfläche verbunden ist. Mithilfe eines 2D-Modells vereinfachen wir die Rheologie und die Struktur des Systems auf einige wenige Parameter und bestimmen, wie empfindlich die Geschwindigkeiten innerhalb des Kanals auf Variationen dieser Parameter reagieren. Es werden mehrere Transportmodi identifiziert und in analytische Skalierungsgesetze übersetzt. Anschließend wenden wir diese Skalierungsgesetze auf den Ausbruch des Vulkans Cumbre Vieja im Jahr 2021 an, um die Struktur des magmatischen Systems unter La Palma auf den Kanarischen Inseln einzugrenzen.

Zweitens entwickeln wir Instrumente, um magmatische Systeme in der gesamten Lithosphäre detaillierter und in sich konsistenter Weise zu modellieren. Eines dieser Werkzeuge ist eine Erweiterung des in der Geodynamik üblichen numerischen Kontinuum-Ansatzes zur Modellierung von plastischem Scher- und Zugversagen. Dies ermöglicht es uns, Dykes, die Hauptform des Schmelztransports in der elasto-plastischen oberen Kruste, in unsere Modelle einzubeziehen. Die vorgestellten konstitutiven Gleichungen beinhalten kompressible Visko-Elasto-Plastizität mit viskoplastischer Regularisierung und nichtlinearen Rheologien. Außerdem wird eine neue “yield function"vorgestellt, die so angepasst ist, dass sie unter Zugbedingungen zuverlässig funktioniert, ohne unphysikalische Spannungszustände in das Modell einzubauen. Ein weiteres in dieser Arbeit beschriebenes Werkzeug ist MAGEMin, ein Gibbs-Energie-Minimierer, der auf magmatische Systeme angewendet wird. MAGEMin ist ein effizientes und hoch skalierbares Minimierungspaket, das neue Möglichkeiten für petrologische Anwendungen sowie für den Einsatz in Verbindung mit thermomechanischen Modellen eröffnet. Es verwendet eine Kombination aus linearer Programmierung, erweiterter Partitioning Gibbs Energy und gradientenbasierter Minimierung. Die Implementierung des thermodynamischen Datensatzes (Holland u. a., 2018) wurde mit

THERMOCALC verglichen und getestet.

Contents

List of Figures

List of Tables

List of Abbreviations

PDE	Partial Differential Equation
yrs	years
MPa	megapascal (10^6 Pa)
0D	zero-dimensional
2D	two-dimensional
3D	three-dimensional

Chapter 1

Introduction

1.1 Motivation

The ascent of magma in the Earth's crust is a fundamental geological process, responsible for both the formation of new crust (Piccolo et al., 2019) and volcanism around the globe. It is also a subject of study that involves many geological disciplines, including field studies, petrology, geochemistry and geophysics, as well as analog and numerical modeling. While the first methods can provide data support hypotheses about how magmatic systems form and evolve, modeling can provide physical constraints to test these hypotheses and organize information from different fields into a coherent model.

Generally accepted conceptual models of the structure of magmatic systems have evolved greatly in recent years, from melt-dominated transcrustal volumes to large, long-lived, highly crystallized magmatic reservoirs containing smaller volumes of magmatic melt for shorter intervals of time (see Bachmann and Bergantz, 2004; Hildreth, 2004; Bachmann and Huber, 2016). The modeling of such systems presents several new challenges that the ERC project MAGMA aims to address. The objectives of the project are: to create new computer models to simulate two-phase flow through a deforming visco-elasto-plastic medium using both shear and tensile plasticity; to perform systematic numerical simulations to better understand the physics of these models and compare them with observations; to develop new approaches to calculate thermodynamic equilibria in a faster and more reliable way; to perform inverse geodynamic modeling of active magmatic systems.

As part of this project, this thesis focuses on three of these goals. The performance of modern computers and access to supercomputer clusters allow us to run several thousand 2D mechanical models in a very short time. This gives us the opportunity to explore the parameter space of a simple model setup and to gain a better understanding of the physical processes governing the dynamics of our simplified system before adding more complexity. Additionally, we work on the development and testing of suitable numerical methods for both the mechanical aspect of modeling magmatic systems and the geochemical aspect of solving for thermodynamic equilibrium. Since the author of this thesis was not the main contributor to the thermodynamic part of the study, it has been included in the appendix.

This work aims to improve our understanding of how magma moves from the mantle to the crust. To achieve this goal, it seeks to introduce new elements into the broader geodynamic framework that we consider essential for creating self-consistent models that accurately describe the dynamics of magmatic systems.

1.2 Thesis structure

This thesis will be structured into two main chapters (chapters 2 and 3), followed by a short summary and conclusion chapter (chapter 4), and an appendix.

Chapter 2: *The dynamics of magma withdrawal in volcanic chambers*

This chapter explores a new method for investigating the architecture of a transcrustal magmatic plumbing system using the dynamics of a volcanic eruption. A simplified volcanic system is modeled in 2D using a finite element code with structural and rheological parameters, allowing a systematic exploration of the parameter space. The sensitivity of the melt flow in the volcanic conduit as a function of each parameter is then presented in three scaling laws describing three different advection regimes. Finally, an application of these scaling laws to the Cumbre Vieja volcano is discussed.

Chapter 3: *A numerical method to solve compressible visco-elasto-plastic systems including shear and tensile plasticity*

The coupling of dyke propagation models with ductile rheologies is a necessary step for the study of transcrustal magmatic systems using numerical models. This chapter presents the derivation and implementation of a tensile plastic rheology suitable for modeling dyking in a visco-elastic-plastic host rock, and an adapted composite yield criterion. The derivations are presented in detail, followed by the numerical implementation method and a demonstration of 0D and 2D cases. Finally, the outlook for the applicability of this method is discussed. The rheology includes rock compressibility, nonlinear viscous and plastic constitutive equations and the viscoplastic regularization of the system.

Chapter 4: *Conclusions*

This chapter summarises the findings of chapters 2 and 3. Concluding remarks are given, as well as a general outlook for the future of magmatic systems study, the next necessary developments, and recontextualises the advances presented in this work.

Appendix *MAGEMin, an Efficient Gibbs Energy Minimizer: Application to Igneous*

Systems

This chapter presents a new Mineral Assemblage Gibbs Energy Minimizer (MAGEMin), which has been developed to predict stable mineral equilibria reliably and efficiently, in view of coupling it with thermomechanical codes. A comprehensive review of currently used methods and their respective shortcomings is given, followed by an explanation of the Gibbs energy formulation and the new Gibbs energy minimization strategy. A demonstration of the code and some applications are then presented. Finally, the consistency of the method and a method for coupling MAGEMin to a geodynamic model are discussed, together with some future prospects.

1.3 Derivation of the stiffness matrix

This thesis investigates the use of numerical modeling to study magmatic processes along two main axes. One axis involves extracting knowledge from a simple mechanical model of a magmatic system. Incompressible Stokes equations are solved in two dimensions for a single time-step using a linear viscous rheology. The complexity of the system's configuration is summarised into a few geometrical parameters and the constitutive equations for the rheology are condensed into a single viscosity value. This model is detailed in chapter 2, along with the methodology used to derive analytical scaling laws from simulation results.

In contrast, chapter 3 employs complex rheologies with multiple sources of non-linearity to model the propagation of dykes. To gradually increase the complexity of tested flow laws and steadily build the implementation, the initial development stages tested various methods for deriving the stiffness matrix associated with the partial differential equations. The following paragraphs present some of the tested methods that did not feature in the implementation outlined in chapter 3.

1.3.1 Picard stiffness matrix

Picard iterations use a quasi-linear form of the residual equation $\boldsymbol{f}(\boldsymbol{x})$ to evaluate the solution $\boldsymbol{x}$ of the next iteration:

$$\boldsymbol{f}(\boldsymbol{x}) = \boldsymbol{A}(\boldsymbol{x})\boldsymbol{x} - \boldsymbol{b} = 0, \tag{1.1}$$

$$\boldsymbol{x}_{k+1} = \boldsymbol{A}(\boldsymbol{x}_k)^{-1}\boldsymbol{b}, \tag{1.2}$$

where $\boldsymbol{A}(\boldsymbol{x})$ is the Picard matrix, $\boldsymbol{b}$ is the right-hand side of the residual function and k is the iteration number. Although the convergence rate of Picard iterations tends to be linear in the best cases (against quadratic for Newton-Raphson iterations), this stiffness matrix is often much easier to compute than the Jacobian and can be useful to test the implementation of new flow laws in the residual functions.

1.3.2 Using Automatic Differentiation tools to compute the global Jacobian matrix

As mentioned above, Newton-Raphson iterations tend to converge way faster to the solution to a partial differential equation. However, This method requires a Jacobian matrix computed from the derivatives of the conservation equations over each primary variable (velocity and pressure):

$$J_{ij} = \frac{\partial f_i}{\partial x_j}. \tag{1.3}$$

This Jacobian can be computed using numerical methods or analytically. The first option requires some additional computational time and possibly a reduced accuracy, while the second has to be re-derived and adapted for each modification of the constitutive equations, sometimes by investing a significant amount of time.

During part of the development phase of the work presented in chapter 3, we computed the Jacobian needed by the global solver using an automatic differentiation method. This method takes advantage of the fact that our residual function, however complex, can be decomposed as a simple sequence of arithmetic operations and elementary functions, as can the derivatives of that function. The main principle of automatic differentiation is therefore to decompose the function and its derivatives using the chain rule to automatically generate an analytical formula.

We use tools from the ForwardDiff.jl package developed by Revels et al. (2016). This package implements in Julia a representation of multidimensional dual numbers. Dual numbers are a complex number system similar to imaginary numbers (Khan and Barton, 2015). They are expressions of the form:

$$z = x + y\epsilon, \tag{1.4}$$

where (x, $y \in R$) and $\epsilon^2 = 0$, and their behavior in scalar functions is defined as:

$$f(x + y\epsilon) = f(x) + f'(x)\, y\epsilon. \tag{1.5}$$

They are very useful for computing scalar derivatives and can be extended to a multidimensional dual number to treat functions of vectors like the residual functions we are concerned with. In ForwardDiff they are formulated as:

$$\boldsymbol{x} = \begin{bmatrix} x_1 \\ \vdots \\ x_i \\ \vdots \\ x_k \end{bmatrix} \rightarrow \boldsymbol{x}_\epsilon = \begin{bmatrix} x_1 + \epsilon_1 \\ \vdots \\ x_i + \epsilon_i \\ \vdots \\ x_k + \epsilon_k \end{bmatrix} \rightarrow \boldsymbol{f}(\boldsymbol{x}_\epsilon) = \boldsymbol{f}(\boldsymbol{x}) + \sum_{i=1}^{k} \frac{\partial \boldsymbol{f}(\boldsymbol{x})}{\partial x_i} \epsilon_i. \tag{1.6}$$

This method has the advantage of requiring much less evaluation of the residual

function to compute a Jacobian matrix than other numerical methods while guaranteeing an accuracy equivalent to an analytical formulation. For a simple case, the residual function would be called only a few times, but for larger or more complex systems, the process can be broken into chunks and run on multiple threads. The process can however have an important cost in memory and allocations and an analytical formulation such as the one formulated in chapter 3 will be faster and more memory efficient.

1.4 Author contributions

Chapter 2: *The dynamics of magma withdrawal in volcanic chambers* - N. Berlie, B. J. P. Kaus

NB developed the concept as well as the methodology of the work, performed the modeling, derived the scaling laws, created the figures and wrote the manuscript. BJPK contributed to the concept and methodology of the work. He also provided reviews to the manuscript and acquired project funding.

Chapter 3: *Velocity-Pressure formulation to solve a compressible visco-elasto-plastic system including shear and tensile plasticity* - N.Berlie, A. Popov, B.J.P. Kaus, D. Kiss

NB developed the concept and the methodology for this work, performed the modeling, created the figures and wrote the manuscript. AP contributed to the equations derivation, to the implementation and the modeling. He also reviewed and edited the manuscript. BJPK contributed to the concept of the study and the methodology, he also reviewed and edited the manuscript. DK contributed to the methodology and reviewed and edited the manuscript.

Appendix *MAGEMin, an Efficient Gibbs Energy Minimizer: Application to Igneous Systems* - N. Riel, B.J.P. Kaus, E.C.R. Green, N. Berlie

NR developed the concept and created the methodology for this work. He also implemented the method and the database, created the figures and wrote the manuscript. BJPK contributed to the concept and method. He also reviewed and edited the manuscript. ECRG contributed to the concept of this work and the implementation of the database as well as reviewed and edited the manuscript. NB contributed to the concept of this work and the implementation of the database as well as reviewed and edited the manuscript.

1.5 Software

All of the modeling in this thesis has been performed in the *Python* and *Julia* language, using the *Visual Studio Code*, *Spyder* and *Jupyter Notebook* editors. This manuscript was written on *ShareLaTeX/Overleaf* using the "Master/Doctoral Thesis" template from `www.latextemplates.com`. The results visualization was done in *Paraview* or directly on the visualization packages from *Python* (*matplotlib*) and *Julia* (*Plots* and *Makie*). *Inkscape* was used to create and edit figures. Other software used are mentioned directly in the chapters.

Chapter 2

The dynamics of magma withdrawal in volcanic chambers

Abstract

Understanding magmatic plumbing systems across the lithosphere is still one of the major challenges in geosciences. This is mainly due to the limited resolution of geophysical data at relevant depths and the rare instances of exposed sections of the deep magmatic crust. We address this problem by investigating how efficiently a magma reservoir can be depleted during an eruption and how geophysical and petrological information can be integrated into a simple numerical model using analytical scaling laws. We proceed here using a 2D finite element code written in Julia. The results show that there are several modes of magma transport. Firstly, the pipe flow mode, where the melt flows through the volcanic conduit can be described by a classical pipe flow formula. Secondly, the plume-driven flow mode, where magma transport mimics the rise of a plume in a viscous medium, and lastly the convection-dominated flow mode, where most of the magma displacement is constrained in the magma chamber rather than in the volcanic conduit. We use numerical simulations to determine how magma ascent velocities are controlled by material and geometric properties such as magma and mush viscosities, magma and mush chamber radius, or dike widths. To improve our understanding of these relationships, and to apply our results to realistic magma viscosities despite the inherent limitations of numerical modeling, we use our numerical results to derive scaling laws characterizing melt advection regimes. We then apply the scaling laws on a geological case study, the Cumbre Vieja 2021 eruption on La Palma.

2.1 Introduction

In recent years it has been recognized that volcanic edifices do not generally have a unique magmatic chamber feeding them, but rather consist of lithospheric scale plumbing systems of interconnected magma reservoirs (Cashman et al., 2017). Most of the plumbing system will exist in a partially molten state ("mush"), with intermittent fully molten sills interconnecting them. However, because direct observation is not

possible, there are only few constraints on the rheology of these mushes, as well as the precise geometry and connectivity of potential molten sills present in large volcanic chambers (Lees, 2007; De Siena et al., 2014).

Using a combination of fieldwork, rock analysis and numerical modeling, previous studies have constrained the size and injection rate of sills in several current or fossil magmatic systems (Coleman et al., 2004; Annen et al., 2008; Michel et al., 2008; Schmitt et al., 2023). The rheology of the mush and the mechanics behind magma ascent to the surface are also being actively investigated (Mark Jellinek and DePaolo, 2003; Papale et al., 2017) as well as the effect of caldera collapse (Acocella et al., 2004; Kennedy et al., 2008; Gregg et al., 2012) or the influence of regional faults on magmatic systems (Novoa et al., 2022; Ruz-Ginouves et al., 2021). The importance of buoyancy as a trigger or consistent driving force for melt displacement also remains an open question (Gregg et al., 2015; Papale et al., 2017).

Which mechanism controls the dynamics of a magma chamber after the initial trigger of an eruption? Can buoyancy sustain the eruptive system after most of the gas has been removed from the system? In this paper, we investigate the importance of magma rheology and the structure of the magma chamber on eruption rates, the criteria under which eruptions stop, and the rate at which magma is transported to the surface. We first perform simulations of a simplified volcanic setting, with a sill of pure melt enclosed at the top of a magma chamber and connected to the surface by a weak vertical conduit. After recovering conduit velocities from these models, we identify the key mechanical processes acting on the system and characterize them in three analytical scaling laws. In the following section, we discuss the application of these scaling laws to the 2021 eruption of the Cumbre Vieja volcano of La Palma, Spain.

2.2 Numerical model

We use the computational framework Gridap (Badia and Verdugo, 2020; Verdugo and Badia, 2022) to solve the mass and momentum conservation equations in 2D using the finite element method (FEM). This package is written in the Julia programming language and provides tools enabling us to automatically discretize differential equations from their weak form and the model setup (grid, boundary conditions, phases and material parameters). We used it to build a model solving the incompressible Stokes equations:

$$\nabla \cdot \boldsymbol{u} = 0, \tag{2.1}$$

$$\nabla \cdot 2\eta \dot{\boldsymbol{\varepsilon}}(\boldsymbol{u}) - \nabla p + \rho \boldsymbol{g} = 0, \tag{2.2}$$

where $\boldsymbol{u}$ is the velocity vector, $\boldsymbol{g}$ is the gravity vector, p is the pressure, ρ is the density, η is the viscosity and $\dot{\boldsymbol{\varepsilon}} = \frac{1}{2}((\nabla \boldsymbol{u})^T + \nabla \boldsymbol{u})$ is the strain rate. We reformulate these

two equations using an abstract framework into a weak form suitable for use with the finite element method to find $(\boldsymbol{u}, p) \in W$ such that:

$$a((\boldsymbol{u}, p), (\boldsymbol{v}, q)) = l((\boldsymbol{v}, q)), \tag{2.3}$$

for all $(\boldsymbol{v}, q) \in W$ where

$$a((\boldsymbol{u}, p), (\boldsymbol{v}, q)) = 2\eta \int_\Omega \dot{\boldsymbol{\varepsilon}}(\boldsymbol{u}) : \dot{\boldsymbol{\varepsilon}}(\boldsymbol{v}) \mathrm{d}\Omega - \int_\Omega \nabla \cdot \boldsymbol{v} p \mathrm{d}\Omega + \int_\Omega \nabla \cdot \boldsymbol{u} q \mathrm{d}\Omega, \tag{2.4}$$

$$l((\boldsymbol{v}, q)) = \int_\Omega \rho \boldsymbol{g} \cdot \boldsymbol{v} \mathrm{d}\Omega, \tag{2.5}$$

the space $W = V \times Q$ being a mixed function space such that $(\boldsymbol{u}, \boldsymbol{v}) \in V$ and $(p, q) \in Q$.

The model setup as well as the unstructured rectangular mesh are set and generated using the Julia API Gmesh (Remacle et al., 2012). A circular magma chamber is situated within a larger mushy region in the upper crust and is linked to the surface through a weak conduit (our vent). This follows the conceptual models of Hildreth and Wilson (2007), Sparks and Cashman (2017), and Cashman et al. (2017). Figure 2.1 shows the dimensions and geometrical features of the modeled space, as well as an example of an unstructured grid.

In order to obtain an applicable set of scaling laws, we reduce the system's complexity (multiphase interactions, temperature dependence, phase transitions) into a select few constant parameters as listed in table 2.1. We also assume that most volatiles have been extruded early on in the eruption event and thus produce a negligible overpressure in the magma chamber once the eruption proceeds. Accordingly, buoyancy is the main driving factor for displacements.

TABLE 2.1: Model parameters

Parameter	Range and units	Description
$\Delta\rho$	300-700 [kg m^{-3}]	Density contrast between the melt and the mush ($\rho_{\text{melt}} - \rho_{\text{mush}}$)
η_{melt}	10^{13} - 10^{19} [Pa s]	Viscosity of the melt
η_{mush}	10^{18} - 10^{22} [Pa s]	Viscosity of the mush
η_{crust}	10^{22} [Pa s]	Viscosity of the crust
L	1500 - 15000 [m]	Length of the conduit
W	50 - 200 [m]	Width of the conduit
R_{melt}	1500 - 3500 [m]	Radius of the melt pocket
R_{mush}	3500 - 15000 [m]	Radius of the mush

2.3 Results and scaling laws determination

To determine the relationship between each parameter and the rate of material moving through the conduit, we systematically performed simulations varying each parameter and plotted the resulting vertical velocities in the conduit. Although the variation of

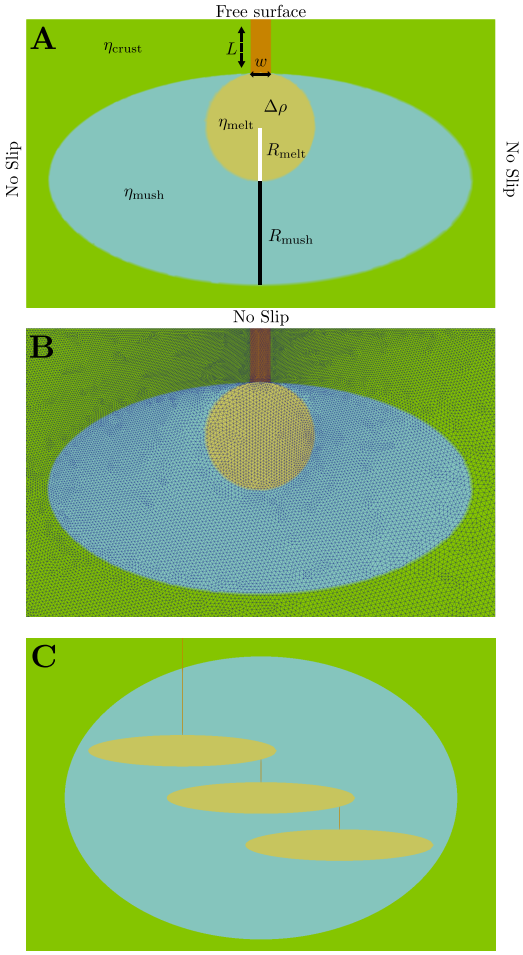

FIGURE 2.1: 2-D model setup. Dirichlet no-slip boundaries are assigned to the right, left and bottom of the model while the top is left as a free surface. A: The box is 60 km wide and 40 km deep in total. The melt pocket is situated at the top of the mush system and connected to the surface by a conduit. The mush chamber is surrounded by a rigid host rock (the upper crust). the parameters listed in table 2.1 are also described on the setup. Even though the mush chamber is elliptical, we maintain a constant aspect ratio such that we can describe its size with a single parameter. B: The mesh is refined in the area of the melt pocket and the channel. C: A configuration with several interconnected melt pockets is also considered to observe the dynamics of such a system.

some parameters affects the whole system dynamics and not just the conduit velocity (e.g. the vertical rise of the melt pocket inside the mush chamber), we limit our observations to this metric as it gives us an insight into the magmatic material that could eventually reach the surface. Figure 2.2 shows an example for different values of mush viscosity while all other model parameters, including geometry, are fixed. A profile of vertical velocity at the center of the model (Fig. 2.2A) shows that the velocity in the conduit is inversely proportional to the mush viscosity. For a mush viscosity of 10^{20} Pas, the magma batch within the mush chamber starts rising as a convective sphere with a maximum vertical velocity that is larger than the conduit velocity (Fig. 2.2B left). For the other two simulations, this is not the case and results in slightly smaller conduit velocities. This is because a lower mush viscosity implies that the mush can deform more easily and thus fill the space of the moving melt. If

the mush viscosity increases, on the other hand, it hampers the motion of the magma chamber and therefore reduces the conduit velocity.

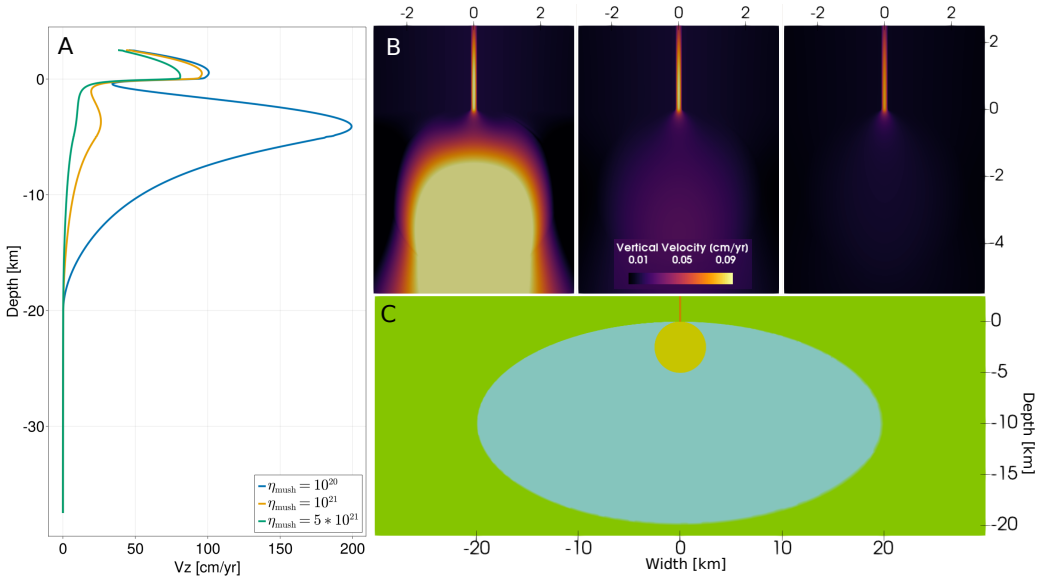

FIGURE 2.2: Visualisation of three models with three different effective mush viscosities: 10^{20}, 10^{21} and 5×10^{21} Pa s while keeping the other parameters constant: $\Delta\rho = 500$ [kg m^{-3}], $\eta_{\text{melt}} = 10^{18}$ [Pa s], $L = 2500$ [m], $W = 200$ m, $R_{\text{melt}} = 2500$ m and $R_{\text{mush}} = 10000$ m. A: Vertical velocity profile from top to bottom of the model at the center of the model (Width=0 km). Reducing the viscosity of the mush causes movement in the melt pocket and increases the melt velocity into the channel as well. B: 2D visualization of the vertical velocity. The mush chamber deforms and allows the entire melt pocket to rise. C: General layout of the models: The host rock (the upper crust) is green, the mush chamber blue, the melt pocket yellow and the conduit is red.

Whereas this is a simple example, most of the other model parameters also influence the conduit velocities. The conduit velocity itself is not constant, but maximum at the bottom and decreasing towards the top, which is because we set the density of the material within the conduit to be the density of the surrounding crust, to eliminate an additional buoyancy source and obtain a lower bound for the conduit velocity. This maximum conduit velocity, $v_{\text{z,max}}$ is thus potentially a function of all model parameters:

$$v_{\text{z,max}} = f(\Delta\rho, \eta_{\text{melt}}, \eta_{\text{mush}}, L, W, R_{\text{melt}}, R_{\text{mush}}). \tag{2.6}$$

We therefore systematically varied each of the parameters to quantify the relative impact of each parameter on $v_{\text{z,max}}$. If there is a relationship between the parameters, quantifying this relationship can be done by plotting $\log_{10}(v_{\text{z,max}})$ versus $\log_{10}(\text{parameter})$. The slope of a linear fit gives the power law exponent. For example, figure 2.3A shows the effect of $\Delta\rho$ on $v_{\text{z,max}}$, which is:

$$\begin{aligned} \log_{10}(v_{\text{z,max}}) &\propto 1.0000000000000146 \log_{10}(\Delta\rho), \\ v_{\text{z,max}} &\propto \Delta\rho^{1.0000000000000146}, \end{aligned} \tag{2.7}$$

which is thus, as expected, linear. In other cases, these relationships are not quite as straightforward and there are different analytical expressions depending on where in the parameter space we are. Increasing the conduit width W, for example, increases the conduit velocity until a maximum is reached and the velocity decreases again (figure 2.3C). The dynamics of the magmatic fluid change at this point from a pipe flow to something more akin to a rising plume, losing velocity as it does so. Similarly, η_{mush} does not correlate with the conduit velocity at low values but begins to negatively affect this velocity at a certain threshold (figure 2.3D). The melt velocity is thus constrained by other parameters before this threshold, which shows another transition between two melt dynamics regimes as a function of mush viscosity.

Each of these exercises can be repeated for all model parameters until a full scaling law is derived. For cases in which we have two different regimes (such as in figure 2.3D), we need to repeat this within each of the distinct regimes (the "low viscosity" and "high viscosity" regimes, respectively).

We performed this for all model parameters and could identify three main regimes for magma conduit velocities, associated with three different scaling laws. These scaling laws are summarized in table 2.2. The scaling law exponents of each parameter have been kept as close as possible to the numerical data while maintaining a consistency in unit. We have also added a constant coefficient to each scaling law to improve the fit with the data.

A summary in which the predicted velocities are compared with the numerically computed values shows that we have a general quite good agreement and velocities are generally within 10 percent for the first and third scaling law and 25 percent for the second (figure 2.4)).

The velocity in all regimes is proportional to $\Delta\rho g$, which is to be expected as buoyancy is the main driving force in the system. In all cases, a larger radius of the melt batch increases the conduit velocity as well, but in different ways. Yet, there are also clear differences. It is interesting to determine the dominant flow mode at different conditions. For this, we can determine boundaries between the different flow regimes, which occur when the velocity of a regime is equal to that of another. A summary of that is given in table 2.3 and showed on figure 2.5, which splits the parameter space between the rheological parameters (the ratio between the melt and the mush viscosity) and the geometrical parameters of the mush chamber, melt pocket and melt conduit.

The first regime dominates for a high $\frac{L}{R}$ ratio and a high $\frac{\eta_{\text{mush}}}{\eta_{\text{melt}}}$ ratio. We call this "pipe flow regime". Under these conditions, the velocity in the conduit increases with the width of the conduit and decreases with its length, similar to the classical pipe flow formula in fluid dynamics. A significant difference, however, is the equal importance of the viscosity of the mush relative to the viscosity of the melt, since any flow into the conduit must be extracted from the magma chamber and this change in volume must be accommodated by the surrounding mush. The resulting formula is

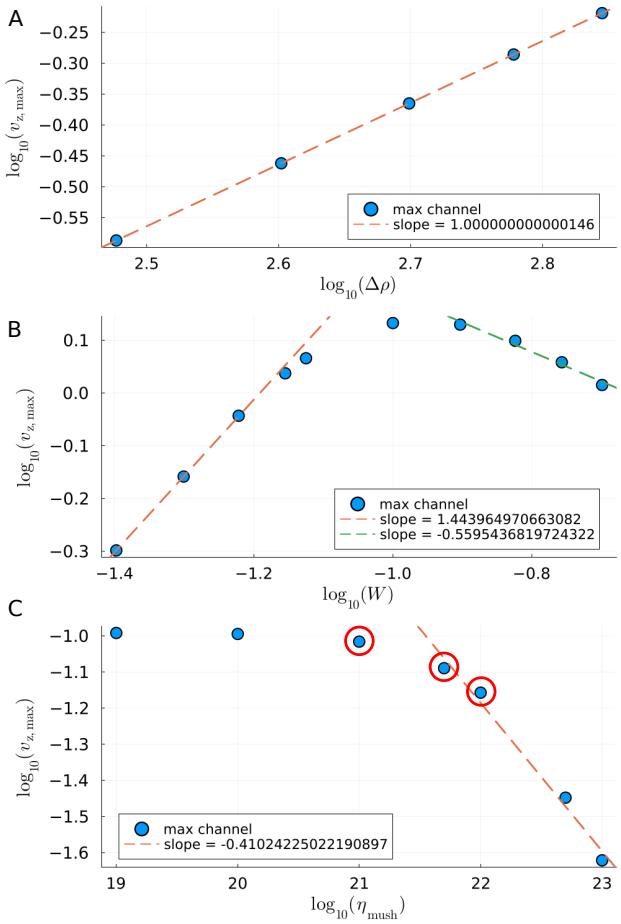

FIGURE 2.3: Maximum vertical velocity in the conduit as a function of several parameters on the logarithmic scale: A: The density contrast between the melt and the surrounding rocks correlates directly with the velocity, B: The length of the conduit correlates negatively with the velocity for this set of parameters, C: The relationship between the width of the conduit and the velocity shows two different trends, one positive and one negative, indicating two different advection regimes, D: The viscosity of the melt has no correlation with the velocity at a low value and a negative one at a higher value. The three data points circled in red are the models shown in figure 2.2, at a transition between two regimes.

$$v_{\text{z,max}} = C_1 \frac{W R_{\text{melt}}^{1.5} \Delta\rho g}{L^{0.5} \eta_{\text{melt}}^{0.5} \eta_{\text{mush}}^{0.5}}. \tag{2.8}$$

The second regime dominates for a low $\frac{L}{R}$ ratio and a high $\frac{\eta_{\text{mush}}}{\eta_{\text{melt}}}$ ratio. We call this "plume-driven regime". Under these conditions, the importance of the mush viscosity becomes greater than the melt viscosity, similar to the tip of a rising plume. The length of the conduit becomes irrelevant to the dynamics of the melt and the width of the conduit is negatively correlated with the velocity in the conduit. The formula of the plume-driven regime is

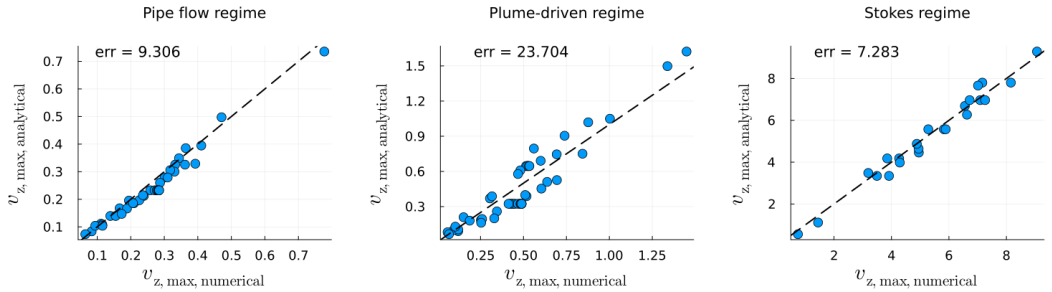

FIGURE 2.4: Comparison between the modeled velocities and the ones computed using the scaling laws, all data points are well aligned, confirming that the parameters chosen are exhaustive enough to represent all the model complexity.

$$v_{\mathrm{z,max}} = C_2 \frac{R_{\mathrm{melt}}^{2.5} \Delta\rho g}{W^{0.5} \eta_{\mathrm{melt}}^{0.3} \eta_{\mathrm{mush}}^{0.7}}. \tag{2.9}$$

The third regime occurs at low $\frac{\eta_{\mathrm{mush}}}{\eta_{\mathrm{melt}}}$ ratios. We call this "convection-driven regime". In this case, the highest velocities in the model are concentrated in the melt pocket rather than in the conduit. Most of the buoyancy in the system is thus used in the internal mixing of the mush chamber and only a limited amount of material makes it to the surface. Since the mush deforms to a similar viscosity to the melt itself, the melt viscosity becomes the most important parameter to consider. Since most of the fluxes now take place in the mush chamber, its geometry becomes more important than the one of the magmatic conduit. We introduce then as a parameter the radius of the mush chamber and remove the length of the conduit. The corresponding formula is:

$$v_{\mathrm{z,max}} = C_3 \frac{W R_{\mathrm{melt}} R_{\mathrm{mush}} \Delta\rho g}{L \eta_{\mathrm{melt}}}. \tag{2.10}$$

TABLE 2.2: Numerically determined scaling laws

	scaling law	
Regime 1: pipe flow	$V_{\mathrm{channel}} = C_1 \frac{W R_{\mathrm{melt}}^{1.5} \Delta\rho g}{L^{0.5} \eta_{\mathrm{melt}}^{0.5} \eta_{\mathrm{mush}}^{0.5}}$	$C_1 = 1.7$
Regime 2: plume-driven	$V_{\mathrm{channel}} = C_2 \frac{R_{\mathrm{melt}}^{2.5} \Delta\rho g}{W^{0.5} \eta_{\mathrm{melt}}^{0.3} \eta_{\mathrm{mush}}^{0.7}}$	$C_2 = 15e-2$
Regime 3: convection-driven	$V_{\mathrm{channel}} = C_3 \frac{W R_{\mathrm{melt}} R_{\mathrm{mush}} \Delta\rho g}{L \eta_{\mathrm{melt}}}$	$C_3 = 18e-4$

2.4 Discussion

2.4.1 The last phase of an eruption

Next, we will look at potential applications of these scaling laws. Of particular interest is understanding the conditions for an eruption to stop. The end of an eruption occurs when the flow of magmatic material in a volcanic vent stops. This could happen if the

TABLE 2.3: Regime boundaries

regime boundary	expression
Regime 1-2	$\frac{\eta_{\text{mush}}}{\eta_{\text{melt}}} = \left(\frac{\frac{C_2}{C_1} R_{\text{melt}} L^{0.5}}{w^{1.5}} \right)^5$
Regime 1-3	$\frac{\eta_{\text{mush}}}{\eta_{\text{melt}}} = \left(\frac{\frac{C_1}{C_3} R_{\text{melt}}^{0.5} L^{0.5}}{R_{\text{mush}}} \right)^2$
Regime 2-3	$\frac{\eta_{\text{mush}}}{\eta_{\text{melt}}} = \left(\frac{\frac{C_2}{C_3} R_{\text{melt}}^{1.5} L}{w^{1.5} R_{\text{mush}}} \right)^{\frac{10}{7}}$

magma inside the conduit solidifies faster than it rises. For this to happen, we need the residence time of the magma in the conduit (t_{adv}) to be of the same order as the typical cooling time of the magma by heat diffusion (t_{cooling}). t_{adv} can be estimated using the velocities calculated from our scaling laws, and t_{cooling} time can be estimated for a given volcano using various analytical or numerical methods, taking into account the width of the conduit, the temperature difference between the magma and the host rock, and the thermal conductivity of the surrounding host rock.

The simplest way to evaluate a value would be to use an analytical expression such as the one presented by Carslaw and Jaeger (1959) Let's represent the conduit as a thermal anomaly using this expression:

$$T(x, t = 0) = \Delta T \exp\left(-\left(\frac{x}{\sigma} \right)^2 \right) + T_{\text{host}}, \tag{2.11}$$

where $T(0)$ is the temperature at the center of the dike, x is the distance from the center of the conduit, t is the time since magma emplacement, ΔT is the temperature difference between the magma at the time of the intrusion and the surrounding host rock, $\sigma = W/2$ is half the thickness of the dyke, and T_{host} is the temperature of the surrounding host rock. We can then estimate the temperature at the center of the conduit for $x = 0$ using the following analytical formula:

$$T(0, t) = \frac{\Delta T}{\sqrt{1 + \frac{4t\kappa}{\sigma^2}}} + T_{\text{host}}, \tag{2.12}$$

where κ is the thermal diffusivity of the host rock. We then substitute in this equation the temperature at which we consider the magma motionless $T\text{cool}$ (typically the temperature that correspond to 50 percent crystallization) and the associated cooling time t_{cool}:

$$T_{\text{cool}} = \frac{\Delta T}{\sqrt{1 + \frac{4t_{\text{cool}}\kappa}{\sigma^2}}} + T_{\text{host}}. \tag{2.13}$$

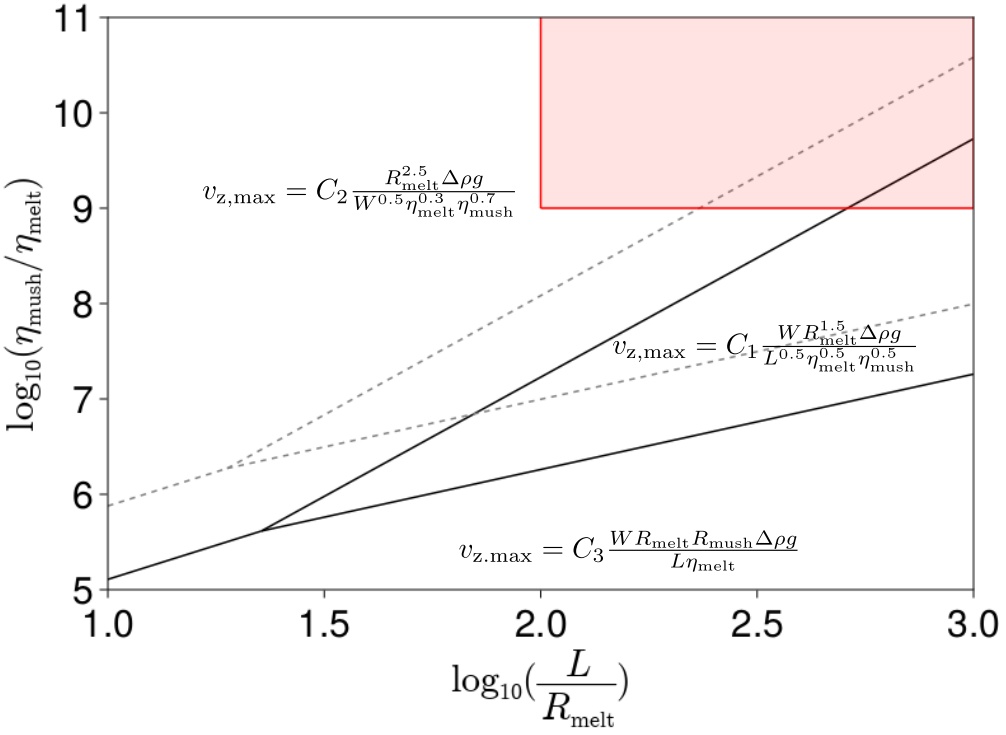

FIGURE 2.5: Map of the melt dynamics in the volcanic conduit across the parameter space. Each scaling law is dominant in the region where it's velocity value is lower than the other two. Both solids and dashed lines are built using the functions described in table 2.3. The missing parameters are defined for the solid line as such: $R_{\mathrm{mush}} = 7R_{\mathrm{melt}}$ and $W = R_{\mathrm{melt}}/10$. For the dashed line: $R_{\mathrm{mush}} = 3R_{\mathrm{melt}}$ and $W = R_{\mathrm{melt}}/13$. The exact value of the parameters are of no importance as long as those ratios are preserved. The red area indicates the subdomain of the parameter space relevant to the case of the Cumbre Vieja (although the viscosity ratio possibilities extend way higher (potentially up to $\log_{10}(\eta_{\mathrm{mush}}/\eta_{\mathrm{melt}}) = 19$)

The typical cooling time can then be estimated by rearranging this equation as follows:

$$t_{\mathrm{cool}} = \frac{\left(\left(\frac{\Delta T}{T_{\mathrm{cool}} - T_{\mathrm{host}}}\right)^2 - 1\right)\sigma^2}{4\kappa}, \tag{2.14}$$

where T_{cool} is the temperature at which the magma has a too large crystal fraction to flow. This can also be simplified by simply using the classical conduction timescale $t_0 = \frac{\sigma^2}{2\kappa}$ in certain cases, but this would mean neglecting the petrological one we often have, which is the crystallisation temperature.

2.4.2 Application: The Cumbre Vieja

Let's apply this method to the Cumbre Vieja volcano on the island of La Palma, Spain. The dynamics of the 2021 eruption have been constrained by many studies, making

it an interesting study case for our method. This eruption started on September 19 and lasted 85 days until December 13. During this time, several vents and a fissure released more than 0.2 km^3 of magma to the surface as tephra and flowing lavas, making this the longest and most voluminous event in the island's history (Civico et al., 2022). Seismic data show two areas of weak seismic swarms concentrated at about the Moho depth (7-14 km) and deeper into the mantle (D'Auria et al., 2022; Fresno et al., 2023). Petrological data from Klügel et al. (2000) and Klügel et al. (2005) also suggest magma differentiation in the mantle and further temporary storage at the Moho. They also hint towards the presence of a crystal-rich mush system comprised of cumulates rock from previous magma batches. D'Auria et al. (2022) identifies as well based on his tomographic survey an area of 400 km^3 characterized by a very large Vp and a very low Vs, potentially a mush body situated under La Palma.

One interesting feature of this eruption is the exceptionally low viscosity of the extruded basanite magma (Castro and Feisel, 2022), causing it to flow rapidly on the slopes of the volcano and towards the sea during the eruption. According to our scaling laws, this low viscosity of the melt should also increase its rising velocity in the volcanic plumbing system and as such have an effect on the efficiency of the magma chamber depletion.

Using petrological as well as geophysical insights, we can partly constrain most of the parameters needed for the application of the scaling laws. We use a model where we assume a 10 km deep melt pocket inside of a bigger mush system and test our scaling laws on it. We constrain the mush size using the estimate of D'Auria et al. (2022) mentioned above, the melt viscosity using the measures from Castro and Feisel (2022) and we vary the remaining parameters to evaluate the uncertainty on the size of the melt pocket and the mush viscosity (see table 2.4 for parameter estimates). We then compute a traveling time $t_t = \frac{v_{z,max}}{L}$ for the melt in the conduit to compare with the critical cooling time due to conduction t_{cool} obtained from the equation 2.14.

TABLE 2.4: Values for La Palma

Parameters	
$\Delta\rho$	300[kg m^{-3}]
η_{melt}	10[Pa s]
L	10[km]
R_{mush}	4.5[km]
W	10[m]
T_{host}	150[°C]
ΔT	1150[°C]
T_{cool}	1100[°C]
κ	10^{-6}[m^2 s^{-1}]

According to our scaling laws, and as shown in the figure 2.6, there is a strong correlation between the viscosity of the magmatic mush and the volume of melt remaining in the pocket at the end of the eruption. For a mush viscosity of $\eta_{mush} = 10^{11}$[Pa s], most of the melt is extracted and the remaining melt pocket contains only about

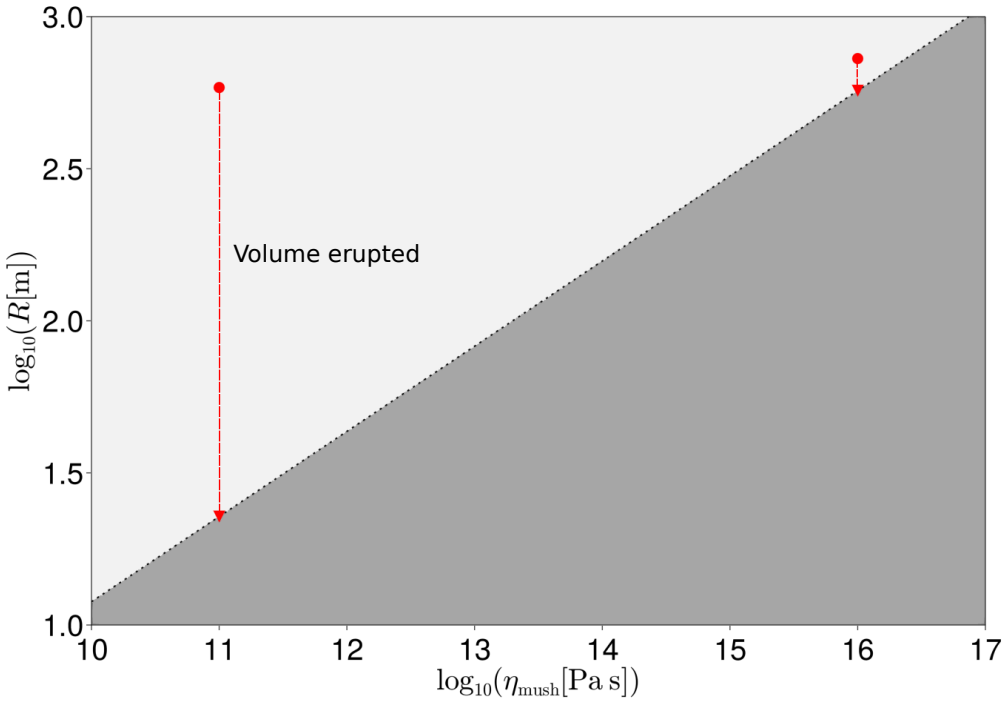

FIGURE 2.6: Comparison of the advection velocity of magma with its cooling by conduction as a function of η_{mush} and R. The other parameters are set according to the table 2.4. The light grey area indicates the regime where advection is dominant and the melt rises in the conduit, while the dark grey area indicates the regime where the melt cools faster than it rises and the eruption stops. The dashed and dotted lines indicate the alternative boundaries between the light and dark grey areas with different widths of the magma conduit. The mapping of the system has been done using all derived scaling laws $v_{\mathrm{z,max}} = \min(v^1_{\mathrm{z,max}}, v^2_{\mathrm{z,max}}, v^3_{\mathrm{z,max}})$ but the whole system is effectively in the plume-driven regime. This matches the location of La Palma on the parameter space as shown in figure 2.5, especially the high $\frac{\eta_{\mathrm{mush}}}{\eta_{\mathrm{melt}}}$. Both red arrows indicate the volume depletion corresponding to the $0.2\mathrm{km}^3$ of magmatic material erupted during the 2021 event compared to the remaining volume of melt present underground at the end of the eruption for two scenarios: $\eta_{\mathrm{mush}} = 10^{11}[\mathrm{Pa\ s}]$ and $\eta_{\mathrm{mush}} = 10^{16}[\mathrm{Pa\ s}]$.

$50000\mathrm{m}^3$. However, for a higher melt viscosity of $\eta_{\mathrm{mush}} = 10^{16}[\mathrm{Pa\ s}]$, the extruded volume of 0.2 km would represent only one-eighth of the total melt previously stored at the base of the crust. This shows a huge variability in the efficiency of the melt depletion from the magmatic pocket. If the mush viscosity increases by only a few more orders of magnitude, so does the volume of magma necessary to sustain the eruption. An eruption occurring in such a system would need a reservoir with a radius of several kilometers to sustain the event through several days or weeks past the evacuation of the gases responsible for the initial overpressure. In the case of La Palma, such a concentration of pure liquid melt would probably have been resolved by the many seismic surveys aimed at the island (D'Auria et al. (2022) estimates a resolution sufficient for anomalies bigger than 4[km]). For such reasons, The large mush area should be of significantly lower viscosity than the surrounding crust ($\eta_{\mathrm{mush}} \leq 10^{17}[\mathrm{Pa\ s}]$).

2.4.3 Interconnected chambers

We also used our numerical model on a setup with several interconnected sills filled with melt (Figure 2.7). First outlooks indicate a strong influence of the viscosity ratio ($\frac{\eta_{\text{mush}}}{\eta_{\text{melt}}}$) on the dominant advection mode in the mush chamber. With $\frac{\eta_{\text{mush}}}{\eta_{\text{melt}}} = 10^9$, the highest velocities of the model are concentrated in the dykes linking the melt pockets. With $\frac{\eta_{\text{mush}}}{\eta_{\text{melt}}} = 10^6$ (after lowering the mush viscosity), the highest velocities are still concentrated in the channels, but the whole system is globally more dynamic. With $\frac{\eta_{\text{mush}}}{\eta_{\text{melt}}} = 10^3$, the melt pockets start to rise in the mush chamber and create a general convection current that prevails over the melt circulation in the dykes. The trend is thus similar to the case of a single melt pocket with a convection-driven regime appearing for a low viscosity ratio similar to figure 2.5.

TABLE 2.5: Connected sills parameters

Parameters	
$\Delta\rho$	500[kg m^{-3}]
η_{melt}	10[Pa s]
L	10[km]
$R_{\text{melt x}}$	12[km]
$R_{\text{melt z}}$	2[km]
$R_{\text{mush x}}$	25[km]
$R_{\text{mush z}}$	18[km]
W	110[m]

An interesting parallel can be drawn here with the conceptual model of Sparks and Cashman (2017), who suggests a direct causal effect of the rapid destabilization of a trans-crustal magmatic mush system on eruptions via the merging of several melt-rich reservoirs.

2.5 Conclusion

Magma ascent from the chamber to the volcanic edifice is strongly controlled by its rheology and the geometry of the magmatic plumbing system. Using a 2D finite element model, we identified the correlations between the rate at which melt rises in a volcanic conduit and several parameters, including the radius of the mush reservoir, the radius of the melt-filled sill, the width of the magmatic conduit, the viscosity of the melt and the viscosity of the magmatic mush. We also characterized these correlations by formulating three different advection regimes in the conduit, each expressed by an analytical scaling law.

Furthermore, we presented an application of the scaling laws to the Cumbre Vieja volcano of La Palma, using data collected around the 2021 eruption. The low magma velocity estimated by Castro and Feisel (2022) and the intense seismic monitoring of the island (D'Auria et al., 2022; Fresno et al., 2023), before and after the eruptions, provided a very interesting case with a wealth of relevant data. Based on our modeling results, we were able to formulate a first-order estimate of the maximum effective

viscosity of the mush under the assumption that buoyancy drove the final phase of the eruption. We hope that these scaling laws can be used as a supplementary tool to interpret observations made at volcanic sites and to improve our understanding of magmatic systems in general.

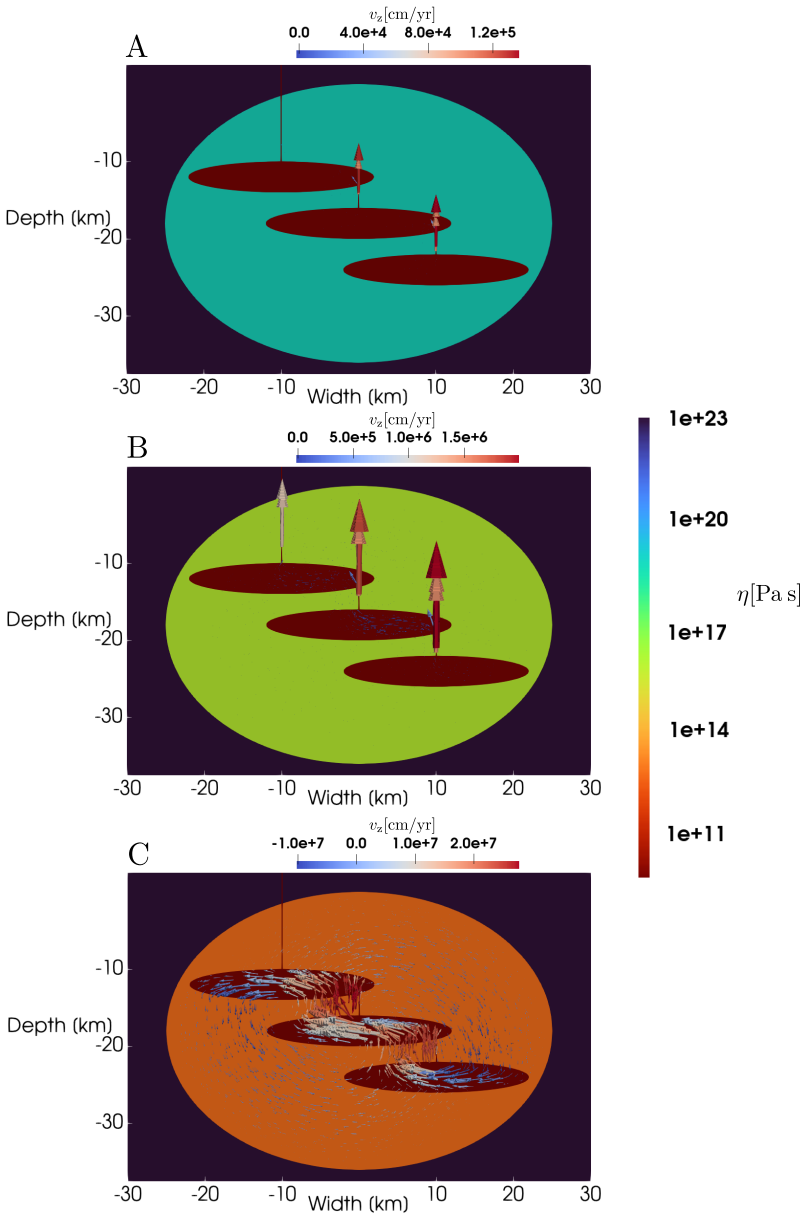

FIGURE 2.7: Visualisation of three models of multiple sills in an upper-crustal magmatic mush following the setup presented in figure 2.1C. The models are presented for three different mush viscosities: 10^{19}[Pa s] in A, 10^{16}[Pa s] in B and 10^{13}[Pa s] in C with the same geometry (described in table 2.5) and a constant melt viscosity of 10^{10}. The sills are connected by dykes filled with melt.

Chapter 3

A numerical method to solve compressible visco-elasto-plastic systems including shear and tensile plasticity

Abstract

A unified theory for magmatic systems, capable of modeling both the ductile transport of magma in the lower crust and the brittle propagation of dykes and shear zones in the upper crust, is fundamental to understanding the mechanisms of melt transport across the lithosphere. One way to achieve this goal is by extending the commonly used numerical continuum approaches in geodynamics to include both mode-1 and mode-2 plastic failure. This work builds towards this goal by presenting a new compressible visco-elasto-viscoplastic formulation adapted to study both ductile and brittle rheologies in a self-consistent manner with a focus on tensile crack initiation and propagation. We introduce a new composite yield function combining Drucker-Prager with a circular approximation to the Griffith criterion coupled with a Perzyna-type regularization viscosity. While mathematically identical, there are several ways to discretize the resulting governing equations numerically. We highlight the differences between the numerical implementations and present local stress update algorithms, and how to combine this into a global stiffness matrix. We implement the governing equations in an implicit finite element framework and use that to demonstrate the numerical efficiency of the numerical formulation. Finally, we present 0D and 2D benchmarks and applications that exemplify tensile fracture in an extensive environment and a dyke propagating through an elasto-plastic host rock. This approach can be implemented as part of a magmatic system model, but can also be used to simulate fluid-induced brittle fracturing in other environments such as in geothermal reservoirs or around salt caverns.

3.1 Introduction

Dykes are the preferred mechanism for transporting magma to the Earth's surface. They are magma-filled tensile fractures that propagate in the crust in a plane generally parallel to σ_3 (Anderson, 1951; Rivalta et al., 2015). This is a mechanical process that predominates in the upper part of the lithosphere, where the rock rheology is mostly elastic and brittle. By connecting a magma chamber to the surface (Acocella and Neri, 2009; Rubin, 1995), but also several magma chambers to each other (Menand, 2011; Sparks and Cashman, 2017), they form a central part of any volcanic plumbing system. Consequently, the study of this process through numerical modeling has been a major focus of the geodynamic community over the years. Currently, the most successful models of dyke propagation use semi-analytical formulations that describe fractures driven by the buoyancy or overpressure of the magma they transport (Maccaferri et al., 2011; Rivalta et al., 2015). These models can accurately predict the direction (Maccaferri et al., 2014; Mantiloni et al., 2023) and propagation of single or multiple dykes and give great insights into the stress field at depth in a volcanic province. Yet, they assume that the host rock deforms in a homogeneous elastic or visco-elastic manner, and thus simplify the more complex nonlinear rheology of rocks. They can also not simulate the broader scale evolving heterogenous nature of the lithosphere or address the visco-elastic behavior of a highly crystallized 'mush' magma chamber as well as the ductile modes of fluid transport occurring at deeper levels in the lithosphere. Within the lithosphere community, it has now become routine to simulate large-deformations of visco-elasto-plastic heterogeneous lithosphere in 2D and 3D (Kaus et al., 2016; Gerya, 2019; Baumann et al., 2018; Pons et al., 2022; Candioti et al., 2022; Andrić-Tomašević et al., 2023; Riel et al., 2023). Yet plastic deformation in these simulations is usually limited to a mode-2 model (such as a Drucker-Prager formulation) that does not include a tensile opening mode and can thus not simulate diking. Moreover, the two-phase nature of magmatic systems consisting of melt and solid rocks is typically not included.

Keller et al. (2013) demonstrated that it is in principle possible to extend a two-phase numerical formulation to include visco-elasto-plastic rheologies, necessary to simulate magma migration through the entire lithosphere. In their approach, the mechanics of tensile plasticity played a central role in dyke nucleation and propagation (partly following Rozhko et al. (2007)). However, the plasticity model of Keller et al. (2013) doesn't seem to always guarantee convergence to a unique solution with physical stress values. Resolving this is important in order to avoid unrealistic negative values of deviatoric stresses and to ensure the convergence of every time step of the model to the solution.

Two additions can remedy this problem: a regularisation scheme capable of imposing a rate dependence on the inherently rate-independent plastic failure process, and a continuous and differentiable yield function that guarantees an effective return mapping for both the shear and tensile modes of plasticity. Duretz et al. (2019) and

Duretz et al. (2020) and Jacquey and Cacace (2020a) have recently introduced the concept of viscoplasticity to regularise models applied to lithospheric scale deformations, building up on approaches that have been used in engineering (Perzyna, 1966; Wang et al., 1997; Heeres et al., 2002). The two main advantages of this type of regularisation are the introduction of a reference time and length scale to the plastic deformation and an improvement in global convergence.

There are also a number of recent studies that employed viscoplasticity in the context of igneous processes. In particular, Kiss et al. (2023) use a Duvaut-Lions viscoplasticity model (Duvaut and Lions, 1972) and a composite yield function that links the Drucker-Prager yield function directly to the Griffith criterion (Murrell, 1964b; Murrell, 1964a; Fullsack, 1995) for tensile failure. However, their numerical implementation is based on the finite-difference pseudo-transient method (Räss et al., 2022), thus avoiding several intricacies relative to the implementation of this rheology in a typical implicit formulation. Li et al. (2023) use the consistent viscoplasticity model (Heeres et al., 2002) and a hyperbolic yield function converging to Drucker-Prager for high deviatoric stresses for both plasticity modes (shear and tensile), but assume a linear rheology outside the plasticity domain.

In the present study, we present the derivation and implementation of a new compressible visco-elasto-viscoplastic framework with a mixed velocity-pressure finite element formulation. We use Perzyna's viscoplasticity model (Perzyna, 1966) for spatial and temporal regularization and allow for nonlinear rheological models such as dislocation creep and nonlinear plastic models. We also propose a circular cap function to link the typical Drucker-Prager yield criterion to the tensile yield strength using a simple continuous and differentiable formulation. The local iterations necessary to update the stresses at the integration points are discussed along with the problem of having two pressure fields resulting from volumetric plasticity. The implementation of the necessary derivatives to solve the presented system of equations using Newton-Raphson iterations for an implicit finite element scheme is presented in detail in the appendix.

3.2 Physical model

3.2.1 Preliminaries

Before laying out the system of equations for this work, we need to introduce a few definitions to the reader. In this work, the trace and deviatoric projection of a tensor as well as the effective magnitude of the tensor (square root of the second invariant)

are respectively defined as:

$$\mathrm{tr}\,(a_{ij}) = a_{kk}, \tag{3.1}$$

$$\mathrm{dev}\,(a_{ij}) = a_{ij} - \frac{1}{3}\,a_{kk}\delta_{ij}, \tag{3.2}$$

$$a_{\mathrm{II}} = \left(\frac{1}{2}a_{ij}a_{ij}\right)^{\frac{1}{2}}, \tag{3.3}$$

where δ_{ij} is the Kronecker delta. We also define the strain rate tensor ($\dot{\epsilon}_{ij}$) as well as the deviatoric ($\dot{\varepsilon}_{ij}$) and volumetric ($\dot{\theta}$) strain rates and the spin tensor ($\dot{\omega}_{ij}$) using velocity v_i as the primary variable:

$$\dot{\epsilon}_{ij} = \frac{1}{2}\left(\frac{\partial v_i}{\partial x_j} + \frac{\partial v_j}{\partial x_i}\right), \tag{3.4}$$

$$\dot{\varepsilon}_{ij} = \mathrm{dev}\,(\dot{\epsilon}_{ij})\,, \tag{3.5}$$

$$\dot{\theta} = \mathrm{tr}\,(\dot{\epsilon}_{ij})\,, \tag{3.6}$$

$$\dot{\omega}_{ij} = \frac{1}{2}\left(\frac{\partial v_i}{\partial x_j} - \frac{\partial v_j}{\partial x_i}\right). \tag{3.7}$$

Finally, we define the Cauchy stress tensor (σ_{ij}), the deviatoric stress (τ_{ij}) and the pressure (p), positive in compression according to the usual practice in geology:

$$\sigma_{ij} = \tau_{ij} - p\,\delta_{ij} \tag{3.8}$$

$$\tau_{ij} = \mathrm{dev}\,(\sigma_{ij}) \tag{3.9}$$

$$p = -\frac{1}{3}\mathrm{tr}\,(\sigma_{ij}) \tag{3.10}$$

3.2.2 Conservation and constitutive equations

We solve a set of two equations to conserve mass and momentum:

$$\frac{\partial \tau_{ij}}{\partial x_j} - \frac{\partial p}{\partial x_i} - \alpha_{\mathrm{b}}\frac{\partial p_{\mathrm{fl}}}{\partial x_i} + \rho g_i = 0, \tag{3.11}$$

$$\dot{\theta} + \frac{1}{K}\frac{Dp}{Dt} - \dot{\lambda}\,\mathrm{tr}\left(\frac{\partial Q}{\partial \sigma_{ij}}\right) = 0. \tag{3.12}$$

The rheological model for shear deformation is based on the Maxwell serial coupling of a diffusion creep, a dislocation creep, an elastic and a viscoplastic element, using a Perzyna viscoplastic model to ensure regularization and convergence of the plastic case. The rheological model for volumetric deformation consists of an elastic element, that represents the pressure-volume equation of state in an incremental form, in a Maxwell coupling with a similar viscoplastic element. The yield function and the plastic potential are identical for shear and volumetric deformations (Figure

3.1). The effect of fluid pressure (p_{fl}) on the system is expressed in the momentum equation and depends on the Biot-Willis constant (see Biot and Blot, 1941; Lade and De Boer, 1997):

$$\alpha_{\mathrm{b}} = 1 - \frac{C_{\mathrm{s}}}{C} \tag{3.13}$$

where C_{s} is the compressibility of solid grains and C is the compressibility of the porous rock.

The deviatoric constitutive equation is:

$$\dot{\varepsilon}_{ij} = \dot{\varepsilon}_{ij}^{\mathrm{vis,dif}} + \dot{\varepsilon}_{ij}^{\mathrm{vis,dis}} + \dot{\varepsilon}_{ij}^{\mathrm{el}} + \dot{\varepsilon}_{ij}^{\mathrm{vp}}, \tag{3.14}$$

where

$$\dot{\varepsilon}_{ij}^{\mathrm{vis,dif}} = A_{\mathrm{D}}\, \tau_{ij}, \tag{3.15}$$

$$\dot{\varepsilon}_{ij}^{\mathrm{vis,dis}} = A_{\mathrm{N}}\, (\tau_{\mathrm{II}})^{n-1}\, \tau_{ij}, \tag{3.16}$$

$$\dot{\varepsilon}_{ij}^{\mathrm{el}} = \frac{\overset{\diamond}{\tau}_{ij}}{2G}, \tag{3.17}$$

$$\dot{\varepsilon}_{ij}^{\mathrm{vp}} = \dot{\lambda}\, \mathrm{dev} \left(\frac{\partial Q}{\partial \sigma_{ij}} \right). \tag{3.18}$$

$$\tag{3.19}$$

The creep pre-factors are:

$$A_{\mathrm{D}} = B_{\mathrm{D}}\, \exp \left[- \frac{E_{\mathrm{L}}}{RT} \right], \tag{3.20}$$

$$A_{\mathrm{N}} = B_{\mathrm{N}}\, \exp \left[- \frac{E_{\mathrm{N}}}{RT} \right]. \tag{3.21}$$

B_{D}, B_{N} and E_{D}, E_{N} are respectively the creep parameters and activation enthalpy of the corresponding mechanism, R is the gas constant and n is the power law exponent. The Jaumann objective stress rates are defined as:

$$\overset{\diamond}{\tau}_{ij} = \frac{\partial \tau_{ij}}{\partial t} + \tau_{ik}\omega_{kj} - \omega_{ik}\tau_{kj} \tag{3.22}$$

and the plastic multiplier following a Perzyna linear viscoplastic model:

$$\dot{\lambda} = \frac{\langle F \rangle}{\eta^{\mathrm{vp}}}. \tag{3.23}$$

where the yield function F is surrounded by Macaulay brackets meaning:

$$\langle F \rangle = \begin{cases} F, & F \geq 0 \\ 0, & \text{otherwise} \end{cases}. \tag{3.24}$$

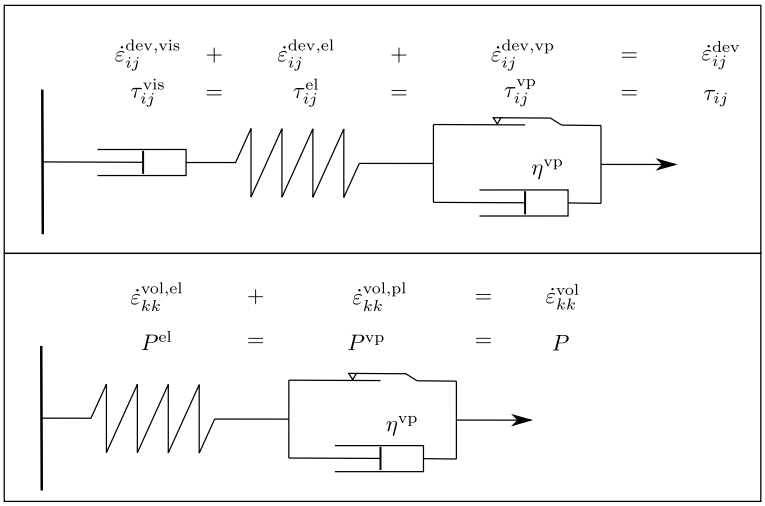

FIGURE 3.1: Schematic representation of the employed deviatoric and bulk rheologies. The deviatoric strain rate is composed of a viscous, elastic and viscoplastic part following a Perzyna scheme.

For the scope of this study, we consider a composite yield function (F), using the pressure-dependent Drucker-Prager function for the shear plastic domain (mode 2) and a circular cap function for the tensile domain (mode 1). We also define a non-associated flow function (Q) as illustrated in figure 3.2(b). The plastic parameters are the friction angle (φ), the dilation angle (ψ), the Mohr-Coulomb cohesion (c_{MC}) and the tensile strength (p_{T}).

The yield function is expressed as

$$F = \begin{cases} \tau_{\mathrm{II}} - k\,p - c, & \tau_{\mathrm{II}}\,(p_{\mathrm{y}} - p_{\mathrm{d}}) \geq \tau_{\mathrm{d}}\,(p_{\mathrm{y}} - p) \\ a\,\left(\hat{R}_{\mathrm{y}} - R_{\mathrm{y}}\right), & \text{otherwise} \end{cases}, \tag{3.25}$$

where

$$\hat{R}_{\mathrm{y}} = \sqrt{\tau_{\mathrm{II}}^2 + (p - p_{\mathrm{y}})^2}, \tag{3.26}$$

and the flow potential is

$$Q = \begin{cases} \tau_{\mathrm{II}} - k_{\mathrm{q}}\,p - \mathrm{const}, & \tau_{\mathrm{II}}\,(p_{\mathrm{q}} - p_{\mathrm{d}}) \geq \tau_{\mathrm{d}}\,(p_{\mathrm{q}} - p) \\ b\,\left(\hat{R}_{\mathrm{q}} - \mathrm{const}\right), & \text{otherwise} \end{cases}, \tag{3.27}$$

where

$$\hat{R}_{\mathrm{q}} = \sqrt{\tau_{\mathrm{II}}^2 + (p - p_{\mathrm{q}})^2}. \tag{3.28}$$

As explained in Jiang and Xie (2011), there are several possible variations of the Drucker-Prager strength criteria. We selected here one that is widely used by the community (Keller et al., 2013; Kaus et al., 2016; Duretz et al., 2021), the formulation of which is simple and doesn't systematically over-estimate the rocks' strength:

$$k = \sin\varphi, \tag{3.29}$$

$$k_{\mathrm{q}} = \sin\psi, \tag{3.30}$$

$$c = c_{\mathrm{MC}} \cos\varphi. \tag{3.31}$$

In order to ensure a smooth transition between the two yield and flow functions over the whole stress domain (see figure 3.3), we define scaling parameters:

$$a = \sqrt{1 + k^2}, \tag{3.32}$$

$$b = \sqrt{1 + k_{\mathrm{q}}^2}. \tag{3.33}$$

Using this, we compute the tensile yield surface center coordinate (P_{y}) and radius (R_{y}), the delimiter point coordinates between both yield functions (p_{d},τ_{d}) and the tensile flow potential center coordinate (p_{q}):

$$p_{\mathrm{y}} = \frac{p_{\mathrm{T}} + \frac{c}{a}}{1 - \frac{k}{a}}, \tag{3.34}$$

$$R_{\mathrm{y}} = p_{\mathrm{y}} - p_{\mathrm{T}}, \tag{3.35}$$

$$p_{\mathrm{d}} = p_{\mathrm{y}} - R_{\mathrm{y}} \frac{k}{a}, \tag{3.36}$$

$$\tau_{\mathrm{d}} = k\, p_{\mathrm{d}} + c, \tag{3.37}$$

$$p_{\mathrm{q}} = p_{\mathrm{d}} + k_{\mathrm{q}} \tau_{\mathrm{d}}. \tag{3.38}$$

The smooth flow potential gradient can be expressed from those variables:

$$\frac{\partial Q}{\partial \sigma_{ij}} = B_\tau \tau_{ij} + B_p \delta_{ij}, \tag{3.39}$$

where:

$$(B_\tau, B_p) = \begin{cases} \left(\frac{1}{2\tau_{\mathrm{II}}}, \frac{k_{\mathrm{q}}}{3}\right), & \tau_{\mathrm{II}}\,(p_{\mathrm{q}} - p_{\mathrm{d}}) \geq \tau_{\mathrm{d}}\,(p_{\mathrm{q}} - p) \\ \left(\frac{b}{2\hat{R}_{\mathrm{q}}}, -\frac{b(p - p_{\mathrm{q}})}{3\hat{R}_{\mathrm{q}}}\right), & \text{otherwise} \end{cases}. \tag{3.40}$$

3.2.3 Perzyna regularization scheme

As explained by Borst and Duretz (2020), strain localization in general, and plastic strain localization in particular, poses a challenge to continuum mechanics modeling. This is because it can concentrate most of a model's deformation in an area of "zero thickness" that can't be resolved by the model's mesh size. This causes the strain and velocity field to be highly dependent on the model resolution as well as severe

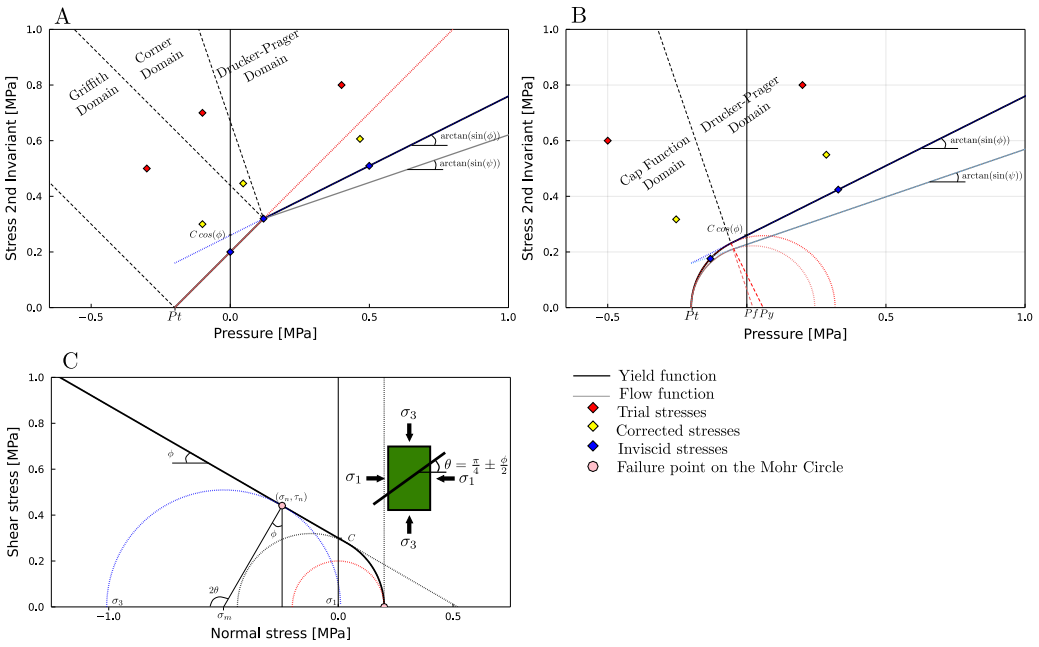

FIGURE 3.2: A: Meridional plot of a composite yield functions similar to the ones used in Keller et al. (2013) or Kiss et al. (2023). The complete function is discontinuous and special care must be applied to ensure the proper mapping of the stress back to the yield at the corner of the yield functions The red diamonds indicate a theoretical visco-elastic stress state outside of the yield limit, the blue ones point to the inviscid stress state (or the stress state after plastic correction if there is no regularization) and the yellow ones to the full visco-elasto-viscoplastic stress state. B: Meridional plot of the composite yield function used in this work. This function is fully continuous and differentiable and guarantees a smooth transition between both domains of the yield function without additional effort. C: Representation of the original Mohr-Coulomb formula from which both of those simplifications are derived, plotted over the normal stress $\sigma_n = \frac{\sigma_1+\sigma_2}{2}$ and the shear stress $\tau_n = \frac{\sigma_1-\sigma_2}{2}$

.

convergence problems (Spiegelman et al., 2016; Duretz et al., 2019). The solution we have adopted to counteract this effect is to add a deformation-limiting viscosity to the plastic strain rate as shown in the figure 3.1, hence the term "viscoplasticity". We use the method of Perzyna (1966) as formulated in the works of Heeres et al. (2002) or Jacquey and Cacace (2020a). Since our yield function F already fulfils the conditions of being continuous and convex in $[0, \infty\rangle$, we are free to define the plastic multiplier as we did in equation 3.24:

$$\dot{\lambda} = \frac{\langle F \rangle}{\eta^{\mathrm{vp}}}. \tag{3.41}$$

There are two important consequences of using this method. First, the addition of a regularization viscosity η^{vp} provides a time scale and implicitly a length scale to the plastic deformation for a large enough value of η^{vp} and a low enough strain (see Duretz et al., 2023; Wang, 2019), simultaneously solving the convergence issues and the mesh dependence of the results. Since this length scale depends on the value

of η^{vp} chosen, it is important to choose a value appropriate for the specific process one wishes to model. The second consequence of using this method is the so-called "overstress" associated with it. Since the addition of η^{vp} is done in the calculation of the plastic multiplier $\dot{\lambda}$ and not directly in the formulation of the yield function F (as in the consistency method used by Duretz et al. (2019) and Duretz et al. (2021)), the model can converge with $F > 0$ and thus stresses converge over the yield function (for example, the yellow diamonds in the figure 3.2), causing what we call overstress. This isn't normally a problem, but in the case of composite yield functions such as the one we have here, it becomes particularly important that the elements of the yield functions, as well as the non-associated flow potential, are continuous for $F \geq 0$ (see figure 3.3). We add scaling parameters to our formulation to ensure this continuity (equations 3.32 and 3.33). The rate-independent plasticity is naturally recovered with this formulation for $\eta^{\text{vp}} = 0$.

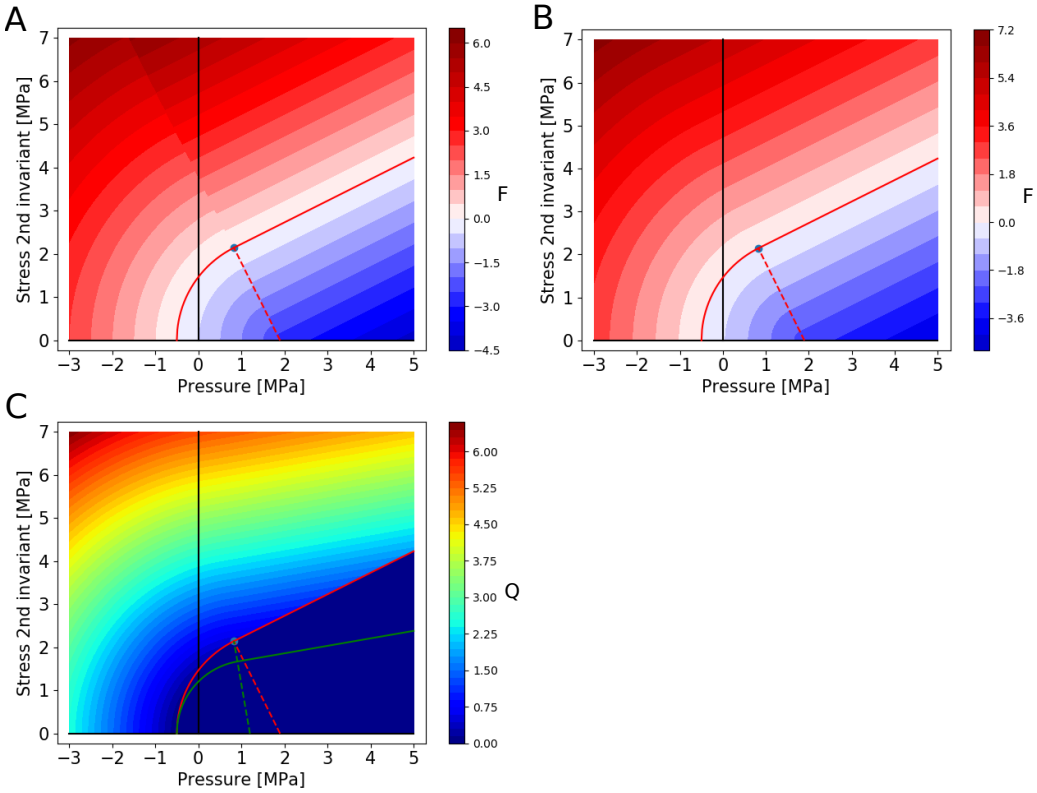

FIGURE 3.3: A: Meridional plot of the composite yield function with the value of the yield function F plotted in contour without the scaling parameter a. Even though the function is continuous for $F = 0$, this is not the case for higher values of the yield function F, as indicated by the discontinuity of the color fields. B: Meridional plot of the composite yield function with the value of F plotted contour with the scaling parameters a. In this case, the function is continuous on the domain $F \geq 0$. C: Meridional plot of the composite yield function with the value of the flow function Q plotted in contour with the scaling parameters b. $Q = 0$ is plotted in green for reference. The gradient of the flow function is continuous above the yield and guarantees a consistent return mapping.

3.3 Numerical formulation

3.3.1 Time and space discretization

The momentum and continuity equations are discretized using the finite element method in 2D and a seven-node triangular Crouzeix-Raviart element. All variables are distributed on the element following the layout presented in figure 3.4. For stability reasons and following the demonstration of Crouzeix and Raviart (1973), the pressure field is discontinuous between elements. The constitutive equations are computed over six integration points. The triangular mesh is generated by the Triangle software (Shewchuk, 1996) using the MeshPy Python API (Kloeckner et al., 2022) to define the geometry of the models.

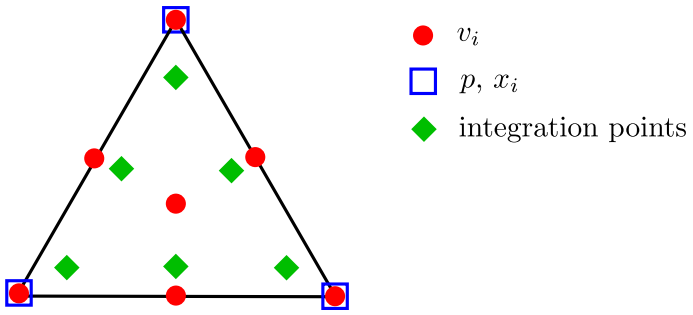

FIGURE 3.4: Seven-nodes triangular Crouzeix-Raviart element. The velocity is defined on all seven nodes while the pressure is defined on each corner (and is not shared with neighbouring elements since it is defined discontinuous). The element is subparametric since the coordinates are defined only on the three corner node. All historical variables are directly saved on the integration points.

The equations are also discretized over time, following a backward Euler implicit scheme:

$$\Delta t = t_{n+1} - t_n \tag{3.42}$$

where the subscript n denotes the beginning of the current time step. All quantities are presented by their unknown values in the end of the time step and assumed to be constant during the time step. The end of the current time step subscript is omitted in the following equations for clarity, i.e. $p = p_{n+1}$.

3.3.2 Primary variables

3.3.2.1 True global pressure scheme

Global primary variables are the velocity (v_i) and pressure (p^*). The star in the superscript explicitly indicates that during the global iterations, the global pressure (that is the value obtained from solving the coupled system of equations) may differ from the pressure obtained by the local stress update (p), i.e. $p^* \neq p$. The difference is caused by the dilatant plasticity that has a nonzero volumetric plastic strain rate

component. The local stress update is formulated as a strain rate-driven problem, hence the local pressure (p) should be discarded and the global residuals should be evaluated using the globally discretized pressure variable (p^*), namely:

$$\frac{\partial \tau_{ij}}{\partial x_j} - \frac{\partial p^*}{\partial x_i} - \alpha_\mathrm{b} \frac{\partial p_\mathrm{fl}}{\partial x_i} + \rho g_i = 0 \tag{3.43}$$

$$\dot{\theta} + \frac{1}{K}\frac{Dp^*}{Dt} - \dot{\lambda}\,\mathrm{tr}\left(\frac{\partial Q}{\partial \sigma_{ij}}\right) = 0 \tag{3.44}$$

Here, it should be noted that the plastic strain rate is evaluated using the updated stress obtained by the local iterations. Upon convergence of the global iterations, both pressure variables become approximately the same, i.e. $p^* \approx p$. For the non-dilatant plasticity case, the initial difference in pressure variables does not occur.

3.3.2.2 Trial global pressure scheme

The global pressure variable (p^*) can be alternatively interpreted as a trial pressure. In this case the local (updated) pressure should be used in the momentum equation, and the volumetric plastic strain rate should be discarded from the continuity equation:

$$\frac{\partial \tau_{ij}}{\partial x_j} - \frac{\partial p}{\partial x_i} - \alpha_\mathrm{b} \frac{\partial p_\mathrm{fl}}{\partial x_i} + \rho g_i = 0 \tag{3.45}$$

$$\dot{\theta} + \frac{1}{K}\frac{Dp^*}{Dt} = 0 \tag{3.46}$$

In this scheme, the difference between the global and local pressure variables need not vanish on convergence, i.e. $p^* \neq p$. We call this approach a trial global pressure scheme since the global pressure converges towards the trial pressure. As before, in the case of non-dilatant plasticity pressure variables are equal.

3.3.3 Stress update: local iterations

3.3.3.1 True global pressure scheme

As several types of non-linearities occur in the constitutive equations (caused by both dislocation creep and plastic corrections), we need to solve a local system of equations on each grid point to retrieve the stress tensor. To this end, we can group the nonlinear stress update equation into a residual vector (for derivations see Appendix 3.A):

$$\mathbf{r} = \begin{bmatrix} \dot{\varepsilon}^*_\mathrm{II} - A_\mathrm{L}\,\tau_\mathrm{II} - A_\mathrm{N}\,(\tau_\mathrm{II})^n - \dot{\lambda}\,A_\tau \\ \dot{\theta}^* + A_\mathrm{K}\,p - \dot{\lambda}\,A_p \\ \langle F \rangle - \dot{\lambda}\,\eta^\mathrm{vp} \end{bmatrix} \tag{3.47}$$

where:

$$\dot{\varepsilon}^*_{ij} = \dot{\varepsilon}_{ij} + \frac{\tau^*_{ij}}{2G\Delta t}, \tag{3.48}$$

$$\dot{\theta}^* = \dot{\theta} - \frac{p_n}{K\Delta t}, \tag{3.49}$$

$$A_{\mathrm{L}} = \frac{1}{2G\Delta t} + A_{\mathrm{D}}, \tag{3.50}$$

$$A_{\mathrm{K}} = \frac{1}{K\Delta t}, \tag{3.51}$$

$$(A_\tau, A_p) = \begin{cases} \left(\frac{1}{2}, k_{\mathrm{q}}\right), & \tau_{\mathrm{II}}\left(p_{\mathrm{q}} - p_{\mathrm{d}}\right) \geq \tau_{\mathrm{d}}\left(p_{\mathrm{q}} - p\right) \\ \left(\frac{b\,\tau_{\mathrm{II}}}{2\hat{R}_{\mathrm{q}}}, -\frac{b(p-p_{\mathrm{q}})}{\hat{R}_{\mathrm{q}}}\right), & \text{otherwise} \end{cases}. \tag{3.52}$$

Here τ^*_{ij} stands for the rotated stress from the previous time step (see the Appendix for more details). Note that stress rotation terms are usually computed using the alternative incrementally-objective scheme (Thielmann et al., 2015; Gerya, 2019). We mention again that the local stress update iteration is formulated as a strain-driven problem, which means that the local pressure (p) is a passive variable and may in general differ from the globally discretized pressure (p^*) (see section 3.3.2.1).

We are solving the stress update set of equations for the second invariant of the deviatoric stress (τ_{II}), the local pressure (p) and the plastic multiplier ($\dot{\lambda}$) which can be merged into a vector $\mathbf{x}$:

$$\mathbf{x} = \begin{bmatrix} \tau_{\mathrm{II}} \\ p \\ \dot{\lambda} \end{bmatrix} \tag{3.53}$$

using Newton-Raphson iterations:

$$\|\mathbf{r}_k\| < \mathrm{tol} \tag{3.54}$$

$$\mathbf{x}_{k+1} = \mathbf{x}_k - \mathbf{J}_k^{-1}\mathbf{r}_k \tag{3.55}$$

with k being the iteration index and $\mathbf{J}$ being the local Jacobian matrix. This matrix can be derived to be:

$$\mathbf{J} = \begin{bmatrix} -A_{\mathrm{L}} - n\,A_{\mathrm{N}}\left(\tau_{\mathrm{II}}\right)^{n-1} - \dot{\lambda}\,\frac{\partial A_\tau}{\partial \tau_{\mathrm{II}}} & -\dot{\lambda}\,\frac{\partial A_\tau}{\partial p} & -A_\tau \\ -\dot{\lambda}\,\frac{\partial A_p}{\partial \tau_{\mathrm{II}}} & A_{\mathrm{K}} - \dot{\lambda}\,\frac{\partial A_p}{\partial p} & -A_p \\ \frac{\partial F}{\partial \tau_{\mathrm{II}}} & \frac{\partial F}{\partial p} & -\eta^{\mathrm{vp}} \end{bmatrix} \tag{3.56}$$

where the derivatives are:

$$\left(\frac{\partial A_\tau}{\partial \tau_{\mathrm{II}}}, \frac{\partial A_\tau}{\partial p}\right) = \begin{cases} (0,0)\,, & \tau_{\mathrm{II}}\left(p_{\mathrm{q}} - p_{\mathrm{d}}\right) \geq \tau_{\mathrm{d}}\left(p_{\mathrm{q}} - p\right) \\ \left(\frac{b\left(\hat{R}_{\mathrm{q}}^2 - \tau_{\mathrm{II}}^2\right)}{2\hat{R}_{\mathrm{q}}^3}, -\frac{b\tau_{\mathrm{II}}(p-p_{\mathrm{q}})}{2\hat{R}_{\mathrm{q}}^3}\right), & \text{otherwise} \end{cases} \tag{3.57}$$

$$\left(\frac{\partial A_p}{\partial \tau_{\mathrm{II}}}, \frac{\partial A_p}{\partial p}\right) = \begin{cases} (0,0)\,, & \tau_{\mathrm{II}}\left(p_{\mathrm{q}} - p_{\mathrm{d}}\right) \geq \tau_{\mathrm{d}}\left(p_{\mathrm{q}} - p\right) \\ \left(\frac{b\tau_{\mathrm{II}}(p-p_{\mathrm{q}})}{\hat{R}_{\mathrm{q}}^3}, -\frac{b\left(\hat{R}_{\mathrm{q}}^2 - (p-p_{\mathrm{q}})^2\right)}{\hat{R}_{\mathrm{q}}^3}\right), & \text{otherwise} \end{cases} \tag{3.58}$$

$$\left(\frac{\partial F}{\partial \tau_{\mathrm{II}}}, \frac{\partial F}{\partial p}\right) = \begin{cases} (1,-k)\,, & \tau_{\mathrm{II}}\left(p_{\mathrm{y}} - p_{\mathrm{d}}\right) \geq \tau_{\mathrm{d}}\left(p_{\mathrm{y}} - p\right) \\ \left(\frac{a\tau_{\mathrm{II}}}{\hat{R}_{\mathrm{y}}}, \frac{a(p-p_{\mathrm{y}})}{\hat{R}_{\mathrm{y}}}\right), & \text{otherwise} \end{cases} \tag{3.59}$$

Although this system of equation has been developed with a rate-dependent viscoplasticity in mind, no change is needed for the rate-independent case since this one is naturally recovered when $\eta^{\mathrm{vp}} \to 0$. The $\dot{\lambda}$ variable becomes then a Lagrange multiplier necessary to enforce the yield surface constraint.

Before we start the general visco-elasto-plastic iteration, a nonlinear visco-elastic trial deviatoric stress (τ_{II}^*) must be computed. This is achieved by isolating the first equation in the system (3.47) and assuming zero plastic multiplier $\dot{\lambda} = 0$:

$$\dot{\varepsilon}_{\mathrm{II}}^* - A_{\mathrm{L}}\,\tau_{\mathrm{II}}^* - A_{\mathrm{N}}\,(\tau^*)^n = 0. \tag{3.60}$$

For the successful convergence of the Newton iterations it is necessary to select a good initial guess. We found the following approximation to perform robustly:

$$(\tau_{\mathrm{II}}^*)_0 = \left(\frac{1}{\tau_{\mathrm{L}}} + \frac{1}{\tau_{\mathrm{N}}}\right)^{-1} \tag{3.61}$$

where:

$$\tau_{\mathrm{L}} = \frac{\dot{\varepsilon}_{\mathrm{II}}^*}{A_{\mathrm{L}}}, \quad \tau_{\mathrm{N}} = \left(\frac{\dot{\varepsilon}_{\mathrm{II}}^*}{A_{\mathrm{N}}}\right)^{1/n}. \tag{3.62}$$

In other words, we start the local iterations with a quasi-harmonic average of the deviatoric stresses resulting from the isolated linear and nonlinear creep mechanisms.

Subsequently, the yield function is evaluated using the trial stresses, and if found to be violated i.e. $F\left(\tau_{\mathrm{II}}^*, p^*\right) > 0$, the general visco-elasto-plastic iterations are invoked. Here we use the newly obtained trial deviatoric stress and the global pressure as initial

guess:

$$\mathbf{x}_0 = \begin{bmatrix} \tau_{\mathrm{II}}^* \\ p^* \\ 0 \end{bmatrix} \tag{3.63}$$

We also rely on a back-tracking line-search algorithm using the Armijo's condition (Armijo, 1966) on the normed residual $\|\mathbf{r}_k\|$ to control the correction rate at every iteration and ensure convergence (figure 3.5). Until:

$$\|\mathbf{r}(\mathbf{x}_{k+1})\| \leq \gamma \|\mathbf{r}(\mathbf{x}_k)\|, \tag{3.64}$$

where $\gamma \leq 1$ is a constant factor, repeat:

$$\mathbf{x}_{k+1} = \mathbf{x}_k + \alpha\, \delta\mathbf{x}_k \tag{3.65}$$

$$\delta\mathbf{x}_k = -\mathbf{J}_k^{-1}\mathbf{r}(\mathbf{x}_k) \tag{3.66}$$

with $\alpha = 1$, the full step length on the first try and $\alpha = \frac{\alpha}{2}$ for each subsequent try.

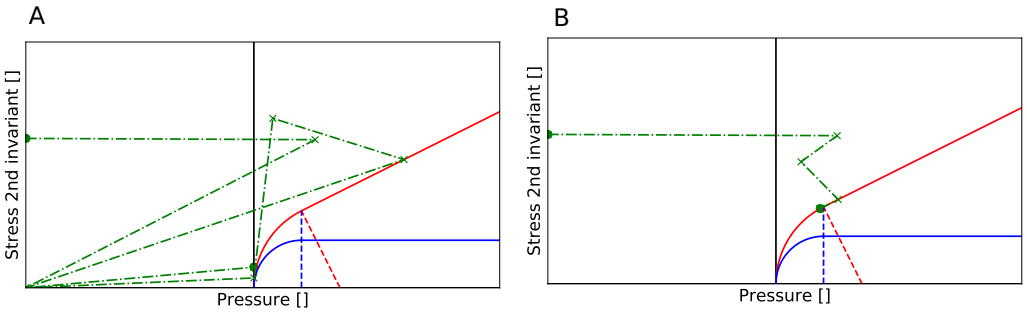

FIGURE 3.5: Illustration of the importance of using line-search. A: updated stress state of a point in 0D that is initially above the yield surface (green) during the first seven local iterations without any limitation on the stress correction. Both pressure and τ_{II} keep evolving without converging to the solution (even when using >5000 iterations). B: updated stress state of a point in 0D with a limiter to the stress correction ensuring the validity of the inequality 3.64. The stress state converges here after seven iterations.

After convergence of the local iteration, the deviatoric stress tensor is computed as:

$$\tau_{ij} = \tau_{\mathrm{II}} \frac{\dot{\varepsilon}_{ij}^*}{\dot{\varepsilon}_{\mathrm{II}}^*} \tag{3.67}$$

Since the result of the local iterations is purely strain rate dependent, $\left(\frac{\partial \dot{\varepsilon}_{\mathrm{II}}^{\mathrm{vp}}}{\partial p^*}\right) = 0$ despite p being a parameter for the yield and flow functions F and Q. This is because p is ultimately a function of $\dot{\theta}$ and, by extension, a function of v_i.

3.3.3.2 Trial global pressure scheme

The difference at the local level is confined to the following modification of the discretized continuity equation:

$$\mathbf{r} = \begin{bmatrix} \dot{\varepsilon}^{*}_{\mathrm{II}} - A_{\mathrm{L}}\,\tau_{\mathrm{II}} - A_{\mathrm{N}}\,(\tau_{\mathrm{II}})^{n} - \dot{\lambda}\,A_{\tau} \\ A_{\mathrm{K}}\,p - A_{\mathrm{K}}\,p^{*} - \dot{\lambda}\,A_{p} \\ \langle F \rangle - \dot{\lambda}\,\eta^{\mathrm{vp}} \end{bmatrix}. \tag{3.68}$$

The first and the third equations in the system remain unmodified. The volumetric strain rate is replaced with an estimate computed from the discretized global (trial) pressure. The remaining part of the local stress update procedure remains the same as in true pressure scheme (for derivations see the appendix).

3.3.4 Strain softening

To simulate the loss of cohesion of a fractured rock compared to an intact rock, some softening can be introduced as a function of accumulated plastic strain:

$$\bar{\varepsilon}^{\mathrm{pl}}_{\mathrm{II}} = \int_{t} \dot{\varepsilon}^{\mathrm{pl}}_{\mathrm{II}}\,dt, \tag{3.69}$$

$$c_{\mathrm{MC}} = c_{\mathrm{MC}}(\bar{\varepsilon}^{\mathrm{pl}}_{\mathrm{II}}) = c_{\mathrm{MC0}} + S_{c}\,\bar{\varepsilon}^{\mathrm{pl}}_{\mathrm{II}}, \tag{3.70}$$

$$\varphi = \varphi(\bar{\varepsilon}^{\mathrm{pl}}_{\mathrm{II}}) = \varphi_{0} + S_{\varphi}\,\bar{\varepsilon}^{\mathrm{pl}}_{\mathrm{II}}, \tag{3.71}$$

where S_c and S_φ are negative softening moduli. This also facilitates strain localization on shear zones and the observation of distinct fault orientations in crustal-scale models. A minimal cohesion value (c^{min}_{MC}) should be set at the minimal value desired.

3.4 Benchmarking and applications

3.4.1 0D analytical tests of the local iterations

We first test the local iteration routine for the stress update on 0D setups. The effect of a constant strain rate applied to a visco-elasto-plastic system present an interesting case study.

For a purely volumetric extensional deformation, the pressure initially decreases with time before reaching the yield, upon which both p and τ_{II} remain constant (figure 3.6 A). This is the expected result since, being shaped as a circular cap, the flow potential function must be perpendicular to the pressure axis for $\tau_{\mathrm{II}} = 0$. This also ensures that the stress will not converge towards negative values because of the plastic correction even for a low τ_{II}. Under a deviatoric shear deformation (figure 3.6 B), τ_{II} progressively increases until reaching the yield (in this case on the circular cap). Because of the plastic dilation, the pressure then starts building up from the plastic

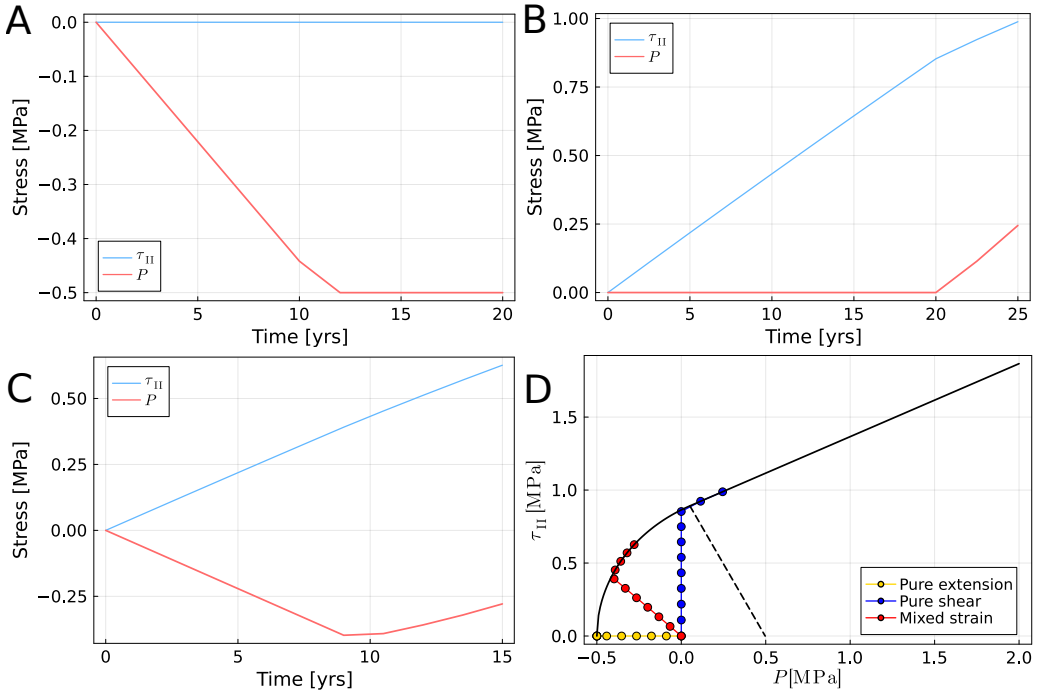

FIGURE 3.6: a. Stress evolution of a point under A: volumetric extension, B: deviatoric shear and C: mixed strain. The subplots A, B, and C present the evolution of the pressure and deviatoric stress second invariant through time, the subplot D presents those same stresses on the meridional plot of the yield function. The black line perpendicular to the yield function on plot D indicates the transition from the cap function to Drucker-Prager. The parameters used in this benchmark are described in the table 3.1

deformation and both p and τ_{II} follow the yield curve, transitioning from the cap function to Drucker-Prager without discontinuity. In the mixed case with both modes of deformation (figure 3.6 C), p decreases similarly to the first case and τ_{II} increases similarly to the second case until reaching the yield. At that point and for those parameters, the increase of pressure provoked by the plasticity in conjunction with the shear deformation overwhelms the elastic volumetric component of the deformation resulting in a pressure increase with time. In general, the pressure will increase or decrease after yield as a function of the deformation, the derivative of the flow function ($\frac{\partial Q}{\partial \sigma_{ij}}$) and the ratio between the visco-elastic effective viscosity and the elastic bulk modulus multiplied by the time-step ($\frac{\eta^{ve}}{K\,\Delta t}$) (Kiss et al., 2023).

3.4.2 Elasto-plastic 2D plate extension

The model includes an elasto-plastic plate with a free surface that undergoes extension and compression. In order to create some heterogeneities and promote the nucleation of faults, an initial accumulated plastic strain field ($\bar{\varepsilon}^{pl}_{II}$) is assigned to the model, following a Gaussian distribution near the surface and, for the compressible case, some randomly distributed weak zones. This then affects the cohesion of the rock as described by the equation 3.70. In both cases, faults first appear at the surface (see figure 3.7) where the pressure is lowest, and develop towards the deeper parts of

TABLE 3.1: Material parameters and background strain rates employed in the different benchmark cases

Variable	Meaning	Figure 3.6A/B/C	Figure 3.8 & 3.7A/B	Figure 3.9 & 3.11	Dimension
$l \times h$	Domain dimensions	-	40×7	40×7	[km] × [km]
S_{el}	Size element	-	50	50	[m]
A_{D}	Diffusion creep pre-factor	5×10^{-21}	-	-	[$\text{Pa}^{-1}\ \text{s}^{-1}$]
G	Shear modulus	10^{10}	4×10^{10}	4×10^{10}	[Pa]
K	Bulk modulus	2×10^{11}	6.4×10^{10}	6.4×10^{10}	[Pa]
c_{MC}	Mohr-Coulomb cohesion	10^{6}	2×10^{7}	2×10^{7}	[Pa]
$c_{\text{MC}}^{\text{min}}$	Minimal Mohr-Coulomb cohesion	-	5×10^{6}	5×10^{6}	[Pa]
S_c	Cohesion softening modulus	-	-10^{8}	-10^{8}	[Pa]
P_{t}	Tensile strength	-5×10^{5}	-10^{6}	-10^{6}	[Pa]
φ	Friction angle	30	30	30	[°]
ψ	Dilation angle	10	0	0	[°]
$\dot{\varepsilon}_{\text{II}}$	Deviatoric strain rate 2nd invariant	$0/7 \times 10^{-14}/7 \times 10^{-14}$	-	-	[s^{-1}]
$\dot{\theta}$	Volumetric strain rate	$7 \times 10^{-15}/0/7 \times 10^{-15}$	-	-	[s^{-1}]
$\dot{\epsilon}_{\text{bg}}$	Background horizontal strain rate	-	$-1.584 \times 10^{-14}/1.584 \times 10^{-14}$	-7.922×10^{-15}	[s^{-1}]
Δt	Time step	2	50/100	1	[yrs]
r_{tol}	Relative tolerance number	-	10^{-5}	10^{-5}	[]

the model at an angle to the horizontal, satisfying on a first order the basic model of Arthur et al. (1978):

$$\alpha = \frac{\pi}{4} \pm \frac{\varphi + \psi}{4}, \tag{3.72}$$

where $\pm$ is an addition for extension and a subtraction for compression (deviations are to be expected from the merging of faults, especially in the compressive setting where several faults nucleate away from the surface at randomly distributed points of lower cohesion). In the extensional setting, faults can propagate to the bottom of the model (7 [km]) and we observe a progressive localization of the strain rate into fewer and fewer fault zones. This localization is much slower in the compressive setting, where similar strain rate magnitudes are reached after three times the time required in the extensional setting. The inverse faults of the compressive setup also don't propagate as deeply into the model, because the pressure at depth is much higher than in the extensive case. Under these conditions, the yield at depth is simply not reached.

An interesting feature of these models, which differs from those produced by codes assuming incompressible plasticity (Popov and Sobolev, 2008; Kaus, 2010) but also from codes using a compressible Drucker-Prager yield and flow function (Duretz et al., 2021; Jacquey and Cacace, 2020b) without a specific Griffith yield criterion, are the vertical cracks that form at the free surface. These form in the extensive case at the very beginning of the localization of plasticity (figure 3.7A) and continue to accumulate volumetric strain until most of the deformation becomes localized in a very small number of normal faults due to the strain softening process. To further explore this, we perform an additional simulation in which we use a dilation angle which suppresses volumetric plastic deformation for shear plasticity (figure 3.8). As a consequence, any plastic correction from the Drucker-Prager part of the yield function can only produce deviatoric plastic strain and all volumetric plastic strain must result from the activation of the tensile cap part of the yield and flow functions. By comparing the accumulated deviatoric and volumetric plastic strains on a plot, we can then observe the transition between the tensile faults produced by the tensile cap at the top of the model and the normal shear faults produced by Drucker-Prager beneath.

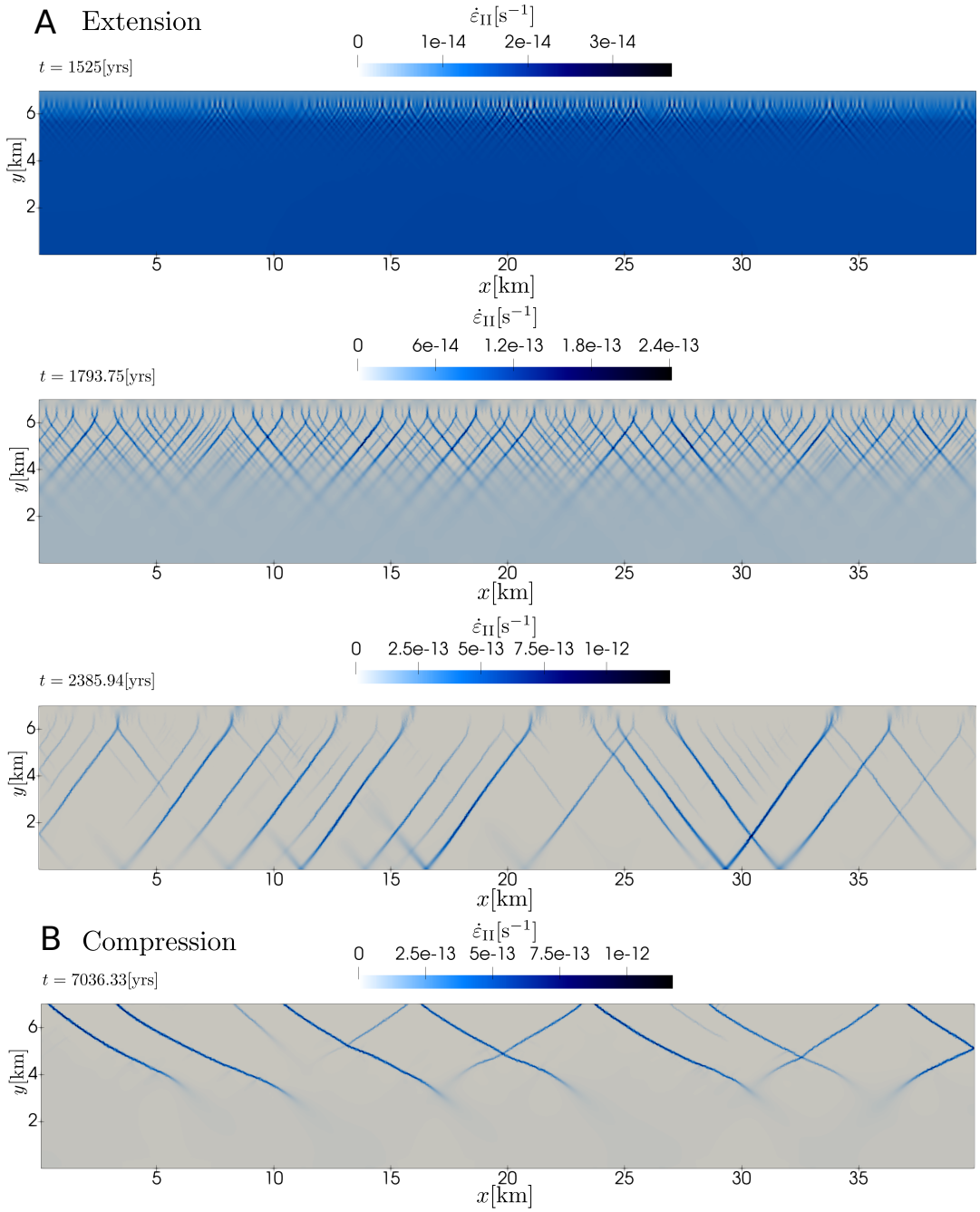

FIGURE 3.7: Elasto-plastic plate under extension (A) and compression (B). A: Temporal evolution of the deviatoric strain rate, showing tensile cracks, normal faults and shear localization. B: Deviatoric strain rate of the same setup under compression.

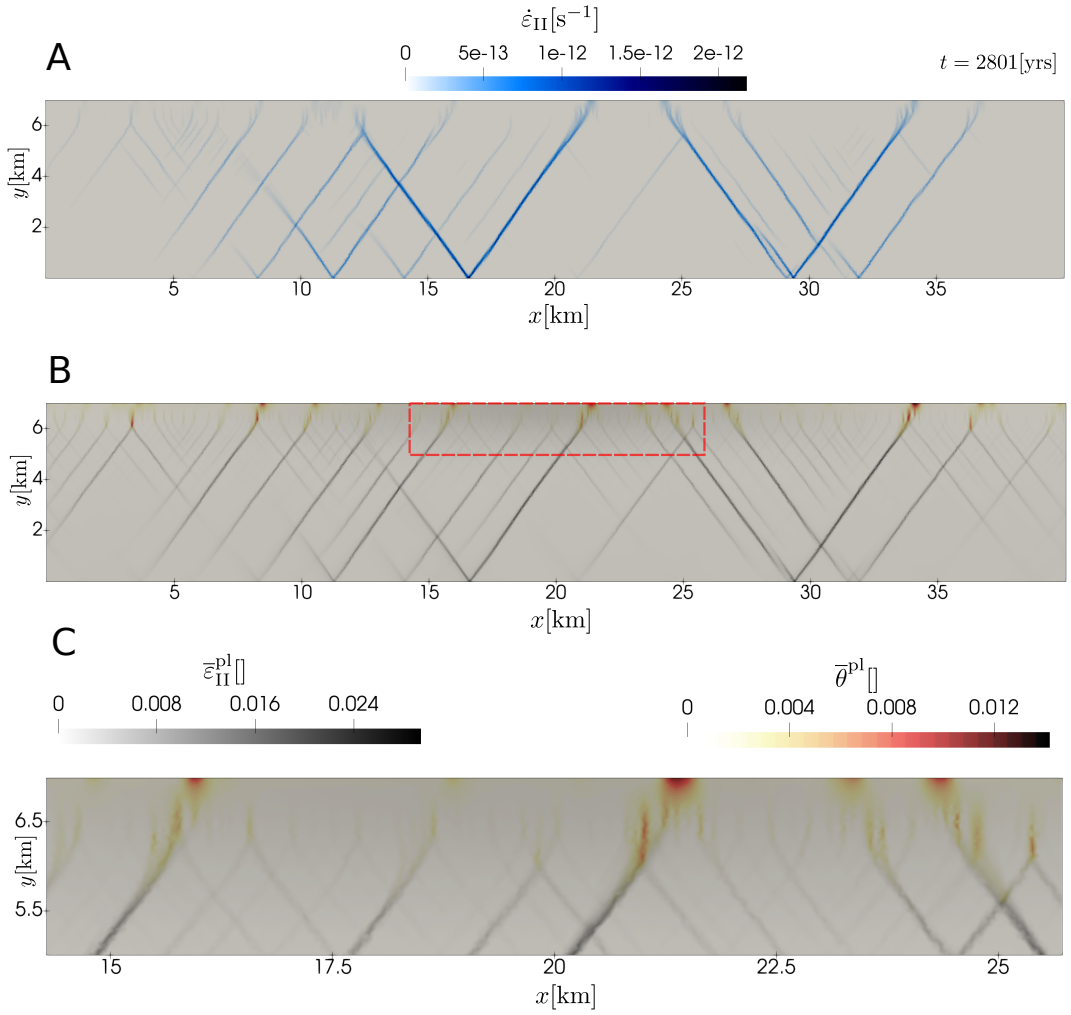

FIGURE 3.8: A: Deviatoric strain rate of an elasto-plastic plate under extension at a late stage, when most of the deformation is concentrated in a few faults. B: Accumulated deviatoric (in grey) and volumetric (in orange) plastic strain for the same simulation. The red dashed square indicates the zoomed area in C. C: Zoom on the transition between tensile cracks and normal shear faults.

3.4.3 2D dyke propagation

Tensile fractures are to a large extent driven by fluid pressure. For reasons of simplicity, we here focus on the plasticity formulation itself leaving out poro-elastic effects. In general, however, a newly opened dike will result in a significantly increased effective permeability compared to a porous background rock. As a result, fluid is expected to rapidly propagate through the dyke and fluid pressures can be expected to be more or less constant within the dike. This effect can be mimicked by starting a simulation with a constant fluid pressure source at the base of the domain, which is explicitly migrated through neighboring elements as a function of their average accumulated volumetric plastic strain ($\overline{\theta}^{\mathrm{pl}}$), similar to weakening of plastic parameters as a function of deviatoric plastic strain (equation 3.69).

A constant fluid pressure (p_{fl}) is set at the bottom of an elasto-plastic crust and

maintained as a fluid pressure source throughout the simulation, while a slight extensional strain is applied to the setting. This causes a significant drop in effective pressure ($p = p_{\text{total}} - p_{\text{fl}}$) into the tensile regime and the appearance of a fractured zone (figures 3.9A, 3.9B). As the fracture progresses upwards, the fluid pressure migrates accordingly and the dyke makes its way to the surface. During this phase, the host rock ruptures on both sides of the dyke, with the maximum velocity occurring at the top of the dyke (see figure 3.9C). While the velocities at the boundary follow the imposed background strain rate (see table 3.1), they reach values that are orders of magnitude higher near the tip of the dyke, suggesting that the dynamics of the system are mainly driven by the brittle failure and the associated elastic rebound.

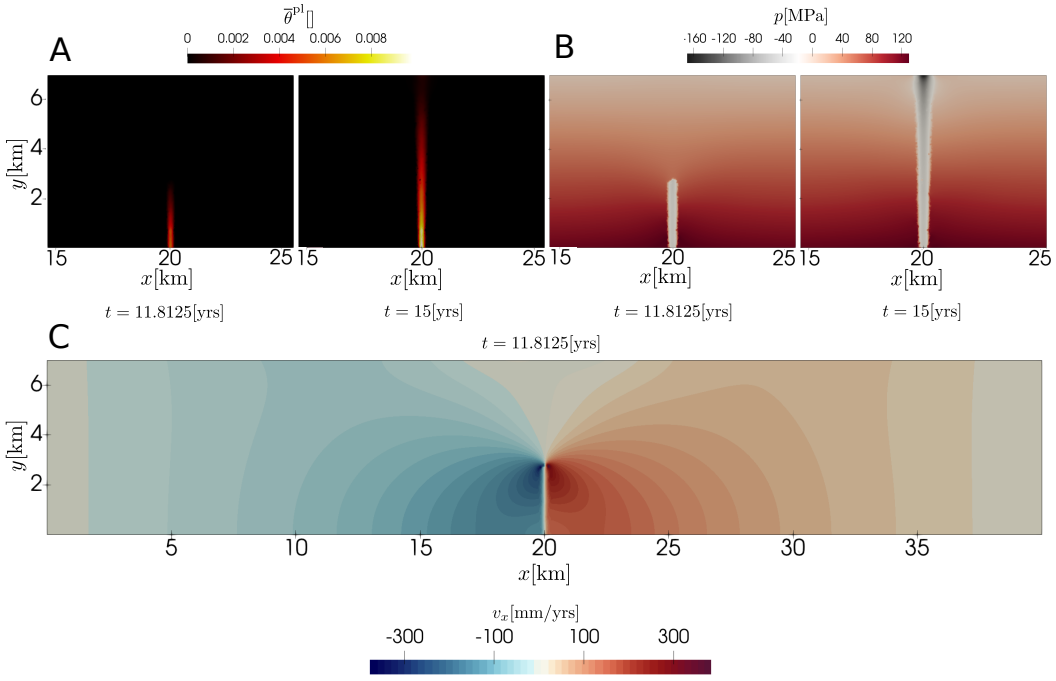

FIGURE 3.9: 2D tensile crack propagating through an elasto-plastic crust in an extensional environment. A: Accumulated volumetric plastic strain after 11.8125 years and 15 years. The drop in effective pressure ($p = p_{\text{total}} - p_{\text{fl}}$) causes tensile failure and the crack forms. B: Effective pressure after 11.8125 years and 15 years. The fluid pressure diffuses into the fractured rock, causing the crack to propagate upwards. C: Horizontal velocity after 11.8125 years. Due to the extension and dike propagation, the model domain is split in the middle, with each side forming a bloc moving in a different direction. Although a small extensional strain is assigned at the side boundaries, most of the displacement occurs close to the top of the dyke, reaching velocities well above the background strain rate.

In this test, dyke propagation accelerates as the depth decreases. This correlates with a continuous decrease in the effective pressure inside the dyke towards the surface. The fluid pressure changes little with depth due to diffusion, and the range of deviatoric stresses around the dyke remains approximately constant. However, the lithostatic pressure decreases rapidly, so that the extreme effective pressures shown in figures 3.9B and 3.11B are well beyond the tensile strength of the rock. As a result, the velocities around the dyke tip increase, as does the rate of dyke propagation, and

the dyke progresses more in the last 3.75 years of the simulation than in the first 11.25 years.

The low pressures found in the dyke are allowed by using rate-dependent viscoplasticity rather than a rate-independent scheme. The Perzyna viscosity also controls the velocities within the dyke, allowing the model domain to be split in two by the dyke without causing a breakdown of convergence of the global solver.

3.4.4 Convergence of the 2D simulations

The convergence of our model is evaluated by comparing the normalized momentum residual with a threshold parameter defined in the table 3.1 (r_{tol}). All 2D simulations presented in this paper were performed with an element size of 50 [m] over a domain of 40[km] $\times$ 7[km] and each time step ended up converging within 10 iterations following a quadratic function as shown in figure 3.10. However, a decrease of the time step is sometimes necessary to ensure this convergence pattern when sharp rheological contrasts appear in the simulation, typically due to plastic strain localization. Consequently, we bisect the time step and restart the overall iterations until we reach a converging pattern again.

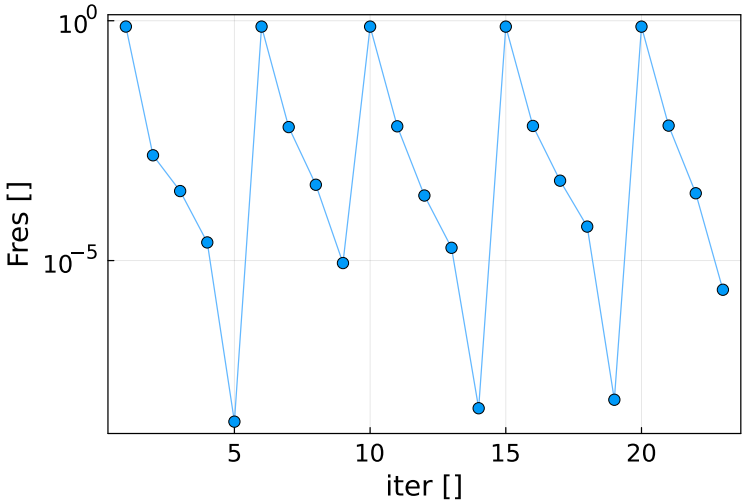

FIGURE 3.10: Global non-linear convergence for the 2D results presented above over five time steps.

3.5 Discussion

3.5.1 The special case of the Pressure variable

As introduced in section 3.3.2, a consequence of dilatant plasticity is the appearance of a local corrected pressure p that may differ from the global pressure p^*. A decision must therefore be made between two schemes for the global pressure: we can either converge it to the true pressure computed during the local iterations ($p^* \approx p$) or converge it to a value corresponding to a test pressure corresponding to the pressure

field of the system if the plastic yield were removed ($p^* \neq p$). The two methods differ slightly, as shown throughout the 3.3 section.

If we converge the global pressure to the true pressure, we can't use the global pressure in the local iterations. As a result, these will be entirely strain driven and all plastic deformation will be calculated from the velocity field. If we converge the global pressure to a trial pressure, on the other hand, the global pressure becomes a variable of the local pressure ($\frac{\partial p}{\partial p^*} \neq 0$) and the local iterations are a function of both v_i and p^*. These differences also have consequences for the global Jacobian matrix, as shown in the appendix. In general, we have observed a better convergence using the trial global pressure scheme and, accordingly, all 2D models presented in this chapter have used this implementation.

3.5.2 The choice of a composite yield function with a circular cap

The choice to link the Drucker-Prager yield and flow functions to the tensile strength of the rock with circular cap functions presents several advantages. Conserving the general Drucker-Prager formulation for higher pressures authorizes the simplification of the parameters to a von Mises yield function (with $\varphi = 0$) or an incompressible type of plasticity (for $\psi = 0$) without implementing exceptions. In addition, other criteria can be used to form the equations 3.29, 3.30 and 3.31 to capture for instance either the outer-bound cone or the inner cone of the Mohr-Coulomb failure criterion (Jiang and Xie, 2011). Finally, as indicated in figure 3.3, we can assure the connection between both function to be continuous and differentiable on the domain $F \geq 0$.

3.5.3 An incremental alternative to the Velocity-Pressure formulation

In the applications presented in sections 3.4.2 and 3.4.3, the global iterations were solved using an incremental scheme (displacement increment - pressure increment) instead of the velocity-pressure formulation presented in this chapter (although the local iterations were still performed exactly as described above). This resulted in much better convergence rates than the original implementation we had tested. The conversion of the strain rate values to strain is simply:

$$\Delta\varepsilon_{ij} = \dot{\varepsilon}_{ij}\ \Delta t \tag{3.73}$$

but this adds a new control over the order of magnitudes of the numbers the solver has to use and guarantees a solution for $\Delta t \to 0$. In practice this allows us to restart a time step where the global iterations fail to converge with a lower Δt until the system starts converging again. This proved to be crucial in modelling dyke propagation, as the velocities varied by orders of magnitude near the tip.

The use of velocity as a primary variable is a logical choice for works studying mainly viscous systems, such as global tectonic or mantle flow models, since the deviatoric stress is correlated with the strain rate (equations 3.15 and 3.16). However,

the upper crust is elasto-plastic and the deviatoric stress is directly correlated with the strain (equations 3.17 and 3.22). Displacement increments are thus often used to model other elasto-plastic materials such as concrete (Caggiano et al., 2012), clay (Perić, 2006) or soil (Lade and Duncan, 1975). It has also been used for the upper crust by Duretz et al. (2019) and Borst and Duretz (2020) in their work on viscoplastic regularization.

3.6 Conclusions

We have derived, implemented and tested a new rheology with the notable addition of a new yield function that allows for a self-consistent tensile fracture initiation and propagation. The proposed implementation couples linear and non-linear viscosity with volumetric and deviatoric elasticity and plasticity. We also include a viscoplastic regularization for the plasticity, a strain softening parameterization and a backtracking line search algorithm for the global iterations. All derivations are presented as thoroughly as possible to make it easy for the reader to implement any part of this method in their own geodynamic code. We have shown that the addition of tensile plasticity can affect the pattern of normal faults in an extensive setup, forming vertical cracks at the surface where lithostatic pressure is lowest. We have also demonstrated the ability of our implementation to produce vertical dikes with the addition of fluid pressure. This opens the door to a range of exciting applications in the study of the ductile-brittle transition in transcrustal magmatic systems, or within the context of induced seismicity in a geothermal context.

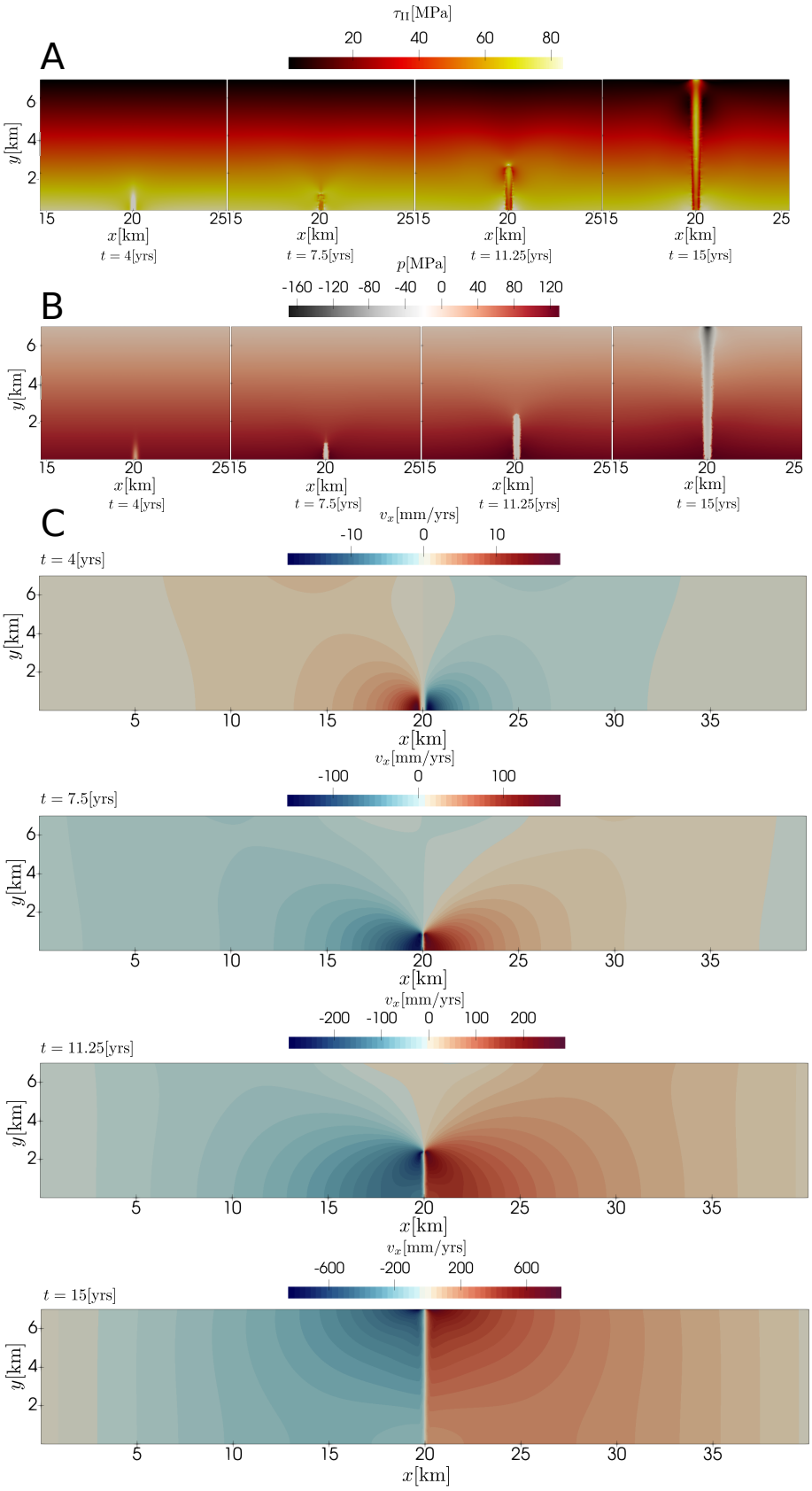

FIGURE 3.11: Snapshots of the same propagating dyke after 4 years, 7.5 years, 11.25 years and 15 years. A: Second invariant of the deviatoric stress. B: Effective pressure. C: Horizontal velocity over the whole system. The color bar for the velocity is updated at each step, as it increases significantly as the dyke progresses toward the surface. Since the dyke is not formed yet, the velocities for $t = 4$[yrs] are simply elastic equilibration of the domain towards the region of lower pressure (the magnitude is also much lower than after the fracture creation).

Supplementary

3.A Stress update derivation

3.A.1 True global pressure scheme

3.A.1.1 Deviatoric constitutive equation

We start by discretizing the stress rate:

$$\overset{\diamond}{\tau}_{ij} = \frac{\tau_{ij} - (\tau_{ij})_n}{\Delta t} + (\tau_{ik})_n \, \omega_{kj} - \omega_{ik} \, (\tau_{kj})_n \, . \tag{3.74}$$

We then take the deviatoric part of plastic flow potential gradient as defined in equation 3.39:

$$\mathrm{dev}\left(\frac{\partial Q}{\partial \sigma_{ij}}\right) = B_\tau \tau_{ij}, \tag{3.75}$$

and insert these two quantities into the deviatoric constitutive equation 3.14 to obtain:

$$\begin{aligned} \dot{\varepsilon}_{ij} - \frac{1}{2G}\left[\frac{\tau_{ij} - (\tau_{ij})_n}{\Delta t} + (\tau_{ik})_n \, \omega_{kj} - \omega_{ik} \, (\tau_{kj})_n\right] - A_\mathrm{D} \, \tau_{ij} \\ - A_\mathrm{N} \, (\tau_\mathrm{II})^{n-1} \, \tau_{ij} - \dot{\lambda} \, B_\tau \tau_{ij} = 0. \end{aligned} \tag{3.76}$$

Rearranging the results yields:

$$\dot{\varepsilon}^*_{ij} - A_\mathrm{L} \, \tau_{ij} - A_\mathrm{N} \, (\tau_\mathrm{II})^{n-1} \, \tau_{ij} - \dot{\lambda} \, B_\tau \tau_{ij} = 0, \tag{3.77}$$

where the effective linear visco-elastic creep pre-factor is:

$$A_\mathrm{L} = \frac{1}{2G\Delta t} + A_\mathrm{D} \tag{3.78}$$

and the effective deviatoric strain rate and rotated old stress are:

$$\dot{\varepsilon}^*_{ij} = \dot{\varepsilon}_{ij} + \frac{\tau^*_{ij}}{2G\Delta t}, \tag{3.79}$$

$$\tau^*_{ij} = (\tau_{ij})_n + \Delta t \left[\omega_{ik} \, (\tau_{kj})_n - (\tau_{ik})_n \, \omega_{kj}\right] . \tag{3.80}$$

From the above equation it becomes obvious that the updated deviatoric stress and the effective strain rate are proportional to each other, hence all the terms can

be replaced with their corresponding scalar norms, the result reads:

$$\dot{\varepsilon}^*_{\mathrm{II}} - A_{\mathrm{L}}\,\tau_{\mathrm{II}} - A_{\mathrm{N}}\,(\tau_{\mathrm{II}})^n - \dot{\lambda}\,A_\tau = 0 \tag{3.81}$$

where:

$$A_\tau = B_\tau \tau_{\mathrm{II}} = \begin{cases} \frac{1}{2}, & \tau_{\mathrm{II}}\,(p_{\mathrm{q}} - p_{\mathrm{d}}) \geq \tau_{\mathrm{d}}\,(p_{\mathrm{q}} - p) \\ \\ \frac{b\,\tau_{\mathrm{II}}}{2\hat{R}_{\mathrm{q}}}, & \text{otherwise} \end{cases}. \tag{3.82}$$

3.A.1.2 Continuity equation

For the bulk equation, following the same steps, we discretize the pressure time derivative:

$$\frac{Dp}{Dt} = \frac{p - p_n}{\Delta t}. \tag{3.83}$$

We then take the spherical part of the plastic flow potential gradient:

$$\mathrm{tr}\left(\frac{\partial Q}{\partial \sigma_{ij}}\right) = 3B_p, \tag{3.84}$$

and insert these two quantities into the mass conservation equation 3.12 gives:

$$\dot{\theta} + \frac{p - p_n}{K\Delta t} - 3\dot{\lambda}B_p = 0, \tag{3.85}$$

that can be rearranged to the following form, for consistency:

$$\dot{\theta}^* + A_{\mathrm{K}}\,p - \dot{\lambda}\,A_p = 0 \tag{3.86}$$

where

$$\dot{\theta}^* = \dot{\theta} - \frac{p_n}{K\Delta t} \tag{3.87}$$

$$A_{\mathrm{K}} = \frac{1}{K\Delta t} \tag{3.88}$$

$$A_p = 3B_p = \begin{cases} k_{\mathrm{q}}, & \tau_{\mathrm{II}}\,(p_{\mathrm{q}} - p_{\mathrm{d}}) \geq \tau_{\mathrm{d}}\,(p_{\mathrm{q}} - p) \\ \\ -\frac{b(p - p_{\mathrm{q}})}{\hat{R}_{\mathrm{q}}}, & \text{otherwise} \end{cases}. \tag{3.89}$$

3.A.1.3 Viscoplastic constitutive equation

Finally, the viscoplastic consitutive equation 3.23 can be recast into residual form:

$$\dot{\lambda} = \frac{\langle F \rangle}{\eta^{\mathrm{vp}}} \rightarrow \langle F \rangle - \dot{\lambda}\, \eta^{\mathrm{vp}} = 0. \tag{3.90}$$

The resulting system of nonlinear stress update equations can be summarized as follows:

$$\dot{\varepsilon}^{*}_{\mathrm{II}} - A_{\mathrm{L}}\, \tau_{\mathrm{II}} - A_{\mathrm{N}}\, (\tau_{\mathrm{II}})^{n} - \dot{\lambda}\, A_{\tau} = 0 \tag{3.91}$$

$$\dot{\theta}^{*} + A_{\mathrm{K}}\, p - \dot{\lambda}\, A_{p} = 0 \tag{3.92}$$

$$\langle F \rangle - \dot{\lambda}\, \eta^{\mathrm{vp}} = 0 \tag{3.93}$$

3.A.2 Trial global pressure scheme

3.A.2.1 Continuity equation

Assuming zero plastic multiplier, the total volumetric strain rate can be expressed in terms of the trial pressure as follows:

$$\dot{\theta} = -\frac{p^{*} - p_{n}}{K \Delta t} \tag{3.94}$$

substituting this expression into the continuity equitation and simplifying, gives:

$$A_{\mathrm{K}}\, p - A_{\mathrm{K}}\, p^{*} - \dot{\lambda}\, A_{p} = 0 \tag{3.95}$$

here we assume that p^{*} is delivered by the global solver and is directly interpreted as a trial pressure.

3.B Jacobian derivation

3.B.1 Assumptions

Star superscripts indicating effective deviatoric ($\dot{\varepsilon}^{*}_{ij}$) and volumetric ($\dot{\theta}^{*}$) strain rates are dropped in this Appendix for notation simplicity. Stress rotation terms are assumed to be constant. Other material dependencies such as strain softening or elastic moduli degradation are also treated explicitly between the time steps and are thus omitted from the linearization given below without loss of generality.

3.B.2 Preliminaries

We first establish the basic derivatives of the unit tensors from the equations 3.5 and 3.6:

$$\frac{\partial \dot{\varepsilon}_{ij}}{\partial \dot{\varepsilon}_{kl}} = \frac{1}{2} \left(\delta_{ik}\delta_{jl} + \delta_{il}\delta_{jk} \right) = I_{ijkl}, \tag{3.96}$$

$$\frac{\partial \dot{\theta}}{\partial \dot{\epsilon}_{kl}} = \delta_{kl}, \tag{3.97}$$

$$\frac{\partial \dot{\varepsilon}_{ij}}{\partial \dot{\epsilon}_{kl}} = I_{ijkl} - \frac{1}{3}\delta_{ij}\delta_{kl} = I^D_{ijkl}. \tag{3.98}$$

Since our constitutive equations are carried out using the second invariant of the deviatoric stress and strain rate tensors, we compute the normalized deviatoric direction tensor and related derivatives:

$$n_{ij} = \frac{\dot{\varepsilon}_{ij}}{\dot{\varepsilon}_{\mathrm{II}}}, \tag{3.99}$$

$$\frac{\partial \dot{\varepsilon}_{\mathrm{II}}}{\partial \dot{\varepsilon}_{kl}} = \frac{1}{2}n_{kl}, \tag{3.100}$$

$$\frac{\partial n_{ij}}{\partial \dot{\varepsilon}_{kl}} = \frac{1}{\dot{\varepsilon}_{\mathrm{II}}}\frac{\partial \dot{\varepsilon}_{ij}}{\partial \dot{\varepsilon}_{kl}} - \frac{\dot{\varepsilon}_{ij}}{\dot{\varepsilon}^2_{\mathrm{II}}}\frac{\partial \dot{\varepsilon}_{\mathrm{II}}}{\partial \dot{\varepsilon}_{kl}} = \frac{1}{\dot{\varepsilon}_{\mathrm{II}}}\left(I_{ijkl} - \frac{1}{2}n_{ij}n_{kl}\right). \tag{3.101}$$

Meanwhile the bulk derivative is simply:

$$\frac{\partial n_{ij}}{\partial \dot{\theta}} = 0. \tag{3.102}$$

3.B.3 True global pressure scheme

3.B.3.1 Local stress update linearization

Directly differentiating the Newton update equations (3.55, 3.47) gives:

$$\mathbf{A} = \begin{bmatrix} \frac{\partial \tau_{\mathrm{II}}}{\partial \dot{\varepsilon}_{\mathrm{II}}} & \frac{\partial \tau_{\mathrm{II}}}{\partial \dot{\theta}} \\ \frac{\partial p}{\partial \dot{\varepsilon}_{\mathrm{II}}} & \frac{\partial p}{\partial \dot{\theta}} \\ \frac{\partial \dot{\lambda}}{\partial \dot{\varepsilon}_{\mathrm{II}}} & \frac{\partial \dot{\lambda}}{\partial \dot{\theta}} \end{bmatrix} = -\mathbf{J}^{-1} \begin{bmatrix} 1 & 0 \\ 0 & 1 \\ 0 & 0 \end{bmatrix} \tag{3.103}$$

.

We compute here the inverse of $\mathbf{J}$ using numerical methods but since it is a three by three matrix, it is possible to express it entirely analytically.

Now that we obtained the necessary elements using the stress invariants, we can compute the strain rate derivative of the deviatoric stress $\left(\frac{\partial \tau_{ij}}{\partial \dot{\epsilon}_{kl}}\right)$ and the volumetric strain rate residuals $\left(\frac{\partial \dot{\theta}_{\mathrm{r}}}{\partial \dot{\epsilon}_{ij}}\right)$.

3.B.3.2 Stress constitutive equation linearization

Let's start with the deviatoric stress:

$$\frac{\partial \tau_{ij}}{\partial \dot{\epsilon}_{kl}} = \frac{\partial \tau_{ij}}{\partial \dot{\varepsilon}_{kl}} \frac{\partial \dot{\varepsilon}_{ij}}{\partial \dot{\epsilon}_{kl}} + \frac{\partial \tau_{ij}}{\partial \dot{\theta}} \frac{\partial \dot{\theta}}{\partial \dot{\epsilon}_{kl}}, \tag{3.104}$$

$$\frac{\partial \tau_{ij}}{\partial \dot{\varepsilon}_{kl}} = \frac{\partial \tau_{\mathrm{II}}}{\partial \dot{\varepsilon}_{kl}} n_{ij} + \tau_{\mathrm{II}} \frac{\partial n_{ij}}{\partial \dot{\varepsilon}_{kl}} \tag{3.105}$$

$$\frac{\partial \tau_{\mathrm{II}}}{\partial \dot{\varepsilon}_{kl}} = \frac{\partial \tau_{\mathrm{II}}}{\partial \dot{\varepsilon}_{\mathrm{II}}} \frac{\partial \dot{\varepsilon}_{\mathrm{II}}}{\partial \dot{\varepsilon}_{kl}}, \tag{3.106}$$

$$\frac{\partial \tau_{ij}}{\partial \dot{\theta}} = \frac{\partial \tau_{\mathrm{II}}}{\partial \dot{\theta}} n_{ij} + \tau_{\mathrm{II}} \frac{\partial n_{ij}}{\partial \dot{\theta}}. \tag{3.107}$$

This gives, once we substitute and simplify:

$$\frac{\partial \tau_{ij}}{\partial \dot{\epsilon}_{kl}} = \frac{1}{2} A_{11} n_{ij} n_{kl} + \frac{\tau_{\mathrm{II}}}{\dot{\varepsilon}_{\mathrm{II}}} \left(I^D_{ijkl} - \frac{1}{2} n_{ij} n_{kl} \right) + A_{12} n_{ij} \delta_{kl}, \tag{3.108}$$

introducing the effective stiffness constants:

$$\eta_{\mathrm{eff}} = \frac{\tau_{\mathrm{II}}}{2\,\dot{\varepsilon}_{\mathrm{II}}}, \tag{3.109}$$

$$\beta_1 = \left(\frac{1}{2} A_{11} - \eta_{\mathrm{eff}} \right), \tag{3.110}$$

$$\beta_2 = A_{12}, \tag{3.111}$$

we can simplify it as:

$$\frac{\partial \tau_{ij}}{\partial \dot{\epsilon}_{kl}} = 2\,\eta_{\mathrm{eff}} I^D_{ijkl} + \beta_1 n_{ij} n_{kl} + \beta_2 n_{ij} \delta_{kl}. \tag{3.112}$$

3.B.3.3 Continuity equation linearization

We can then derive the volumetric strain rate residual linearization, defined as:

$$\dot{\theta}_{\mathrm{r}} = \dot{\theta} + \dot{\theta}_{\mathrm{e}} - \dot{\theta}_{\mathrm{p}}, \tag{3.113}$$

$$\dot{\theta}_{\mathrm{e}} = \frac{p - p_n}{K \Delta t}, \tag{3.114}$$

$$\dot{\theta}_{\mathrm{p}} = \dot{\lambda} A_p. \tag{3.115}$$

Since the elastic strain rate ($\dot{\theta}_{\mathrm{e}}$) depends only on pressure, we can omit it for the derivations. The total ($\dot{\theta}$) and plastic ($\dot{\theta}_{\mathrm{p}}$) strain rates are the sole contributors:

$$\frac{\partial \dot{\theta}_{\mathrm{r}}}{\partial \dot{\epsilon}_{ij}} = \frac{\partial \dot{\theta}}{\partial \dot{\epsilon}_{ij}} - \frac{\partial \dot{\theta}_{\mathrm{p}}}{\partial \dot{\varepsilon}_{kl}} \frac{\partial \dot{\varepsilon}_{kl}}{\partial \dot{\epsilon}_{ij}} - \frac{\partial \dot{\theta}_{\mathrm{p}}}{\partial \dot{\theta}} \frac{\partial \dot{\theta}}{\partial \dot{\epsilon}_{ij}}, \tag{3.116}$$

with

$$\frac{\partial \dot{\theta}_{\mathrm{p}}}{\partial \dot{\varepsilon}_{kl}} = \frac{\partial \dot{\theta}_{\mathrm{p}}}{\partial \dot{\varepsilon}_{\mathrm{II}}} \frac{\partial \dot{\varepsilon}_{\mathrm{II}}}{\partial \dot{\varepsilon}_{kl}}, \tag{3.117}$$

$$\frac{\partial \dot{\theta}_{\mathrm{p}}}{\partial \dot{\varepsilon}_{\mathrm{II}}} = \frac{\partial \dot{\lambda}}{\partial \dot{\varepsilon}_{\mathrm{II}}} A_p + \dot{\lambda} \frac{\partial A_p}{\partial \dot{\varepsilon}_{\mathrm{II}}}, \tag{3.118}$$

$$\frac{\partial \dot{\theta}_{\mathrm{p}}}{\partial \dot{\theta}} = \frac{\partial \dot{\lambda}}{\partial \dot{\theta}} A_p + \dot{\lambda} \frac{\partial A_p}{\partial \dot{\theta}}, \tag{3.119}$$

$$\frac{\partial A_p}{\partial \dot{\varepsilon}_{\mathrm{II}}} = \frac{\partial A_p}{\partial \tau_{\mathrm{II}}} \frac{\partial \tau_{\mathrm{II}}}{\partial \dot{\varepsilon}_{\mathrm{II}}} + \frac{\partial A_p}{\partial p} \frac{\partial p}{\partial \dot{\varepsilon}_{\mathrm{II}}}, \tag{3.120}$$

and

$$\frac{\partial A_p}{\partial \dot{\theta}} = \frac{\partial A_p}{\partial \tau_{\mathrm{II}}} \frac{\partial \tau_{\mathrm{II}}}{\partial \dot{\theta}} + \frac{\partial A_p}{\partial p} \frac{\partial p}{\partial \dot{\theta}}. \tag{3.121}$$

This gives, once we substitute and simplify:

$$\frac{\partial \dot{\theta}_{\mathrm{r}}}{\partial \dot{\epsilon}_{ij}} = \left(1 - \frac{\partial \dot{\theta}_{\mathrm{p}}}{\partial \dot{\theta}}\right) \delta_{ij} - \frac{1}{2} \frac{\partial \dot{\theta}_{\mathrm{p}}}{\partial \dot{\varepsilon}_{\mathrm{II}}} n_{ij}, \tag{3.122}$$

$$\frac{\partial \dot{\theta}_{\mathrm{p}}}{\partial \dot{\theta}} = A_{32} A_p + \dot{\lambda} \left(\frac{\partial A_p}{\partial \tau_{\mathrm{II}}} A_{12} + \frac{\partial A_p}{\partial p} A_{22} \right), \tag{3.123}$$

$$\frac{\partial \dot{\theta}_{\mathrm{p}}}{\partial \dot{\varepsilon}_{\mathrm{II}}} = A_{31} A_p + \dot{\lambda} \left(\frac{\partial A_p}{\partial \tau_{\mathrm{II}}} A_{11} + \frac{\partial A_p}{\partial p} A_{21} \right), \tag{3.124}$$

introducing the effective stiffness constants:

$$\beta_3 = \frac{\partial \dot{\theta}_{\mathrm{p}}}{\partial \dot{\theta}} \tag{3.125}$$

and

$$\beta_4 = \frac{\partial \dot{\theta}_{\mathrm{p}}}{\partial \dot{\varepsilon}_{\mathrm{II}}} \tag{3.126}$$

we can simplify it as:

$$\frac{\partial \dot{\theta}_{\mathrm{r}}}{\partial \dot{\epsilon}_{ij}} = (1 - \beta_3)\, \delta_{ij} - \frac{1}{2} \beta_4 n_{ij}. \tag{3.127}$$

3.B.4 Trial global pressure scheme

3.B.4.1 Local stress update linearization

In this case, the constitutive equations must be derived by the deviatoric strain rate and the trial pressure. Directly differentiating the Newton update equations (3.55, 3.68) gives:

$$\mathbf{A} = \begin{bmatrix} \frac{\partial \tau_{\mathrm{II}}}{\partial \dot{\varepsilon}_{\mathrm{II}}} & \frac{\partial \tau_{\mathrm{II}}}{\partial p^*} \\ \frac{\partial p}{\partial \dot{\varepsilon}_{\mathrm{II}}} & \frac{\partial p}{\partial p^*} \\ \frac{\partial \dot{\lambda}}{\partial \dot{\varepsilon}_{\mathrm{II}}} & \frac{\partial \dot{\lambda}}{\partial p^*} \end{bmatrix} = -\mathbf{J}^{-1} \begin{bmatrix} 1 & 0 \\ 0 & -A_{\mathrm{K}} \\ 0 & 0 \end{bmatrix}. \tag{3.128}$$

3.B.4.2 Stress constitutive equation linearization

We can then compute the stress derivatives with respect to strain rate:

$$\frac{\partial \sigma_{ij}}{\partial \dot{\epsilon}_{kl}} = \frac{\partial \tau_{ij}}{\partial \dot{\epsilon}_{kl}} - \delta_{ij} \frac{\partial p}{\partial \dot{\epsilon}_{kl}}, \tag{3.129}$$

$$\frac{\partial \tau_{ij}}{\partial \dot{\epsilon}_{kl}} = \frac{\partial \tau_{ij}}{\partial \dot{\varepsilon}_{kl}} \frac{\partial \dot{\varepsilon}_{ij}}{\partial \dot{\epsilon}_{kl}}, \tag{3.130}$$

$$\frac{\partial \tau_{ij}}{\partial \dot{\varepsilon}_{kl}} = \frac{\partial \tau_{\mathrm{II}}}{\partial \dot{\varepsilon}_{kl}} n_{ij} + \tau_{\mathrm{II}} \frac{\partial n_{ij}}{\partial \dot{\varepsilon}_{kl}}, \tag{3.131}$$

$$\frac{\partial \tau_{\mathrm{II}}}{\partial \dot{\varepsilon}_{kl}} = \frac{\partial \tau_{\mathrm{II}}}{\partial \dot{\varepsilon}_{\mathrm{II}}} \frac{\partial \dot{\varepsilon}_{\mathrm{II}}}{\partial \dot{\varepsilon}_{kl}}, \tag{3.132}$$

$$\frac{\partial p}{\partial \dot{\epsilon}_{kl}} = \frac{\partial p}{\partial \dot{\varepsilon}_{\mathrm{II}}} \frac{\partial \dot{\varepsilon}_{\mathrm{II}}}{\partial \dot{\varepsilon}_{mn}} \frac{\partial \dot{\varepsilon}_{mn}}{\partial \dot{\epsilon}_{kl}}. \tag{3.133}$$

This gives, once we substitute and simplify:

$$\frac{\partial \sigma_{ij}}{\partial \dot{\epsilon}_{kl}} = 2\,\eta_{\mathrm{eff}} I^D_{ijkl} + \beta_1 n_{ij} n_{kl} + \beta_2 \delta_{ij} n_{kl}, \tag{3.134}$$

where the effective stiffness constants are:

$$\eta_{\mathrm{eff}} = \frac{\tau_{\mathrm{II}}}{2\,\dot{\varepsilon}_{\mathrm{II}}}, \tag{3.135}$$

$$\beta_1 = \left(\frac{1}{2} A_{11} - \eta_{\mathrm{eff}} \right), \tag{3.136}$$

and

$$\beta_2 = -\frac{1}{2} A_{21}. \tag{3.137}$$

Finally, we compute the derivative with respect to global pressure:

$$\frac{\partial \sigma_{ij}}{\partial p^*} = \frac{\partial \tau_{ij}}{\partial p^*} - \delta_{ij} \frac{\partial p}{\partial p^*} \tag{3.138}$$

$$\frac{\partial \tau_{ij}}{\partial p^*} = \frac{\partial \tau_{\mathrm{II}}}{\partial p^*} n_{ij} \tag{3.139}$$

We substitute and rearrange to get:

$$\frac{\partial \sigma_{ij}}{\partial p^*} = \beta_3 n_{ij} + \beta_4 \delta_{ij} \tag{3.140}$$

where the effective constants are:

$$\beta_3 = A_{12} \tag{3.141}$$

and

$$\beta_4 = -A_{22}. \tag{3.142}$$

3.C Finite element formulation

3.C.1 Preliminaries

We first setup the strain rate and stress tensors according to the Voigt notation:

$$\boldsymbol{\tau} = \left[\tau_{xx}, \tau_{yy}, \tau_{zz}, \tau_{xy}, \tau_{xz}, \tau_{yz}\right]^T, \tag{3.143}$$

$$\dot{\boldsymbol{\epsilon}} = \left[\dot{\epsilon}_{xx}, \dot{\epsilon}_{yy}, \dot{\epsilon}_{zz}, \dot{\gamma}_{xy}, \dot{\gamma}_{xz}, \dot{\gamma}_{yz}\right]^T, \tag{3.144}$$

with the shear strain rates defined as:

$$\dot{\gamma}_{xy} = 2\,\dot{\epsilon}_{xy}, \ldots \tag{3.145}$$

The deviatoric strain rate ($\dot{\boldsymbol{\varepsilon}}$) and the volumetric strain rate ($\dot{\theta}$) are accordingly:

$$\dot{\boldsymbol{\varepsilon}} = \mathbf{I}^D\,\dot{\boldsymbol{\epsilon}} = \left[\dot{\varepsilon}_{xx}, \dot{\varepsilon}_{yy}, \dot{\varepsilon}_{zz}, \dot{\varepsilon}_{xy}, \dot{\varepsilon}_{xz}, \dot{\varepsilon}_{yz}\right]^T, \tag{3.146}$$

$$\dot{\theta} = \mathbf{m}^T\,\dot{\boldsymbol{\epsilon}}, \tag{3.147}$$

using the deviatoric projection matrix:

$$\mathbf{I}^D = \mathbf{I} - \frac{1}{3}\mathbf{m}\,\mathbf{m}^T, \quad \mathbf{I} = \frac{1}{2}\begin{bmatrix} 2 & & & & & \\ & 2 & & & & \\ & & 2 & & & \\ & & & 1 & & \\ & & & & 1 & \\ & & & & & 1 \end{bmatrix}, \quad \mathbf{m} = \begin{bmatrix} 1 \\ 1 \\ 1 \\ 0 \\ 0 \\ 0 \end{bmatrix}. \tag{3.148}$$

Next we define in this form the magnitude of deviatoric strain rate tensor and the unit deviatoric tensor similarly to the index notation:

$$\dot{\varepsilon}_{\mathrm{II}} = \sqrt{\frac{1}{2}\left(\dot{\varepsilon}_{xx}^2 + \dot{\varepsilon}_{yy}^2 + \dot{\varepsilon}_{zz}^2\right) + \dot{\varepsilon}_{xy}^2 + \dot{\varepsilon}_{xz}^2 + \dot{\varepsilon}_{yz}^2}, \tag{3.149}$$

$$\mathbf{n} = \frac{\dot{\boldsymbol{\varepsilon}}}{\dot{\varepsilon}_{\mathrm{II}}}. \tag{3.150}$$

We can now define the components of our finite element discretization, starting with the velocity and pressure shape function matrices:

$$\mathbf{N}_v = \begin{bmatrix} N_{v1} & 0 & 0 & \dots \\ 0 & N_{v1} & 0 & \dots \\ 0 & 0 & N_{v1} & \dots \end{bmatrix}, \tag{3.151}$$

$$\mathbf{N}_p = \begin{bmatrix} N_{p1} \dots \end{bmatrix}, \tag{3.152}$$

as well as the differential operator matrix:

$$\mathbf{B} = \begin{bmatrix} \frac{\partial N_{v1}}{\partial x} & 0 & 0 & \dots \\ 0 & \frac{\partial N_{v1}}{\partial y} & 0 & \dots \\ 0 & 0 & \frac{\partial N_{v1}}{\partial z} & \dots \\ \frac{\partial N_{v1}}{\partial y} & \frac{\partial N_{v1}}{\partial x} & 0 & \dots \\ \frac{\partial N_{v1}}{\partial z} & 0 & \frac{\partial N_{v1}}{\partial x} & \dots \\ 0 & \frac{\partial N_{v1}}{\partial z} & \frac{\partial N_{v1}}{\partial y} & \dots \end{bmatrix}. \tag{3.153}$$

Velocity, pressure and strain rates can then be interpolated at the integration points from the element's nodes :

$$\mathbf{v} = \mathbf{N}_v \, \mathbf{v}_e, \tag{3.154}$$

$$p^* = \mathbf{N}_p \, \mathbf{p}_e^*, \tag{3.155}$$

$$\dot{\boldsymbol{\epsilon}} = \mathbf{B} \, \mathbf{v}_e. \tag{3.156}$$

3.C.2 True global pressure scheme

The discretized momemtum and continuity equations are:

$$\mathbf{r}_v = \int_V \mathbf{B}^T \boldsymbol{\tau}\, dV - \int_V \mathbf{B}^T \mathbf{m}\, p^*\, dV - \int_V \mathbf{N}_v^T \mathbf{b}\, dV - \int_S \mathbf{N}_v^T \mathbf{t}\, dS \quad = 0, \tag{3.157}$$

$$\mathbf{r}_p = -\int_V \mathbf{N}_p^T \dot{\theta}_\mathrm{r}\, dV \quad = 0, \tag{3.158}$$

and the Newton - Raphson iterations scheme used the convergence towards the solution: (with k being the iteration index)

$$\begin{bmatrix} \mathbf{v} \\ \mathbf{p}^* \end{bmatrix}_{k+1} = \begin{bmatrix} \mathbf{v} \\ \mathbf{p}^* \end{bmatrix}_k - \begin{bmatrix} \mathbf{K}_{vv} & \mathbf{K}_{vp} \\ \mathbf{K}_{pv} & \mathbf{K}_{pp} \end{bmatrix}_k^{-1} \begin{bmatrix} \mathbf{r}_v \\ \mathbf{r}_p \end{bmatrix}_k . \tag{3.159}$$

The four components of the global jacobian are in this case:

$$\mathbf{K}_{vv} = \int_V \mathbf{B}^T\, \mathbf{D}\, \mathbf{B}\, dV, \tag{3.160}$$

$$\mathbf{K}_{vp} = -\int_V \mathbf{B}^T\, \mathbf{m}\, \mathbf{N}_p\, dV, \tag{3.161}$$

$$\mathbf{K}_{pv} = -\int_V \mathbf{N}_p^T\, \mathbf{q}^T\, \mathbf{B}\, dV, \tag{3.162}$$

$$\mathbf{K}_{pp} = -\int_V \mathbf{N}_p^T\, A_\mathrm{K}\, \mathbf{N}_p\, dV, \tag{3.163}$$

with

$$\mathbf{D} = \frac{\partial \boldsymbol{\tau}}{\partial \dot{\boldsymbol{\epsilon}}}, \tag{3.164}$$

$$\mathbf{q}^T = \frac{\partial \dot{\theta}_\mathrm{r}}{\partial \dot{\boldsymbol{\epsilon}}}, \tag{3.165}$$

being the two quantities derived in the previous appendix. In order to translate them into tensor equations, we expand the linearization in nine-component format to make sure we don't introduce any simplification mistake:

$$\underline{\boldsymbol{\tau}} = \left[\tau_{xx}, \tau_{yy}, \tau_{zz}, \tau_{xy}, \tau_{yx}, \tau_{xz}, \tau_{zx}, \tau_{yz}, \tau_{zy}\right]^T, \tag{3.166}$$

$$\underline{\dot{\boldsymbol{\epsilon}}} = \left[\dot{\epsilon}_{xx}, \dot{\epsilon}_{yy}, \dot{\epsilon}_{zz}, \dot{\epsilon}_{xy}, \dot{\epsilon}_{yx}, \dot{\epsilon}_{xz}, \dot{\epsilon}_{zx}, \dot{\epsilon}_{yz}, \dot{\epsilon}_{zy}\right]^T, \tag{3.167}$$

with the corresponding deviatoric projection matrix and unit deviatoric tensor:

$$\underline{\mathbf{I}}^D = \underline{\mathbf{I}} - \frac{1}{3}\underline{\mathbf{m}}\,\underline{\mathbf{m}}^T, \quad \underline{\mathbf{I}} = \frac{1}{2}\begin{bmatrix} 2 & & & & & & & & \\ & 2 & & & & & & & \\ & & 2 & & & & & & \\ & & & 1 & 1 & & & & \\ & & & 1 & 1 & & & & \\ & & & & & 1 & 1 & & \\ & & & & & 1 & 1 & & \\ & & & & & & & 1 & 1 \\ & & & & & & & 1 & 1 \end{bmatrix}, \quad \underline{\mathbf{m}} = \begin{bmatrix} 1 \\ 1 \\ 1 \\ 0 \\ 0 \\ 0 \\ 0 \\ 0 \\ 0 \end{bmatrix} \tag{3.168}$$

$$\underline{\dot{\boldsymbol{\varepsilon}}} = \underline{\mathbf{I}}^D\,\underline{\dot{\boldsymbol{\epsilon}}} \tag{3.169}$$

$$\underline{\mathbf{n}} = \frac{\underline{\dot{\boldsymbol{\varepsilon}}}}{\dot{\varepsilon}_{\mathrm{II}}} \tag{3.170}$$

We can now proceed to the translation of the equations 3.112 and 3.127:

$$\underline{\mathbf{D}} = 2\,\eta_{\mathrm{eff}}\,\underline{\mathbf{I}}^D + \beta_1\,\underline{\mathbf{n}}\,\underline{\mathbf{n}}^T + \beta_2\,\underline{\mathbf{n}}\,\underline{\mathbf{m}}^T \tag{3.171}$$

$$\underline{\mathbf{q}}^T = (1-\beta_3)\,\underline{\mathbf{m}}^T - \frac{1}{2}\beta_4\,\underline{\mathbf{n}}^T \tag{3.172}$$

We now verify if this corresponds to the 6-elements Voigt notation using a projection matrix:

$$\mathbf{P}^T = \frac{1}{2}\begin{bmatrix} 2 & & & & & & & & \\ & 2 & & & & & & & \\ & & 2 & & & & & & \\ & & & 1 & 1 & & & & \\ & & & & & 1 & 1 & & \\ & & & & & & & 1 & 1 \end{bmatrix}, \tag{3.173}$$

$$\boldsymbol{\tau} = \mathbf{P}^T\underline{\boldsymbol{\tau}}, \tag{3.174}$$

$$\underline{\dot{\boldsymbol{\epsilon}}} = \mathbf{P}\dot{\boldsymbol{\epsilon}}, \tag{3.175}$$

and by applying the chain rule:

$$\mathbf{D} = \frac{\partial\boldsymbol{\tau}}{\partial\underline{\boldsymbol{\tau}}}\frac{\partial\underline{\boldsymbol{\tau}}}{\partial\underline{\dot{\boldsymbol{\epsilon}}}}\frac{\partial\underline{\dot{\boldsymbol{\epsilon}}}}{\partial\dot{\boldsymbol{\epsilon}}} = \mathbf{P}^T\underline{\mathbf{D}}\mathbf{P}, \tag{3.176}$$

$$\mathbf{q}^T = \frac{\partial\dot{\theta}_{\mathrm{r}}}{\partial\underline{\dot{\boldsymbol{\epsilon}}}}\frac{\partial\underline{\dot{\boldsymbol{\epsilon}}}}{\partial\dot{\boldsymbol{\epsilon}}} = \underline{\mathbf{q}}^T\mathbf{P}. \tag{3.177}$$

After substitution, we obtain as results:

$$\mathbf{D} = 2\,\eta_{\mathrm{eff}}\,\mathbf{I}^D + \beta_1\,\mathbf{n}\,\mathbf{n}^T + \beta_2\,\mathbf{n}\,\mathbf{m}^T, \tag{3.178}$$

$$\mathbf{q}^T = (1-\beta_3)\,\mathbf{m}^T - \frac{1}{2}\beta_4\,\mathbf{n}^T. \tag{3.179}$$

Since plastic terms are included in $\dot{\theta}_\mathrm{r}$ (see section 3.3.2.1), the volumetric plasticity is felt in the continuity equation and thus in the K_{pv} component of the global Jacobian.

3.C.3 Trial global pressure scheme

In this case, the discretized momemtum and continuity equations are:

$$\mathbf{r}_v = \int_V \mathbf{B}^T\boldsymbol{\sigma}\,dV - \int_V \mathbf{N}_v^T\mathbf{b}\,dV - \int_S \mathbf{N}_v^T\mathbf{t}\,dS \qquad = 0 \tag{3.180}$$

$$\mathbf{r}_p = -\int_V \mathbf{N}_p^T\dot{\theta}_\mathrm{r}\,dV \qquad = 0 \tag{3.181}$$

and we recall that volumetric strain rate residual $\dot{\theta}_\mathrm{r}$ in the above equation does not include plastic term (see section 3.3.2.2).

As a result, we need different stiffness matrices for the Newton-Raphson iterations defined as (the details of the derivation is similar to the True pressure case):

$$\mathbf{K}_{vv} = \int_V \mathbf{B}^T\,\mathbf{D}\,\mathbf{B}\,dV, \tag{3.182}$$

$$\mathbf{K}_{vp} = -\int_V \mathbf{B}^T\,\mathbf{q}\,\mathbf{N}_p\,dV, \tag{3.183}$$

$$\mathbf{K}_{pv} = -\int_V \mathbf{N}_p^T\,\mathbf{m}^T\,\mathbf{B}\,dV, \tag{3.184}$$

$$\mathbf{K}_{pp} = -\int_V \mathbf{N}_p^T\,A_\mathrm{K}\,\mathbf{N}_p\,dV, \tag{3.185}$$

with

$$\mathbf{D} = \frac{\partial\boldsymbol{\sigma}}{\partial\dot{\boldsymbol{\epsilon}}} = 2\,\eta_\mathrm{eff}\,\mathbf{I}^D + \beta_1\,\mathbf{n}\,\mathbf{n}^T + \beta_2\,\mathbf{m}\,\mathbf{n}^T, \tag{3.186}$$

and

$$\mathbf{q} = \frac{\partial\boldsymbol{\sigma}}{\partial p^*} = \beta_3\,\mathbf{n} + \beta_4\mathbf{m}. \tag{3.187}$$

In this case, plastic terms are not included in the continuity equation and thus the volumetric plasticity is felt in the K_{vp} component of the global Jacobian.

Chapter 4

Summary & Conclusions

This thesis builds towards consistent numerical modeling of magmatic systems through the lithosphere. This domain presents several challenges related to the poor resolution of geophysical imaging techniques and the lack of direct observations of these underground systems. Therefore, using physically consistent numerical models is essential to test hypotheses and constrain geometries and rheological parameters. Two lines of research are explored in this thesis: the use of simple models to extract qualitative and semi-quantitative observations on a volcanic system in the chapter 2, and the implementation of rheologies needed to model dyke propagation in a visco-elastic-plastic host rock in the chapter 3. The next section gives a brief summary of these chapters' main findings.

4.1 The dynamics of magma withdrawal in volcanic chambers

Chapter 2 presents a set of scaling laws to evaluate the melt velocity within a volcanic conduit as a function of the geometry of the magma chamber and mush system, and the rheology of the magma and mush. The first step is to use a numerical finite element code to solve the mass and momentum conservation equations in 2D. The setup considered is a magmatic melt-rich sill at the top of a crystal-rich mush system, connected to the surface by a weak conduit. The geometry of the model is constrained by a few parameters and the rheology of the melt, crystal-rich mush and host rock is approximated as linear viscous. No additional pressure is applied via internal boundary conditions, so the system is buoyancy-driven. Each simulation is run for a single time step and the maximum velocity of the melt rising in the weak conduit is measured and retrieved along the parameters used for the simulation.

We use this model to explore the parameter space and obtain sensitivity coefficients for each parameter. This reveals variations in these sensitivities over the parameter space that can be explained by different advection regimes in the conduit. We then use the obtained sensitivities to derive three scaling laws corresponding to all identified advection modes: a pipe flow, a plume-driven flow, and a convection-driven flow. The boundaries between these advection modes are also derived and presented as a function

of the ratio between the viscosity of the melt and that of the crystal-rich mush, and the ratio between the radius of the sill and the length of the volcanic conduit.

We then discuss the application of these scaling laws. One case proposed is to compute a critical cooling time in the volcanic conduit at which conduction and heat loss is predominant over the advection and the melt crystallizes rather than erupting. We then compare this cooling time with the residence time estimated for a specific volcanic system using the velocities obtained from the scaling laws. The 2021 eruption of the Cumbre Vieja on La Palma is used as an example of a volcanic system that has been the subject of both intensive seismic and petrological investigations. Estimations of the melt rheology, the mush dimensions and emplacement can be obtained from the literature as well as a minimum estimate of the erupted volume. We then compute a first-order estimate of the maximum viscosity of the crystal-rich mush sitting below La Palma. The potential application of our model to a connected network of melt pocket in a transcrustal mush system is also mentioned.

4.2 A numerical method to solve compressible visco-elasto-plastic systems including shear and tensile plasticity

Chapter 3 presents the derivation and implementation of a formulation for tensile plasticity as part of a compressible visco-elasto-plastic rheology for a code solving the mass and momentum conservation equations. We present our derivations in great detail, starting with preliminary definitions and presenting intermediate derivations in the supplementary material of the chapter. We first introduce a general framework using both linear and nonlinear creep laws, deviatoric and compressible elastic moduli, and a viscoplastic regularized plasticity model. We then define a yield function suitable for both shear and tensile plasticity using a classical Drucker-Prager formulation combined with a circular cap connecting the Drucker-Prager cone to the tensile strength of the rock.

We then detail the local stress update implementation. Since we need to account for nonlinearities in both the viscous and plastic rheologies, we need to solve a system of three equations over the variables τ_{II}, p and $\dot{\lambda}$. We propose to do this using Newton-Raphson iterations and provide the necessary Jacobian matrix. We also discuss the best approach to ensure fast convergence of these local iterations by using an appropriate initial guess, solving the visco-elastic system first to obtain a trial stress τ_{II}^{*} and p^{*}, and using a line-search algorithm. Since we obtain an updated pressure from this system of equations each time plasticity is activated, a strategy must be employed to converge the global pressure variable. Here we discuss two different schemes to solve this problem: a true global pressure scheme, where the local stress update is purely strain-driven, and a trial global pressure scheme, where the global pressure corresponds to the visco-elastic trial pressure and serves as a variable to compute the true pressure. After testing both schemes, the latter appeared to be more robust and was used in all subsequent applications.

The local iterations are tested with 0D setups such as volumetric extension, pure shear and mixed strain. We progressively apply stress in the visco-elastic domain until we reach the plastic domain, testing both plasticity's shear and tensile components. We also present two 2D model setups in which we can observe tensile plasticity. One is the extension of an elasto-plastic plate, where we observe the progressive localization of the plastic strain along faults that eventually extend throughout the whole domain. A more efficient localization of the normal faults is also observed for a smaller dilation angle as well as, in all simulations, the presence of vertical cracks at the surface of the domain. The second 2D setup is the nucleation and propagation of a vertical dyke in an elasto-plastic medium. A constant fluid pressure at the bottom of the domain induces a tensile failure. The cracks propagate vertically and we parameterize a pseudo-diffusion scheme for the fluid pressure to follow the plastic failure as a function of the accumulated volumetric plastic strain ($\overline{\theta}^{\mathrm{pl}}$). Both the local and global solvers converge at each time step, even when the dyke divides the domain into two distinct blocks, since the Perzina viscoplasticity dictates the rheology in the fracture. Finally, we discuss the treatment of the global pressure variable, the advantages of using a circular cap on the yield function and the alternative use of an incremental formulation at the global level.

4.3 Conclusions and perspectives

The study of magmatic systems using numerical models is an expanding field in the geosciences as we gain access to better hardware and develop more adapted software. In this thesis, we have presented an application of numerical modeling to better understand how magma rheology and magma chamber structure influence the flow of melt toward an erupting volcano. Although we have simplified the rheology of the material and the geometry of the domain to only a few parameters, we have identified three different advection modes for the melt in the conduit in this study. This illustrates well how even a simplified conceptual model can contain more complexity than one might expect, and how physically consistent models are important to unravel these layers of complexity, from the simplest setups to more elaborate ones. If the extracted scaling laws can make first-order estimates of the structure of the system using data collected by geophysical or geological studies, other questions require the use of more sophisticated models.

The use of volumetric plasticity is rare in geodynamic codes, which tend to focus on solving large-scale tectonic models of converging plates. However, if rock dilation isn't a primary mechanism in this context, it becomes essential when it comes to propagating a viscous melt through the upper crust. Coupling mode-1 plasticity to a code capable of modeling nonlinear viscous fluid advection is thus an important step towards a self-consistent model capable of handling both the vicious propagation of a diapir in the lower crust and the brittle opening of a dyke in the upper crust. We have also illustrated the effect of activating mode-1 plasticity on more classical

geodynamic settings, with the opening of tensile vertical fractures connecting normal faults to the surface of an elasto-plastic crust undergoing extension. The method is described as completely and clearly as possible, using the notation conventions of the geodynamic community, in the hope of providing a comprehensive reading without requiring extensive prior knowledge of the subject.

Finally, the creation of MAGEMin and its efficiency opens many exciting prospects. Coupling thermodynamic computations of complex datasets with a thermo-mechanical model in a (semi)-automatic way would be a revolution in our field. Potential applications exist at all scales, from the chemical segregation of a magmatic chamber to the advection of an ultramafic melt extracted from the mantle and its evolution going through the crust. In general, the methods discussed in this thesis are applicable to many studies, with an emphasis on the interaction of a viscous fluid with an elasto-visco-plastic host rock.

Appendix A

MAGEMin, an efficient Gibbs energy minimizer: application to igneous systems

This chapter has been published in:
Riel, N., Kaus, B. J. P., Green, E. C. R., & Berlie, N. (2022). MAGEMin, an efficient Gibbs energy minimizer: Application to igneous systems. *Geochemistry, Geophysics, Geosystems,23,* e2022GC010427. https://doi.org/10.1029/2022GC010427

Abstract

Prediction of stable mineral equilibria in the Earth's lithosphere is critical to unravel the tectonomagmatic history of exposed geological sections. While the recent advances in geodynamic modelling allow us to explore the dynamics of magmatic transfer in solid mediums, there is to date no available thermodynamic package that can easily be linked and efficiently accounts for the computation of phase equilibrium in magmatic systems. Moreover, none of the existing tools fully exploit single point calculation parallelization which strongly hinders their applicability for direct geodynamic coupling or for thermodynamic database inversions. Here, we present a new Mineral Assemblage Gibbs Energy Minimizer (MAGEMin). The package is written as a parallel C library, provides a direct Julia interface and is callable from any petrological/geodynamic tool. For a given set of pressure, temperature and bulk-rock composition MAGEMin uses a combination of linear programming, extended Partitioning Gibbs Energy and gradient-based local minimization to compute the stable mineral assemblage. We apply our new minimization package to the igneous thermodynamic dataset of (Holland et al., 2018) and produce several phase diagrams at supra-solidus conditions. The phase diagrams are then directly benchmarked against THERMOCALC and exhibit very good agreement. The high scalability of MAGEMin on parallel computing facilities opens new horizons e.g., for modelling reactive magma flow, for thermodynamic dataset inversion and for petrological/geophysical applications.

Plain language summary

Prediction of stable mineral equilibria in the Earth's lithosphere is critical to unravel the tectonomagmatic history of exposed geological sections. While the recent advances in geodynamic modelling allow us to explore the dynamics of magmatic transfer in solid mediums, there is to date no available thermodynamic package that can easily be linked and efficiently accounts for the computation of phase equilibrium in magmatic systems. Moreover, none of the existing tools fully exploit single point calculation parallelization which strongly hinders their applicability for direct geodynamic coupling or for thermodynamic database inversions. Here, we present a new Mineral Assemblage Gibbs Energy Minimizer (MAGEMin). The package is written as a parallel C library, provides a direct Julia interface and is callable from any petrological/geodynamic tool. For a given set of pressure, temperature and bulk-rock composition MAGEMin uses a combination of linear programming, extended Partitioning Gibbs Energy and gradient-based local minimization to compute the stable mineral assemblage. We apply our new minimization package to the igneous thermodynamic dataset of (Holland et al., 2018) and produce several phase diagrams at supra-solidus conditions. The phase diagrams are then directly benchmarked against THERMOCALC and exhibit very good agreement. The high scalability of MAGEMin on parallel computing facilities opens new horizons e.g., for modelling reactive magma flow, for thermodynamic dataset inversion and for petrological/geophysical applications.

A.1 Introduction

The thermodynamic modelling of equilibrium mineral assemblages is a crucial tool for understanding the solid Earth. Mineral equilibrium modelling can be used in an inverse sense, to make inferences about magmatic and tectonic processes based on the rocks that they generated. Used in a forward-modelling sense, our capacity to simulate Earth processes is greater if we can model the most stable mineral assemblage under given conditions, since the mineral assemblage controls or contributes to the thermodynamic, chemical and rheological properties of the rock package. Such modelling thus forms a key step in linking geophysical observations with petrological constraints, and to assess the effect of mineral reactions on deformation of the lithosphere. Even when geological systems are not always at equilibrium, non-equilibrium effects tends to move the system towards equilibrium (Lasaga, 1986), and as such it remains crucial to be able to efficiently model the equilibrium state (e.g., Hou et al., 2021).

In order to model mineral equilibria, an equation of state is needed for each mineral or fluid phase that might potentially be stable under the conditions of interest. The equation of state describes the calorimetric and volumetric properties of the phase as a function of its pressure, temperature, composition and state of order. A phase may be considered to have anything from one compositional components (a pure phase) up

to the maximum number of components in which the rock system is to be modelled. It may or may not contain dimensions of order-disorder. There are several different thermodynamic datasets currently in use that comprise collections of such equations of state, usually aimed at modelling a subset of terrestrial mineral equilibria; for example those of White et al. (2014) (equilibria in metapelites), Green et al. (2016) (equilibria in metabasites), and Stixrude and Lithgow-Bertelloni (2011), Stixrude and Lithgow-Bertelloni (2021) (equilibria among mantle phases). Each collection is calibrated with some degree of internal consistency. In this contribution we use a version of the thermodynamic dataset of Holland et al. (2018), which incorporates the internally-consistent dataset of end-member thermodynamic properties of Holland and Powell (2011) and Tomlinson and Holland (2021). However, our method can also be applied to any other thermodynamic datasets.

Mineral equilibrium calculations for geological applications commonly assume that pressure and temperature are the independent variables in the problem, rather than their conjugates, volume and entropy. Therefore, the equilibrium compositions and states of order for the phases in a model equilibrium are found by minimizing the Gibbs energy, G, of the assemblage. However, minimization of the Gibbs energy in multicomponent and multiphase systems remains one of the most challenging global optimization problems, not only in the fields of metamorphic petrology (e.g., Lanari and Duesterhoeft, 2018), but also for chemical engineering (e.g., Fateen, 2016; Lothenbach et al., 2019) and for the nuclear industry (e.g., Piro, 2011; Piro et al., 2013a). Because the problem is intrinsically multidimensional, non-linear and non-convex, minimization strategies are not guarantee to obtain the global minimum of the Gibbs energy of the system. Consequently, numerous Gibbs energy minimization strategies are used depending on the problem dimensionality (number of chemical components) and complexity of the equations of state. This includes, but is not limited to, equality and non-equality contrained linear least squares (e.g., Ghiorso, 1983; Ghiorso, 1985), linear programming and non-linear optimization methods (e.g., de Capitani and Brown, 1987), discretization of the equations of state in composition–order space combined with linear programming (e.g., Connolly, 1990; Connolly, 2005), linear programming and Partitioning Gibbs Energy (e.g., Piro, 2011; Piro et al., 2013a; Kruskopf and Visuri, 2017), metaheuristic optimization methods (e.g., Teh and Rangaiah, 2002; Burgos-Solórzano et al., 2004; Çetin and Keçebaş, 2021) and Lagrangian formulations (e.g., White et al., 1958; Piro and Simunovic, 2016).

In the geosciences, a number of petrological tools have been developed to predict phase equilibria, study phase relations and produce phase diagrams, e.g., GIBBS (Spear, 1988), THERMOCALC (Powell and Holland, 1988), Perple_X (Connolly, 1990; Connolly, 2005), Theriak-Domino (de Capitani and Brown, 1987; Capitani and Petrakakis, 2010), MELTS and pMELTS (Ghiorso, 1983; Ghiorso, 1985; Ghiorso and Sack, 1995; Asimow and Ghiorso, 1998), GeoPS (Xiang and Connolly, 2021). In general, they fall into two categories (Connolly, 2017; Lanari and Duesterhoeft, 2018): phase equilibrium calculators and Gibbs energy minimizers.

The first category (e.g., THERMOCALC and GIBBS) equate the chemical potentials of components in a specified set of phases, in order to calculate what compositions and states of order the phases must have, to be in equilibrium with each other under the specified conditions. The user may investigate any set of phases for which equations of state are present within the thermodynamic dataset. Conditions to be specified might include pressure, temperature, bulk system composition, or partial phase compositions. Univariant reactions or other phase field boundaries are calculated using geometric constraints (Schreinemakers analysis or related rules) combined with experience and a priori knowledge of the petrological system. This approach allows a wide range of phase diagrams to be calculated, and facilitates the user in exploring any equilibrium of interest, whether stable or metastable. However, in many applications in the geosciences, the only equilibrium of interest is that of the most stable equilibrium at given bulk system composition – or, in geological terms, the most stable equilibrated mineral assemblage in a given bulk rock composition. The phase equilibrium calculator approach is not optimal for this purpose, since it depends on the user anticipating all of the phases that might appear in the stable equilibrium. In complex systems, even an expert user may easily overlook the presence of a phase in a given region of the diagram, and consequently mistake a metastable assemblage for the stable one. Programs in the second category (e.g., MELTS, pMELTS, Theriak-Domino, Perple_X and GeoPS) are designed specifically to predict the most stable assemblage in a given bulk rock composition. At each point on a pressure–temperature grid, these programs explore all possible equilibria among subsets of the phases in a large prespecified list, potentially including all the phases represented in the thermodynamic dataset. They return the subset of these phases that yield the lowest Gibbs energy for the system, along with equilibrium phase compositions and states of order.

Three main Gibbs energy minimization approaches are commonly used in the geosciences. MELTS and pMELTS (Ghiorso, 1983; Ghiorso, 1985; Ghiorso and Sack, 1995; Asimow and Ghiorso, 1998) use Taylor series expansion to express the Gibbs energy of the system and minimize the resulting system of constrained linear equations using least squares methods. However, the thermodynamic datasets hard-wired into MELTS and pMELTS are relatively limited in their application, as they are not appropriate for handling subsolidus equilibria, nor equilibria involving amphibole or biotite. Theriak-Domino uses a combination of linear programming and non-linear local optimization methods (de Capitani and Brown, 1987) to compute the phase equilibria. Perple_X (Connolly, 2005) linearizes the problem by discretizing the equations of state in composition–order space, and solves it using the simplex algorithm. A detailed review of Perple_X and Theriak-Domino methods is presented in Connolly (2017). While these two approaches have proven to be quite reliable and efficient in systems involving a limited number of components, their performance and reliability tends to decrease for higher dimensional systems. For Theriak-Domino the main limitation can be attributed to the absence of constraints during the rotation of the Gibbs-hyperplane between the linear programming and non-linear optimization

stages. For Perple_X, discretization becomes increasingly expensive as the number of compositional components in the equations of state becomes larger. GeoPS (Xiang and Connolly, 2021) has recently been successful in combining these two approaches to provide the community with an efficient petrological program to easily compute phase diagrams. However, none of the above tools are MPI-parallelized for single point calculations, they are not designed to fully exploit high performance facilities, which constitutes a critical limitation for direct coupling with geodynamic modelling. The recent breakthroughs in modelling coupled mechanical and fluid/magma flow systems (e.g., Keller et al., 2013; Taylor-West and Katz, 2015; Keller and Katz, 2016; Keller et al., 2017; Turner et al., 2017; Keller and Suckale, 2019; Rummel et al., 2020; Katz et al., 2022), and, the ongoing open-source movement in the community to simplify and unify modelling tools (e.g., Bezanson et al., 2017, Julia) however, highlight the need for an efficient, open-source and fully parallel mineral assemblage modelling routine.

Here, we describe a new approach, MAGEMin (Mineral Assemblage Gibbs Energy Minimization) (https://github.com/ComputationalThermodynamics/MAGEMin.git), which was developed to provide a minimization routine that is easily callable and fulfils several objectives. First, the package performs single point calculations at given pressure, temperature and bulk-rock composition and finds the thermodynamically most stable assemblage in an automated manner with no required a priori knowledge of the system which is a requirement for integration with geodynamic software. Second, the package has been developed for stability, performance and scalability in complex chemical systems.

Our Gibbs minimization approach combines discretization of the equations of state in composition space (Connolly, 1990) with linear programming (de Capitani and Brown, 1987), and extends the mass constrained Gibbs-hyperplane rotation (Piro et al., 2013a) method to account for the mixing on crystallographic sites that takes place in silicate mineral solid solutions. In this way, we overcome many of the drawbacks of the above-mentioned software packages. Moreover, since the method is developed around point-wise calculations, it is well-suited for parallelization on massively parallel machines and can be combined with an adaptive mesh refinement strategy. We demonstrate the effectiveness of our method by computing a series of phase diagrams using a large thermodynamic dataset native to the THERMOCALC software, and comparing the automatically calculated MAGEMin results with those obtained using THERMOCALC. The definition of the general terminology used in this contribution is given in Table A.1.1 and the definition of the symbols is provided in Table A.2.1.

A.2 Methodology

A.2.1 Gibbs energy formulation

At fixed pressure P and temperature T, the integral Gibbs energy [J] of a multicomponent multiphase system G_{sys} (e.g., Gibbs, 1878; Spear, 1993) can be expressed

TABLE A.1.1: General terminology

Term	Definition
System component	Chemically independent constituent (see Pauken (2011)). The collection of components define the number of chemical dimensions of the system. Here, we use oxides as system components spanning up to 11 dimensions: Na_2O–CaO–K_2O–FeO–MgO–Al_2O_3–SiO_2–TiO_2–Fe_2O_3–Cr_2O_3–H_2O.
Pure phase	(or stoichiometric phase), is a phase that has a fixed composition (or does not vary measurably from its ideal composition) e.g., quartz (SiO_2)
End-member	(or species (Kruskopf and Visuri, 2017) or phase component (Berman, 1991), or vertex of a polytope (Myhill and Connolly, 2021)) is an independent instance of a solution phase (with defined cation occupancy/vacancy on each site) that can be linearly combined with other end-members to span the complete site-occupancy space of a solution
Solution phase	A Solution phase is a mixture of end-members spanning a range of compositions for a single crystal structure (solid solution phase), a fluid or a melt. For instance, in a chemical sub-system restricted to FeO–MgO–SiO_2, the compositional space of olivine is covered by the linear mixture of fayalite (Fe_2SiO4) and forsterite (Mg_2SiO4) end-members. The composition of the end-members are expressed in oxide form (fayalite = 2FeO + SiO_2 and forsterite = 2MgO + SiO_2) but the substitution of Fe and Mg cations occurs in elemental form on the olivine crystallographic site M1 ($[Fe,Mg]^{M1}$ SiO_2)
Pseudosection	(or isochemical equilibrium phase diagram (de Capitani and Brown, 1987)) is a class of phase diagram in pressure-temperature space showing the fields of most stable phase equilibrium for a single bulk-rock composition
Solution phase model	(or equation of state (Powell, 1978)) aims to reproduce the energetic behaviour of naturally occurring mineral, melt, and fluid phases. Depending on the complexity of the phase of interest, the related solution phase model is usually formulated using an ideal and a non-ideal mixing term
Ideal mixing term	The ideal mixing term include both the mechanical mixture contribution, which is the linear combination of the standard Gibbs energy of the end-members, and the configurational energy term which describes the change of energy when the mixture reacts to form a single phase (see Ganguly (2001) and Lanari and Duesterhoeft (2018) for more details)
Non-ideal mixing term	(or excess term) expresses the non-ideal interaction between end-members (see Ganguly (2001))

by:

$$G_{\text{sys}} = \sum_{\lambda=1}^{\Lambda} \alpha_\lambda \sum_{i=1}^{N_\lambda} \mu_{i(\lambda)} p_{i(\lambda)} + \sum_{\omega=1}^{\Omega} \alpha_\omega \mu_\omega, \tag{A.1}$$

where Λ indicates the number of solution phases (mineral phases of variable composition), N_λ the number of end-members of solution phase λ, Ω the number of pure phases (mineral phases of fixed composition, also described as pure phases), α_λ and α_ω are the mole fractions of solution phase λ and pure phase ω, respectively. $p_{i(\lambda)}$ is the fraction of end-member i dissolved in solution phase λ and $\mu_{i(\lambda)}$, μ_ω are the chemical potential of end-member i in solution phase λ and pure phase ω, respectively. An end-member is defined as an independent instance of a solution phase. In a given chemical system, the linear combination of the end-members span the complete crystallographic site-occupancy space of the solution phase.

The chemical potential of a phase is either a constant for a stoichiometric phase (Spear, 1993):

$$\mu_\omega = g^0_\omega, \tag{A.2}$$

or a function for a dissolved end-members within a solution phase (see Ganguly, 2001, for a review)

$$\mu_{i(\lambda)} = g^0_{i(\lambda)} + RT \log(a^{id}_{i(\lambda)}) + g^{\text{ex}}_{i(\lambda)}, \tag{A.3}$$

where R [$\text{Jmol}^{-1}\text{K}^{-1}$] is the ideal gas constant, T [K] is the absolute temperature, $a^{id}_{i(\lambda)}$ is the ideal mixing term, $g^0_{i(\lambda)}$ the Gibbs energy of reference of the pure end-member (Helgeson, 1978; Holland and Powell, 1998) and $g^{\text{ex}}_{i(\lambda)}$ is the excess energy term (Powell and Holland, 1993; Holland and Powell, 2003). The ideal mixing term $a^{id}_{i(\lambda)}$ is generally defined as $a^{id}_{i(\lambda)} = p_{i(\lambda)}$ for molecular mixing, or else for mixing on crystallographic sites as

$$a^{id}_{i(\lambda)} = c_i \prod_s (X^s_{e_{s,i}})^{\nu_s} \tag{A.4}$$

where $X^s_{e_{s,i}}$ is the site fraction of the element $e_{s,i}$ that appears on site s in end-member i of phase λ, ν_s is the number of atoms contained in mixing site s of λ, and c_i is a normalisation constant that ensures that $a^{id}_{i(\lambda)}$ is unity for the pure end-member i. The total Gibbs energy of solution phase λ is given by

$$G_\lambda = \sum_{i=1}^{N_\lambda} \mu_{i(\lambda)} p_{i(\lambda)}. \tag{A.5}$$

At equilibrium, all pure phases and dissolved end-members in a solution phase have to satisfy the Gibbs-Duhem rule (e.g., Spear, 1988; Spear, 1993)

$$\mu_{i(\lambda),\omega} = \sum_{j=1}^{C} a_{i,\omega j} \Gamma_j, \tag{A.6}$$

where Γ_j is the chemical potential of the pure component j. The Gibbs-Duhem rule implies that, at equilibrium, the chemical potential of all end-members of a solution

phase must lie on the Gibbs-hyperplane defined by Γ_j. At specified pressure and temperature, the system must satisfy the Gibbs phase rule (e.g., Spear, 1988; Spear, 1993)

$$F = C - \Phi \geq 0, \tag{A.7}$$

where F is the number of degrees of freedom, C is the number of components (or oxides) and Φ is the total number of phases. Finally, the system must satisfy the mass balance constraint, which implies that the ratio of chemical elements supplied by the phases at their equilibrium compositions and proportions should be equal to that in the specified bulk rock composition b_j

$$\sum_{\lambda=1}^{\Lambda} \alpha_\lambda \sum_{i=1}^{N_\lambda} a_{ij} p_{i(\lambda)} + \sum_{\omega=1}^{\Omega} \alpha_\omega a_{\omega j} - b_j = 0, \tag{A.8}$$

where a_{ij} and $a_{\omega j}$ are composition vectors for the end-member and system components j and $\alpha_{\lambda,\omega} \geq 0$.

A.2.2 Gibbs energy minimization strategy

For any system of fixed bulk composition, pressure and temperature conditions, the general equilibrium conditions are given by minimizing Eq. A.1 while satisfying the Gibbs-Duhem rule (Eq. A.6) and mass constraint (Eq. A.7). This system of equations yields an equality-constrained optimization problem that remains notoriously difficult to solve as it involves a weighted sum of objective functions unevenly spanning the dimensional space. To compute the thermodynamic equilibrium conditions we employ a two-stage algorithm. First, we obtain an initial guess using discretized solution phases (pseudocompounds) and linear programming methods (levelling, Fig. 1A,B) and after which a local minimization of solution phases is coupled with the Partitioning Gibbs Energy method (Piro et al., 2013a) among predicted stable phases (Fig. 1C).

A.2.2.1 Levelling stage

The concept of levelling is to temporarily neglect the thermodynamic contribution from mixing in the solution phases (de Capitani and Brown, 1987; Piro et al., 2013a; Kruskopf and Visuri, 2017). As a consequence, all end-members of solution phases and stoichiometric phases in the system are initially treated as separate pure phases. This allows us to estimate the chemical potential of system components (oxides) and the proportions of the stable pure phases using linear programming methods.

Given this set of artificial "pure phases", the first step of the levelling stage minimizes

$$G^{\text{lvl}} = \min \left(\sum_{\phi=1}^{\Phi} \alpha_\phi g_\phi^0 \right), \tag{A.9}$$

where Φ is the number of active phases equal to the number of system components C, α_ϕ is the fraction of phase ϕ and g_ϕ^0 is the chemical potential of phase ϕ, and, subject

Table A.2.1: Symbols definition

Symbol	Unit	Definition
R	J mol^{-1} K^{-1}	Ideal gas constant
T	K	Temperature
C	-	Total number of chemical components (oxides) in the system
F	-	Number of degrees of freedom (Gibbs-Duhem rule)
j	-	Oxide
b_j	-	Bulk rock composition of oxide j
Φ	-	Total number of active phases
Λ	-	Total number of active solution phases
λ	-	Solution phase
N_λ	-	Number of end-members of solution phase λ
$i(\lambda)$	-	End-member i of solution phase λ
$p_{i(\lambda)}$	mol%	Fraction of end-member i in phase λ
$x_{i(\lambda)}$	-	Penalty formulation for PGE stage of end-member i in phase λ
$x_{k(\lambda)}$	-	Compositional variable k of solution phase λ
Ω	-	Total number of active pure phases
ω	-	Pure phase
α_λ	mol%	Fraction of solution phase λ
α_ω	mol%	Fraction of pure phase ω
a_{ij}	mol	Molar composition of oxide j in end-member i
$a_{\lambda j}$	mol	Molar composition of oxide j in solution phase λ
$a_{\omega j}$	mol	Molar composition of oxide j in pure phase ω
f	-	Normalization factor
a_j	-	Number of atom per oxide j
$e_{i(\lambda)}$	-	Molar composition of end-member i in solution phase λ
ν_s	-	Number of atoms contained in mixing site s of λ
c_i	-	Normalisation constant
G_λ	J	Gibbs energy of the solution phase λ
G^{lvl}	J	Gibbs energy of system during the level stage
G_{sys}	J	Total Gibbs energy of the system
Γ_j	J	Chemical potential of pure oxide j, defining Gibbs-hyperplane
Γ^{lvl}	J	Set of oxide chemical potentials obtained during levelling stage
$g^0_{i(\lambda)}$	J	Gibbs energy of reference of end-member i in phase λ
$a^{id}_{i(\lambda)}$	J	Ideal mixing term
$X^s_{e_{s,i}}$	-	Site fraction of the element $e_{s,i}$ on site s in end-member i of phase λ
$g^{\text{ex}}_{i(\lambda)}$	J	Excess energy term of end-member i in phase λ
$\mu_{i(\lambda)}$	J	Chemical potential of end-member i in phase λ
$\Delta\mu_{i(\lambda)}$	J	Gibbs energy distance of end-member i in phase λ from Gibbs-hyperplane
μ_ω	J	Gibbs energy of pure phase ω
ρ	kg m^{-3}	density
K_b	Pa	Adiabatic bulk modulus
K_s	Pa	Elastic shear modulus
v_p	km s^{-1}	Compressional P-wave velocity
v_s	km s^{-1}	Shear S-wave velocity

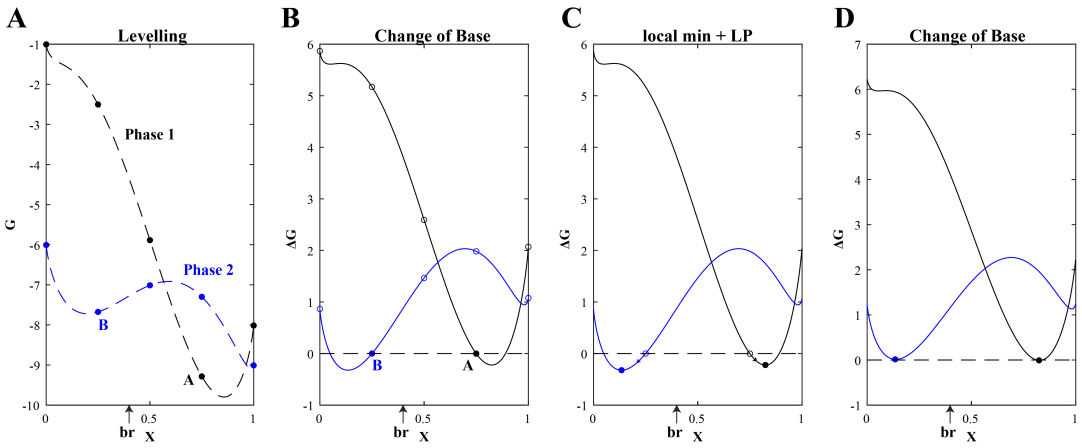

FIGURE A.2.1: Simplified illustration of the minimization strategy, at pressure P=0 GPa and temperature T=1 K, with two solution phases λ_1 and λ_2 (modified after de Capitani and Brown (1987)). Both solution phases include 2 end-members of identical composition C=[1 0; 0 1] (at coordinate X=0.0 and X=1.0). The Gibbs energy of reference of the end-members are: $G0_{i1}^{\lambda 1}$ = -1.0, $G0_{i2}^{\lambda 1}$ = -8.0, $G0_{i1}^{\lambda 2}$ = -6.0 and $G0_{i2}^{\lambda 2}$ = -9.0. The ideal mixing terms are formulated as $RT\log(x)$ with R = 8.134 J/mol/K and T = 1.0 K. The excess terms are calculated as $G_{\text{ex}}^{\lambda 1} = 35.0x_1^2x_2$ and $G_{\text{ex}}^{\lambda 2} = 35.0x_1x_2^2+15.0x_1^2x_2$. The total Gibbs energy of each phase is expressed as $G^{\lambda} = \sum_{i=1}^{N_\lambda} x_i\mu_{i(\lambda)} = \sum_{i=1}^{N_\lambda} x_i\left(G0_i + RT\log(x_i) + G_{\text{ex}}\right)$. A) During the levelling stage the G^{λ} function of each phase is discretized in composition space with a step of 0.25. Then, linear programming is used to find the combination of discrete points minimizing the Gibbs energy of the system $G_{\text{sys}} = G^{\lambda 1} + G^{\lambda 2}$ while satisfying the mass constraint br = [0.6 0.4], here resulting in points A (α=0.7) and B (α=0.3). The Gibbs-hyperplane passing through discrete phases A and B is computed by solving $\Gamma_j = \mathbf{A}^{-1}b$, where $\mathbf{A}$ is the stoichiometry matrix ([0.25 0.75; 0.75 0.25]) and b is the vector of Gibbs energy of discrete points A and B ([-9.2846; -7.6753]). B) The whole system is rotated by recalculating the Gibbs energy curves G^{λ} as $\Delta G^{\lambda} = \sum_{i=1}^{N_\lambda} x_i\left(G0_i - \sum_{j=1}^{C}\Gamma_j a_{ij} + RT\log(x_i) + G_{\text{ex}}\right)$, where Γ_j = [-6.8706; -10.0893] and a_i is the compositional vector of end-member i. This step effectively levels the plane passing through points A and B to the horizontal i.e., $\Delta G^{\lambda A,B}$ = 0.0. C) Starting from discrete points A and B (empty black and blue circles) a gradient-based method is used to find the minimum of phases λ_1 and λ_2 (X_1 = 0.8242 and X_2 = 0.1345). D) Using the minimized points the Gibbs plane is rotated again ($\Delta\Gamma_j$ = [-0.3631; -0.1806], Γ_j=Γ_j + $\Delta\Gamma_j$) and for this simplified case-study, the system is considered to have converged, as there are no phases left for which ΔG<0. The phase fractions are retrieved as $\alpha_{\lambda 1,2}$=$\mathbf{A}^{-1}br$ ($\alpha_{\lambda 1}$ = 0.3850 and $\alpha_{\lambda 2}$ = 0.6151). Note that in our formulation, unlike in de Capitani and Brown (1987), the update of the Gibbs-hyperplane defined by $\Delta\Gamma_j$ is achieved using the PGE approach (Eqs. A.26, A.27 and A.28) modified for mixing on crystallographic sites.

to the mass balance constraint

$$\sum_{\phi=1}^{\Phi} \alpha_\phi a_{\phi j} - b_j = 0, \tag{A.10}$$

where $a_{\phi j}$ is the composition vector of the phase ϕ and $\alpha_\phi \geq 0$. Equations A.9 and A.10 are solved using the linear programming method adapted from de Capitani and Brown (1987) with a special case of the simplex method (Dantzig, 1963). Upon convergence, the chemical potential of the system components defining the Gibbs-hyperplane are retrieved such as

$$\Gamma^{\text{lvl}} = A^{-1} G^{\text{lvl}}, \tag{A.11}$$

where A is the stoichiometry matrix of the predicted stable pure phases and G^{lvl} is the Gibbs energy vector of the same set of pure phases.

During the second step of the levelling stage, solution phases are discretized (pseudocompound) and only the pseudocompounds located close or below the Gibbs-hyperplane defined by Γ^{lvl} are further considered for a second round of linear programming. The distance of a pseudocompound with respect to the Gibbs-hyperplane is calculated as

$$\Delta G_\lambda = \sum_{j=1}^{C} a_{\lambda j} \Gamma_j^{\text{lvl}} - G_\lambda, \tag{A.12}$$

where $a_{\lambda j}$ is the composition and G_λ is the Gibbs energy of the pseudocompound.

Likewise, the distance from the Gibbs-hyperplane can be calculated for each end-member dissolved in a solution phase from

$$\Delta\mu_{i(\lambda)} = \mu_{i(\lambda)} - \sum_{j=1}^{C} a_{\lambda j}\Gamma_j = g^0_{i(\lambda)} + RT\log(a^{id}_{i(\lambda)}) + g^{\text{ex}}_{i(\lambda)} - \sum_{j=1}^{C} a_{\lambda j}\Gamma_j. \tag{A.13}$$

Cycling through the list of pseudocompounds is achieved until no remaining pseudocompound is left with a negative $\Delta G_\lambda \leq -10^{-6}$. The levelling stage is then successfully terminated and the Partitioning Gibbs Energy (PGE) stage is initiated.

A.2.2.2 Partitioning Gibbs energy (PGE) stage

The Partitioning Gibbs Energy (PGE) approach (e.g., Piro et al., 2013a; Kruskopf and Visuri, 2017) has the objective to partition the Gibbs energy of the system among the system components (i.e., Γ_j) by expressing the end-member fraction of the mass balance (Eq. A.8) as function of the chemical potential of the end-members (Eq. A.3). The key advantage of this approach is that a change in Γ_j (which we attempt to find) is directly coupled to the composition of the system, which helps the optimisation process.

For an non-ideal solution model where the ideal mixing term only depends on the end-member fraction (and not the site-fractions) Piro et al. (2013a) first expresses the

chemical potential of the end-members as function of the Gibbs-Duhem relation by substituting Eq. A.6 in Eq. A.3 yielding

$$\sum_{j=1}^{C} a_{i(\lambda),j}\Gamma_j = g^0_{i(\lambda)} + RT\log(x_{i(\lambda)}) + g^{\text{ex}}_{i(\lambda)}. \tag{A.14}$$

Solving this for $x_{i(\lambda)}$ gives

$$x_{i(\lambda)} = \exp\left(\left(\sum_{j=1}^{C} a_{\lambda j}\Gamma_j - g^0_\lambda - g^{\text{ex}}_\lambda\right)/(RT)\right), \tag{A.15}$$

which is a direct expression of the end-member fraction $x_{i(\lambda)}$ as function of its chemical potential and the chemical potential of the pure components of the system Γ_j. This expression is then substituted into the mass balance equation (Eq. A.8) yielding a set of equations (one per component) in the PGE form:

$$\sum_{\lambda=1}^{\Lambda}\alpha_\lambda\sum_{i=1}^{N_\lambda} a_{ij}\exp\left(\left(\sum_{j=1}^{C} a_{\lambda j}\Gamma_j - g^0_\lambda - g^{\text{ex}}_\lambda\right)/(RT)\right) + \sum_{\omega=1}^{\Omega}\alpha_\omega a_{\omega j} - b_j = 0, \tag{A.16}$$

This formulation has proven to be very successful in large chemical systems involving as many as 118 components (Piro, 2011) and relatively simple ideal and non-ideal solution models (Piro et al., 2013a; Kruskopf and Visuri, 2017), allowing to model for the first time the temporal and spatial evolution of coupled thermochemical and nuclear reactions of irradiated fuel (Piro et al., 2013b).

However, this formulation cannot be directly applied to more complex solid solutions, in which mixing-on-sites must be considered, yielding an ideal entropy term that must be written in terms of site fractions (Eq. A.4). To extend the PGE approach to account for solution models involving site-fractions, we expand the ideal mixing term as

$$RT\log(a^{id}_{i(\lambda)}) = RT\log(x_{i(\lambda)}) + RT\log\left(\frac{a^{id}_{i(\lambda)}}{p_{i(\lambda)}}\right), \tag{A.17}$$

where $x_{i(\lambda)} = p_{i(\lambda)}$, which gives using Eq. A.3 and the Gibbs-Duhem relation of Eq. A.6

$$RT\log(x_{i(\lambda)}) = \sum_{j=1}^{C} a_{i(\lambda)j}\Gamma_j - g^0_{i(\lambda)} - RT\log\left(\frac{a^{id}_{i(\lambda)}}{p_{i(\lambda)}}\right) - g^{\text{ex}}_{i(\lambda)}. \tag{A.18}$$

Developing the log term of the right side of Eq. A.18 gives

$$RT\log(x_{i(\lambda)}) = \sum_{j=1}^{C} a_{i(\lambda)j}\Gamma_j - g^0_{i(\lambda)} - RT\log(a^{id}_{i(\lambda)}) - g^{\text{ex}}_{i(\lambda)} + RT\log(p_{i(\lambda)}), \tag{A.19}$$

which can be simplified using Eq. A.13 as

$$\log(x_{i(\lambda)}) = -\frac{\Delta\mu_{i(\lambda)}}{RT} + \log(p_{i(\lambda)}), \tag{A.20}$$

and rearranged as

$$x_{i(\lambda)} = \exp\Big(-\frac{\Delta\mu_{i(\lambda)}}{RT}\Big)p_{i(\lambda)}, \tag{A.21}$$

where $x_{i(\lambda)}$ is the expression for end-member fraction used in the subsequent PGE formulation and $p_{i(\lambda)}$ is the end-member fraction as computed by the solution phase model. After the levelling stage, and as long as the Gibbs-Duhem constraint is not respected, $\Delta\mu_{i(\lambda)} \neq 0$ and $x_{i(\lambda)} \neq p_{i(\lambda)}$. During the course of the PGE iterations, the term $\exp\Big(-\frac{\Delta\mu_{i(\lambda)}}{RT}\Big)$ tends to 1.0 as $\Delta\mu_{i(\lambda)}$ tends to 0.0, which enforces that at convergence the chemical potential of all the endmembers of predicted stable solution phases lie on the Gibbs-hyperplane (Gibbs-Duhem rule) and that $x_{i(\lambda)} = p_{i(\lambda)}$. The exponential dependency of $x_{i(\lambda)}$ on $\mu_{i(\lambda)}$ imposes the Gibbs-hyperplane computed during levelling to be sufficiently close to solution to ensure convergence.
Eq. (A.21) is then substituted in Eq. (A.8) yielding

$$\sum_{\lambda=1}^{\Lambda}\alpha_\lambda\sum_{i=1}^{N_\lambda}a_{ij}x_{i(\lambda)} + \sum_{\omega=1}^{\Omega}\alpha_\omega a_{\omega j} - b_j = 0, \tag{A.22}$$

which has the advantage that it effectively couples the mass balance constraint (Eq. A.8) and the chemical potential of pure components (Eq. A.6) (Piro et al., 2013a; Kruskopf and Visuri, 2017). Additionally, the sum of the end-member fractions of a solution phase must equal unity at convergence i.e.

$$\sum_{i=1}^{N_\lambda}x_{i(\lambda)} - 1 = 0, \tag{A.23}$$

and the stoichiometric phases must lie on the Gibbs-hyperplane i.e.

$$\sum_{j=1}^{C}a_{\omega j}\Gamma_j - g^0_\omega = 0. \tag{A.24}$$

This results in the following system of equations

$$f_v = \sum_{\lambda=1}^{\Lambda}\alpha_\lambda\sum_{i=1}^{N_\lambda}a_{ij}x_{i(\lambda)} + \sum_{\omega=1}^{\Omega}\alpha_\omega a_{\omega j} - b_j, \tag{A.25}$$

$$h_l = \sum_{i=1}^{N_\lambda}x_{i(\lambda)} - 1, \tag{A.26}$$

$$q_k = \sum_{j=1}^{C}a_{\omega j}\Gamma_j - g^0_\omega. \tag{A.27}$$

Eqs. A.25, A.26 and A.27 are solved using a Newton-Raphson approach such as

$$\mathbf{J}\Delta y = -F, \tag{A.28}$$

where $\mathbf{J}$ is the Jacobian of the system of equations f_v, h_l and q_k expressed as

$$\mathbf{J} = \begin{pmatrix} \frac{\partial f_v}{\partial \Gamma_j} & \frac{\partial f_v}{\partial \alpha_\lambda} & \frac{\partial f_v}{\partial \alpha_\omega} \\ \frac{\partial h_l}{\partial \Gamma_j} & \frac{\partial h_l}{\partial \alpha_\lambda} & \frac{\partial h_l}{\partial \alpha_\omega} \\ \frac{\partial q_k}{\partial \Gamma_j} & \frac{\partial q_k}{\partial \alpha_\lambda} & \frac{\partial q_k}{\partial \alpha_\omega} \end{pmatrix} = \begin{pmatrix} \sum_{\lambda=1}^{\Lambda} \alpha_\lambda \sum_{i=1}^{N_\lambda} x_{i(\lambda)} a_{ij} a_{iv} & \sum_{i=1}^{N_\lambda} x_{i(\lambda)} a_{ij} & a_{\omega j} \\ \sum_{i=1}^{N_\lambda} x_{i(\lambda)} a_{ij} & 0 & 0 \\ a_{\omega j} & 0 & 0 \end{pmatrix}, \tag{A.29}$$

F is the residual vector defined as

$$F = (f_1, ..., f_C, h_1, ..., h_\Lambda, q_1, ..., q_\Omega), \tag{A.30}$$

and Δy is the set of variable we solve for

$$\Delta y = (\Delta\Gamma_1, ..., \Delta\Gamma_C, \Delta\alpha_1, ..., \Delta\alpha_\Lambda, \Delta\alpha_1, ..., \Delta\alpha_\Omega). \tag{A.31}$$

At the beginning of a PGE iteration, all considered solution models are minimized while taking inequality constraints into account. In MAGEMin, we employ the optimization library NLopt (Johnson, 2021) and the gradient-based CCSAQ algorithm (Svanberg, 2002). This algorithm supports inequality constraints which is a requirement to minimize the solution models as the ideal mixing term is function of the site-fractions which have to be ≥ 0. An example of a solution model derivation for a gradient-based inequality constraint optimization is given in the Appendices.

Subsequently, Eq. A.28 is solved and the set of variables is updated as $y^1 = y^0 + \tau\Delta y$ where τ is an under-relaxing factor defined as

$$\tau = \min\left(\frac{\frac{0.025}{\delta}}{\left\| \alpha_{\lambda,\omega}^{\max} \right\|_2^2}, \frac{\frac{2.5}{\delta}}{\left\| \Gamma_j^{\max} \right\|_2^2}, 1.0 \right), \tag{A.32}$$

where

$$\delta = 192.0 e^{\left[-8.0 \cdot \left(\|\Delta b_j\|_2^2\right)^{0.26}\right]} - 1.0, \tag{A.33}$$

is an inner under-relaxing factor linked to the residual norm of the mass constraint. Effectively, δ decreases the maximum allowed step size of $\Delta\Gamma_j$ and $\Delta\alpha_{\lambda,\omega}$ when the norm of the mass constraint decreases. δ has been optimized in a manual manner across the pseudosections presented in this study to increase the performances and stability of the computation. We choosed this option because the use of backtracking line search methods has proven to be rather inefficient as, in order to converge, the system has to be able to temporarily relax constraints. Although the current definition of δ makes it a proud member of the family of "magic" number, we find that the

minimization results remain quite consistent, as long as the relaxing factor is small enough.

During the iterations, a phase is removed from the active assemblage when its fraction is ≤ 0.0 and a phase is added when its driving force ΔG_λ is ≤ 0.0 i.e., the phase has a lower energy than/or is lying on the Gibbs-hyperplane.

The system is considered to have converged when the norm of the mass balance residual vector, the residual of the sum of the end-member fractions and the driving force of the solution phases are lower than 10^{-5}.

A.2.2.3 Solution phase solvi

Solvi are regions of unmixing within a solution. They can be detected when a stable or metastable assemblage contains two distinct phases with the same structure but different composition, such as co-existing augite and pigeonite for clinopyroxene (e.g. (Gasparik, 2014)). Computationally, the two phases are represented by local minima at two different compositions within a single isobaric-isothermal G-surface of an equation of state. They are handled in several ways.

Firstly, after the levelling stage, if multiple discretized points on the G-surface of the same solution phase are predicted in the stable mineral assemblage they are initially all treated as potential solvi candidates. Subsequently, they are merged after the local minimization step if they converge to the same local minimum ($\|\Delta x_k\|_2^2 \leq 10^{-2}$).

Secondly, during the course of the PGE iterations a solution phase can be duplicated and checked for solvi when its active set of compositional variables is too far from its starting values i.e.,

$$\left\|x_\lambda^t - x_\lambda^0\right\|_2^2 \geq x_{\text{step}}\sqrt{N_x}, \tag{A.34}$$

where x_λ^t is the actual set of compositional variables, x_λ^0 is the initial set of compositional variables, N_x is the number of compositional variables of solution phase λ and x_{step} is the discretization step of the solution phase λ.

Finally, when getting close to solution $\Delta b_j \leq 10^{-4}$ discretized points of solution phases close to the Gibbs-hyperplane but compositionally away from the active solution phase are locally minimized. In the event the driving force of a tested point $\Delta G_\lambda^{\text{tested}} \leq 0.0$, the point is added to the system. The latter strategy ensures that solvi are not overlooked and that the system converges toward global minimum (no phase lies below the Gibbs-hyperplane).

A.2.2.4 Failed minimization contingency plan

While local minimization using NLopt (Johnson, 2021) and CCSAQ algorithm (Svanberg, 2002) has proven to be quite efficient and reliable, in some cases the site-fraction inequality constraints can be slightly violated which lead to wrong values of ΔG_λ and $\Delta \mu_{i(\lambda)}$ and therefore to divergence of the overall algorithm.

In order to avoid this, site-fractions are tested after every local minimization of solution phases and in the event a site-fraction is violated, the set of compositional variables is brought back to the feasible domain using the nullspace formulation described in Feppon et al. (2020) such as

$$\Delta x_k = -\alpha_c\Big(\mathbf{G}^T(\mathbf{G}\mathbf{G}^T)^{-1}g\Big), \tag{A.35}$$

where Δx_k is the compositional variable step toward the feasible domain, g is a vector of violated site-fraction constraints, $\mathbf{G}$ is the Jacobian of the violated site-fractions and $\alpha_c = 0.1$ is an under-relaxing factor. This approach proved to be robust and the solution phase is generally brought back into the feasible domain within 4-5 iterations.

In the event convergence is not achieved using the default tolerance, the tolerance can be relaxed by up to one order of magnitude ($\leq 2\times10^{-4}$). If convergence is still not obtained, the minimization is considered to have failed. In all cases a code, MAGEMin sends back the status of the minimization (0, success; 1, relaxed tolerance; 2, failure).

A.2.3 Dataset implementation

In order to improve performance and benchmark the results with THERMOCALC, the thermodynamic dataset used natively in THERMOCALC was translated directly into C routines for MAGEMin, and implemented without transformation of variables or coordinate systems. This eliminates inconsistencies and minimizes the risk of introducing mistakes. Appendix A gives an overview of equation of state construction in the thermodynamic dataset.

A.2.4 Normalization for mass balance

Like THERMOCALC, MAGEMin accepts input bulk compositions expressed in terms of normalised numbers of oxide units (SiO_2, Al_2O_3, CaO, ...). However, the phases present in the system at equilibrium will in general be written on a variety of formula units (e.g. (Mg,Fe,Ca)(Mg,Fe)SiO_4, (K,Na,Ca,Mg,Fe)(Mg,Fe,Al,Fe^{3+},Cr)(Si,Al)$_2O_6$, ...). In order to be able to compare the amounts of phases present in a meaningful way, MAGEMin follows THERMOCALC in expressing the amounts of phases present on a 1-atom basis. The Gibbs energies of phases must therefore be normalized.

The normalized Gibbs energy of a model solution phase is expressed as

$$fG_\lambda = f\sum_{i=1}^{N_\lambda}\mu_{i(\lambda)}p_{i(\lambda)}, \tag{A.36}$$

where f is the normalization factor defined as

$$f = \frac{\sum_{j=1}^{C} b_j a_j}{\sum_{i=1}^{N_\lambda} p_{i(\lambda)} \sum_{j=1}^{C} e_{i(\lambda)j} a_j}, \tag{A.37}$$

where a_j is the number of atom per oxide and e_i is the molar composition of end-member i of solution phase λ.

The first derivative of the objective function (Eq. A.5), necessary to conduct gradient-based minimization, is computed using the chain rule as

$$\frac{\partial f G_\lambda}{\partial x_k} = \left(\mu_{i(\lambda)} - \frac{\sum_{j=1}^{C} e_{i(\lambda)j} a_j}{\sum_{l=1}^{N_\lambda} \sum_{j=1}^{C} e_{l(\lambda)j} a_j} G_\lambda \right) f \frac{\partial p_{i(\lambda)}}{\partial x_k}, \tag{A.38}$$

where x_k are the compositional variables of solution phase λ.

A.2.5 Solution phase discretization

The set of pseudocompounds used during the first levelling stage (§2.2.1) and tested when getting close to convergence, is pre-computed using a python Jupyter-Notebook and implemented as C functions to improve performance. The discretization step for each solution phase is chosen to be $0.05 \leq \Delta x_k^{\text{step}} \leq 0.33$ such that the total number of discrete points per solution phase ranges between 100 and 6000 depending of the number of compositional variables (dimensionality). The currently used compositional variables steps for the discretization of the solution phases are: spn, 0.199; bi, 0.124; cd, 0.098; cpx, 0.249; ep, 0.049; g, 0.198; hb, 0.329; ilm, 0.049; liq, 0.198; mu, 0.198; ol, 0.098; opx, 0.249; pl4T, 0.049; as fl is largely dominated by water we only use one pseudocompound made of 100% of the pure water endmember.

A.3 Algorithm demonstration

To demonstrate how the extended PGE algorithm compares to a linear programming (Theriak-Domino) approach, we present a simplified application in the Na_2O–CaO–K_2O–Al_2O_3–SiO_2 (NCKAS) chemical system. This application includes two pure phases, sillimanite and quartz, and activity–composition (a–x) relations for feldspar (pl4T)(Holland et al., 2021). The bulk-rock composition used in this example is presented in Table A.4.1 as "demo" and the pressure and temperature conditions are fixed at 600 °C and 0.3 GPa.

The results of the Gibbs energy minimization are shown in figure (A.3.1). At equilibrium the Gibbs energy of the system is -1080.8358 J and the mineral assemblage is characterized by quartz (8.123 mol%), sillimanite (9.614 mol%) and two feldspar (41.084 and 41.179 mol%) (Fig. A.3.1). Although both the LP and the PGE methods give very similar results and both exhibit super-linear convergence (Fig. A.3.1B), important differences can be observed. First, the residual on the chemical potential of the system components $\|\Gamma_j\|_2^2$ is, at convergence, one order of magnitude lower with the PGE method (Fig. A.3.1B). Note that the absolute accuracy is controlled by the tolerance of the non-linear optimizer. Here 10^{-10} was used with fmincon MATLAB solver. Secondly, on a log10 basis, the PGE convergence profile is piece-wise linear while the LP profile exhibits significant oscillations (Fig. A.3.1B). The LP oscillations

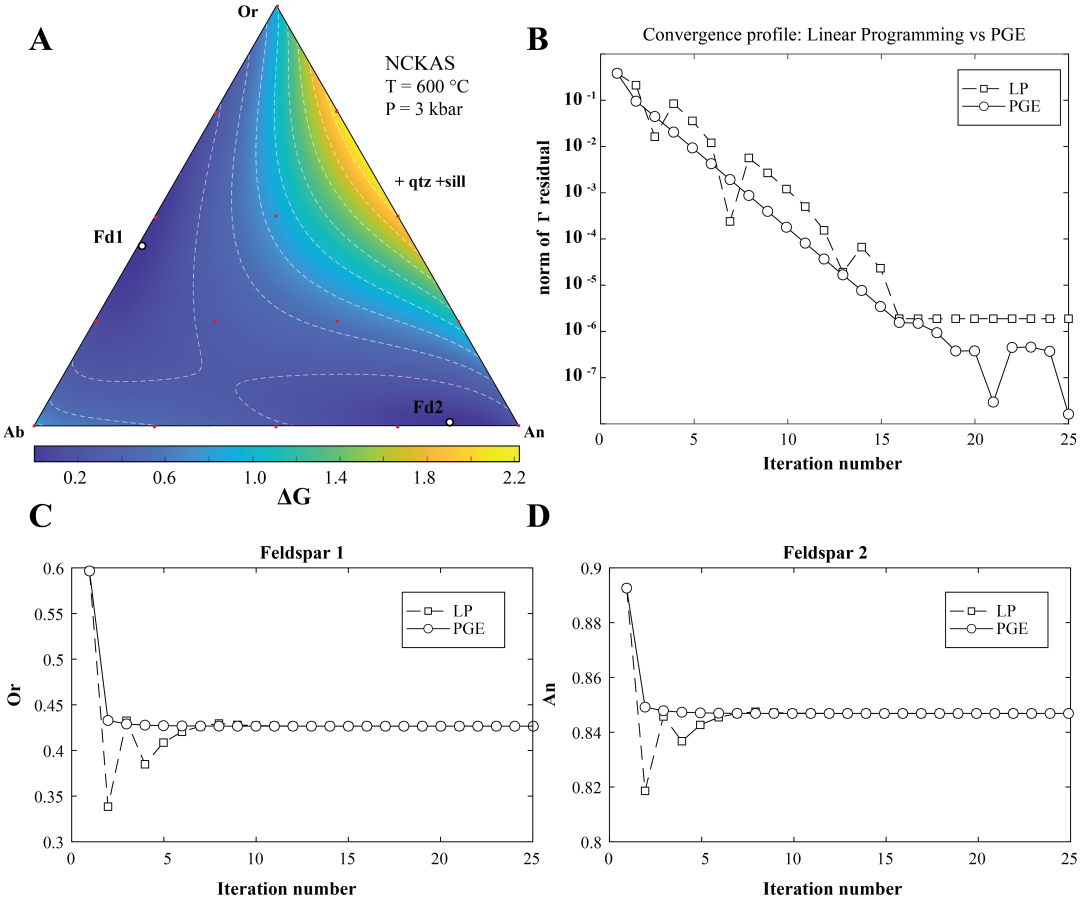

FIGURE A.3.1: Comparison of Linear Programming (LP) versus the extended Partitioning Gibbs Energy (PGE) approach. A, ΔG energy of the ternary feldspar at equilibrium. "Fd1" and "Fd2" are the two feldspar phases coexisting at equilibrium. The red dots represent the starting set of discretized points of the feldspar solution model for both LP and PGE approach. B, Comparison of the convergence profile between LP and extended PGE approaches. C. Orthose-content of feldspar 1 as function of the minimization iteration. D. Anorthite-content of feldspar 2 as function of the minimization iteration.

are caused by under/overshooting during local minimization A.3.1C,D) which is not observed for the PGE approach (Figs. A.3.1C,D).

This key difference in convergence behavior between the LP and the PGE methods is related to how the Gibbs-hyperplane is rotated after the gradient-based minimization stage. For the LP method, rotation is achieved by using the Gibbs energy of the minimized points irrespective of the chemical potential of their constitutive endmembers (see Eq. A.9). Instead, for the extended PGE approach, the rotation is conducted by solving the mass constraint equation where the endmember fractions are penalized using the chemical potentials of the endmembers (see Eq. A.8). The additional constraint drive the rotation of the Gibbs-hyperplane in a direction that also decreases the Gibbs-Duhem residual of all species i.e., that the Gibbs-hyperplane of each individual solution phase is rotated to be become parallel to the system Gibbs-hyperplane. This efficiently removes under/overshooting during the non-linear stage (Figs. A.3.1C,D).

This example has been performed with MATLAB using the optimization toolbox and the script is available at https://github.com/ComputationalThermodynamics/sandbox.git

A.4 Application to igneous systems

Below we demonstrate our approach by presenting a variety of phase diagrams calculations, which we compare with the output from THERMOCALC. Pseudosections map the most stable phase equilibrium to occur in a specified bulk-rock composition, as a function of pressure and temperature. The bulk compositions used in our calculations are shown in Table A.4.1, and are defined in the systems Na_2O–CaO–K_2O–FeO–MgO–Al_2O_3–SiO_2–TiO_2–Fe_2O_3–Cr_2O_3 (NCKFMASTOCr; "dry"), or NCKFMASTOCr+H_2O (NCKFMASHTOCr; "wet").

We used a thermodynamic dataset based on that of Holland et al. (2018), including the minor published updates to the equations of state for solution phases current as of 23 Jan 2022 (see http://hpxeosandthermocalc.org). The updates include a change in the feldspar equation of state to that of Holland et al. (2021). We used version 6.34 of the internally-consistent dataset of end-member thermodynamic properties (Tomlinson and Holland, 2021). The thermodynamic dataset as a whole includes equations of state for the pure stoichiometric phases quartz (q), cristobalite (crst), tridymite (trd), coesite (coe), stishovite (stv), kyanite (ky), sillimanite (sill), andalusite (and), rutile (ru) and sphene (sph). It also represents the solution phases spinel (spn), biotite (bi), cordierite (cd), clinopyroxene (cpx), orthopyroxene (opx), epidote (ep), garnet (g), hornblende (hb), ilmenite (ilm), silicate melt (liq), muscovite (mu), olivine (ol), ternary feldspar (pl4T), and aqueous fluid (fl). An outline of the construction of the thermodynamic dataset is given in Appendix A. Full documentation and THERMOCALC input files for the thermodynamic dataset can be downloaded from http://hpxeosandthermocalc.org, designated as an accompaniment to this paper.

A.4.1 Example pseudosections

Pseudosections were computed using MAGEMin and processed using an MATLAB Graphical User Interface that employs adaptive mesh refinement similar to what is done in Perple_X (Connolly, 2005)(Fig. 2). The MATLAB application sends a list of pressure-temperature points to MAGEMin for a specified bulk-rock composition and receives back the stable phase mineral assemblage. MAGEMin is parallelized using MPI and can therefore take advantage of multicore processor architectures or be deployed on local or larger remote computing servers.

In total, 6 pseudosections are presented: KLB-1 peridotite (e.g., Takahashi, 1986), RE46 Icelandic basalt (Yang et al., 1996), water-oversaturated tonalite 101 (Piwinskii, 1968), wet basalt and two additional N-MOR basalt (Gale et al., 2013) and MIX1G pyroxenite (Hirschmann et al., 2003). Among them, KLB-1, RE46, wet basalt and Tonalite 101 are directly benchmarked against pseudosections produced with THERMOCALC (Figs. 3 and 4).

The pseudosections for KLB-1 peridotite (Fig. 3A,B), RE46 Icelandic basalt (Fig. 3C,D), Tonalite 101 (Fig. 4A,B) and Wet basalt (Fig. 4C,D) were computed with both THERMOCALC and MAGEMin. The pseudosections for KLB-1 and RE46 were computed in the KNCFMASTOCr system from 0 to 5 GPa and from 800 to 2000 °C, and from 0 to 1.2 GPa and from 1000 to 1400 °C, respectively. The pseudosections for T101 and Wet Basalt were computed in the KNCFMASHTOCr system from 0 to 0.25 GPa and from 650 to 925 °C, and from 0 to 2.4 GPa and from 800 to 1400 °C, respectively. For MAGEMin, the total number of minimized points per pseudosection varies from 80,000 to 100,000. The resulting 4 pseudosections produced with MAGEMin show nearly identical results to the one produced with THERMOCALC (Figs 3 and 4).

The pseudosections for N-MOR basalt and MIX1G pyroxenite were computed only with MAGEMin in the KNCFMASTOCr chemical system (Fig. 4A,B) from 0 to 1.2 GPa and from 500 to 1400 °C, and from 0 to 2.0 GPa and from 600 to 1600 °C, respectively.

A.4.2 Seismic velocities

Seismic velocities (see Fig. A.4.5) are computed following the approach described in Connolly and Kerrick (2002) such as:

$$v_p = \sqrt{\frac{K_b + \frac{4K_s}{3}}{\rho}}, \tag{A.39}$$

and

$$v_s = \sqrt{\frac{K_s}{\rho}}, \tag{A.40}$$

where v_p is the P-wave velocity, v_s the S-wave velocity, ρ the density, K_b the adiabatic bulk modulus and K_s is the elastic shear modulus. The adiabatic bulk modulus is

TABLE A.4.1: Bulk-rock compositions (mol%) used to produce the igneous phase diagrams. Note that for readability purpose the Tonalite 101 bulk-rock composition is not displayed normalized to 100.

Name	SiO2	Al2O3	CaO	MgO	FeO	K2O	Na2O	TiO2	O	Cr2O3	H2O
Demo	70.69	16.63	4.56	-	-	4.45	3.67	-	-	-	-
KLB1 peridotite	38.49	1.776	2.824	50.57	5.89	0.01	0.25	0.10	0.096	0.109	-
RE46 basalt	50.72	9.16	15.21	16.25	7.06	0.01	1.47	0.39	0.35	0.01	-
Tonalite 101	66.01	11.98	7.06	4.16	5.30	1.57	4.12	0.66	0.97	0.01	50.0
Water-bearing basalt	50.08	8.69	11.67	12.14	7.78	0.22	2.49	1.00	0.47	0.01	5.44
MIX1G pyroxenite	45.25	8.89	12.22	24.68	6.45	0.03	1.39	0.67	0.11	0.012	-
N-MORB basalt	53.21	9.41	12.2 1	12.21	8.65	0.09	2.90	1.21	0.69	0.02	-

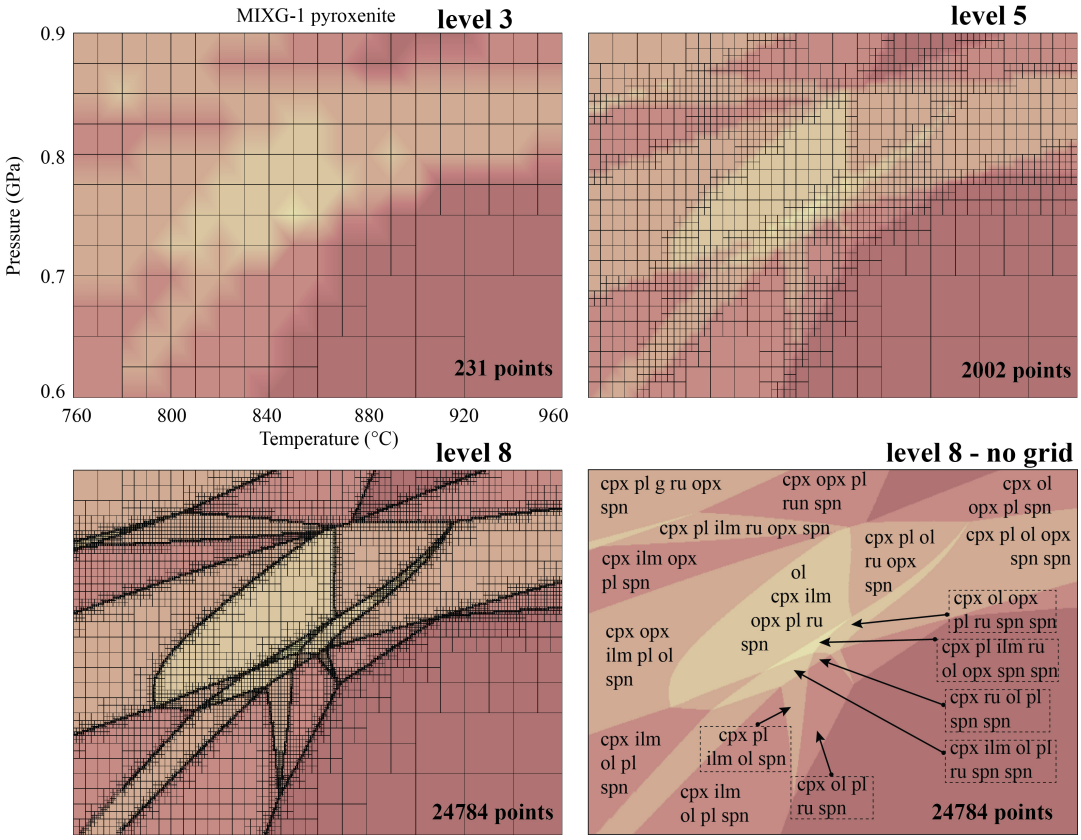

FIGURE A.4.1: Illustration of the adaptive mesh refinement strategy used for pseudosection computation. Adaptive mesh refinement is illustrated for a sub-section of MIX1G phase diagram displaying complex phase relations (see Fig. 5B). In total 8 levels of refinements are processed with an initial pressure-temperature step of 0.1 GPa and 40 °C. A grid cell is refined by splitting in 4 smaller cells, when at least one of the four corners exhibits a different mineral assemblage. This allows us to progressively increase the resolution along reaction lines and properly resolve them as the levels of refinement increase (see level 8). Moreover, this strategy allows us to significantly reduce the total number of minimization compared to a uniform refinement reaching the same resolution, which would have required 245,760 points for this example.

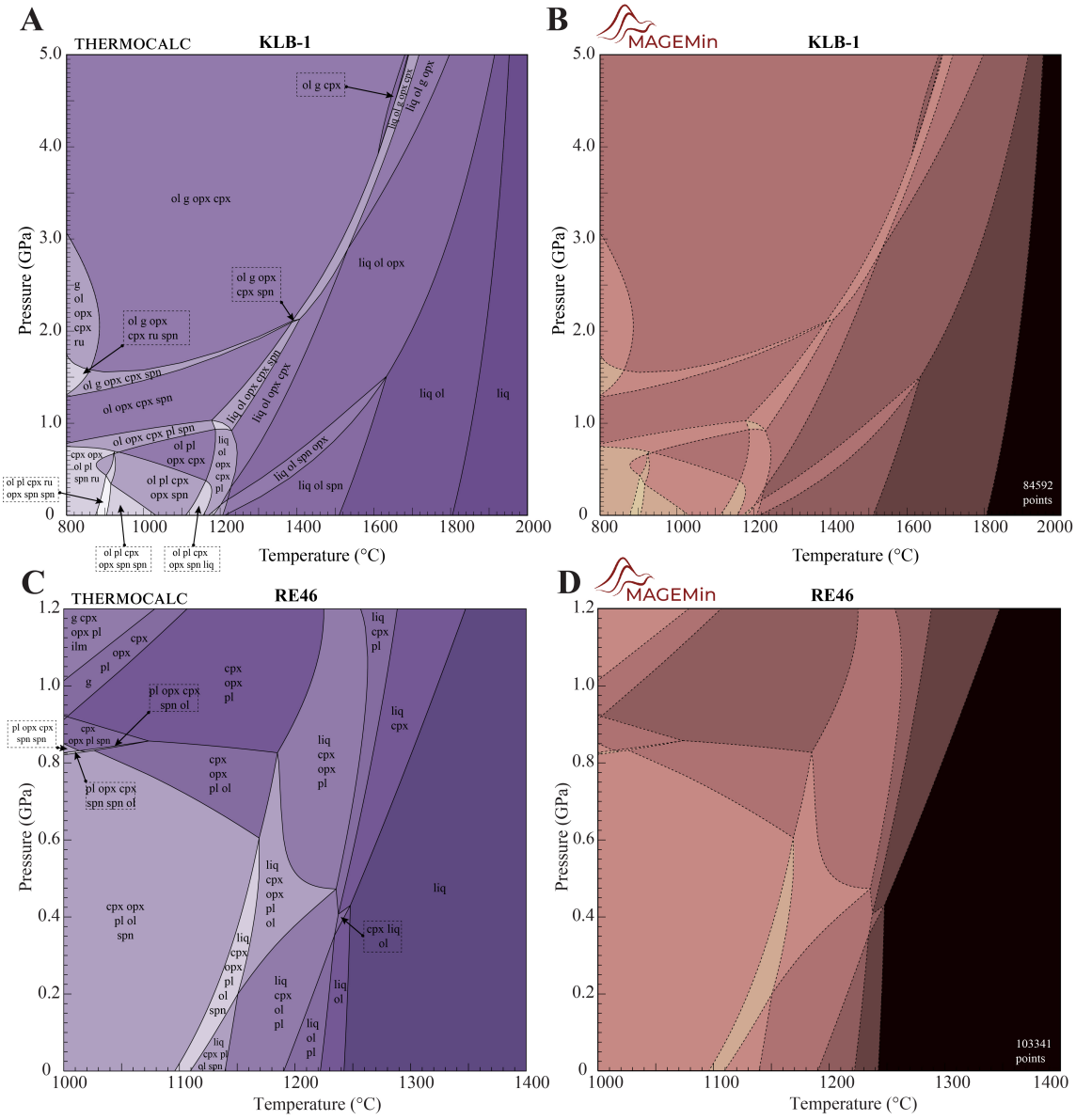

FIGURE A.4.2: Comparison of dry pseudosections produced by THERMOCALC and MAGEMin. A, B, KLB-1 peridotite. C,D, RE46 Islandic basalt. For comparison, THERMOCALC reaction lines are shown as dashed lines in the MAGEMin pseudosection. Shading represents the variance of the system.

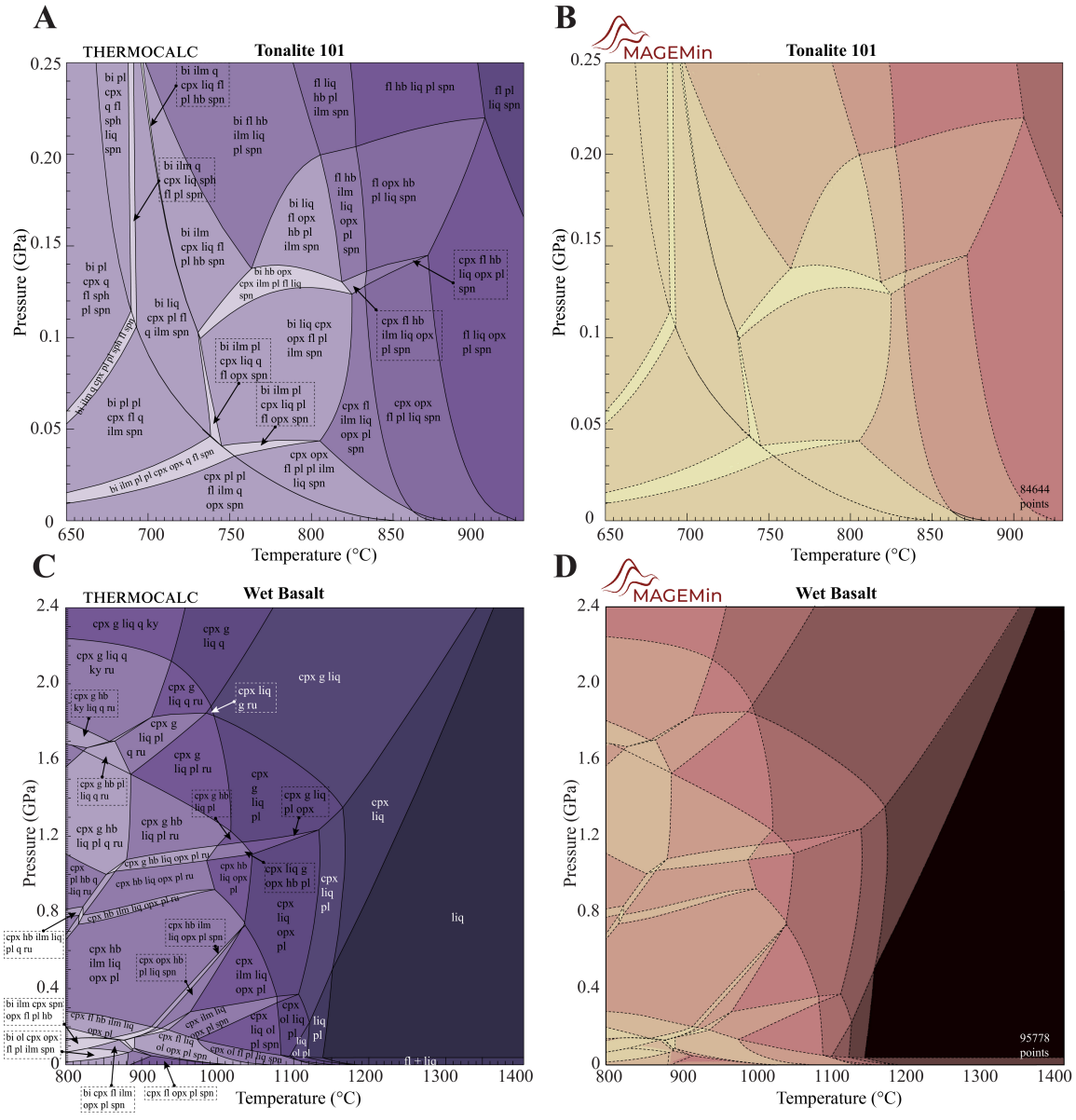

FIGURE A.4.3: Comparison of wet pseudosections produced by THERMOCALC and MAGEMin. A, B, T101 tonalite. C,D, Wet basalt.

calculated from the thermodynamic data as

$$K_b = -\frac{\partial G_{sys}}{\partial P}\left[\frac{\partial^2 G_{sys}}{\partial P^2} + \left(\frac{\partial}{\partial P}\frac{\partial G_{sys}}{\partial T}\right)^2 \Big/ \frac{\partial^2 G_{sys}}{\partial T^2}\right]^{-1}. \tag{A.41}$$

Shear modulii cannot be computed from thermodynamic data, and are therefore calculated using an empirical relation (Connolly and Kerrick, 2002):

$$K_s = K_s^0 + T\frac{\partial K_s}{\partial T} + P\frac{\partial K_s}{\partial P}. \tag{A.42}$$

The shear modulii of the appropriate phases used in this study are taken from the database provided in Perple_X (Connolly, 2005). The database is a collection of shear modulii data mainly from Helffrich (1996), and from Karki et al. (2001), Sinogeikin et al. (2000), Bailey and Holloway (2000) and Bass et al. (1995). The bulk-rock seismic velocities are calculated without anelasticity correction, using a Voight–Reuss–Hill averaging of the velocities of the constituent phases, weighted by volume fraction (Connolly and Kerrick, 2002).

A.5 Discussion

A.5.1 Minimization approach

Here, we present a new Gibbs energy minimization approach applied to multiphase multicomponent systems. While some of the key ideas of our approach are based on the method of Partitioning Gibbs Energy (PGE) (e.g., Piro et al., 2013a; Kruskopf and Visuri, 2017) we extended it to account for modelling of mineral solid solutions involving mixing-on-sites (Eq. A.17 to A.21). In Piro et al. (2013a) the fraction of the end-members are updated using Eq. A.15, whereas in our formulation the PGE stage is used to decrease the residual between $x_{i(\lambda)}$ and $p_{i(\lambda)}$. Essentially, the expression $\exp\left(-\frac{\Delta\mu_{i(\lambda)}}{RT}\right)$ of Eq. A.21 forces the system to progressively satisfy the Gibbs Duhem rule by penalizing the fraction of end-members (hence, the mass constraint) computed during local minimization. However, to avoid divergence, the PGE stage requires a good initial guess, proper set of under-relaxing factors and more critically, a highly consistent local minimization step. Although NLopt (Johnson, 2021) implements several gradient-based minimizers with inequality constraints (SLSQP, MMA, CCSAQ), we find that the CCSAQ algorithm (Svanberg, 2002) yields by far the best consistency and precision compared to SLSQP and linear MMA.

A.5.2 Consistency

The application of MAGEMin to the igneous thermodynamic dataset of Holland et al. (2018) shows very good agreement with pseudosections produced with THERMOCALC (Figs 3 and 4). However, minor differences can be observed in some regions. For instance the tonalite 101 pseudosection produced with MAGEMin (Fig. 4B) has an

irregular reaction line at ca. 750 °C and 0.1 GPa (Fig. 3B). This is caused by oscillations when getting close to convergence, where a relaxed solution tolerance was accepted (tol $\leq 10^{-4}$ instead of the default value of 10^{-5}). Similar irregular reactions lines related to slightly relaxed tolerances can be observed in N-MOR basalt at ca. 750 °C and 0.88 GPa (Fig. 5A) and in MIX1G pyroxenite at ca. 1250 °C and 1.4 GPa (Fig. 5B).

A.5.3 Computational efficiency

Pseudosections presented in this work have been run in parallel on 6 logical processors on an Intel(R) Core(TM) i5-11400H. Single point calculation time has been averaged for each pseudosection which yielded 96 ms for KLB-1, 122 ms for RE46, 186 ms for Tonalite 101 and 162 ms for Wet Basalt. The large increase of calculation time for water-bearing compositions (Tonalite 101 and Wet Basalt) stems from having a larger number of discrete points during levelling (+ 40 ms) and a larger number of global iterations to reach convergence (+40 to 60 iterations on average).

In order to roughly compare our results with Perple_X (Connolly, 2005), we recomputed the KLB-1 pseudosection at similar resolution (±9000 grid points, Fig. 6). Although Perple_X did not include the last version of the dataset "hp634ver.dat" at the time we generated the diagram (Fig. 6A), we obtain a similar pseudosection nearly 20 times faster (Fig. 6B). Note that with default option the pseudosection was computed with Perple_X in 36 minutes, but the overall quality of the grid was quite degraded and we therefore choose to increase the grid resolution (exploratory and autorefine set to 60 and 200, respectively). In terms of single core performance, we still find that MAGEMin is nearly 3 times faster and yields cleaner diagrams with less visible artefacts (Fig. 6). Moreover, since the current version of Perple_X is not parallelized, the computational differences are more significant in practice. In the other comparable G-minimization software, Theriak and pMELTS, the Holland et al. (2018) thermodynamic dataset is not or cannot be implemented.

A.5.4 Coupling with geodynamic codes

In order to facilitate coupling with geodynamic codes we provide a Julia wrapper to MAGEMin. The Julia wrapper (called MAGEMin_C) allows the user to directly call the C functions of MAGEMin without writing data to disk first (which is slow). The results of the minimization are saved into a structure that is also accessed through the Julia interface. Here we provide a simple example.

Assuming Julia is installed, to install MAGEMin_C, first open a Julia terminal and type:

```
julia> ]                                  # opens the package manager
pkg> add MAGEMin_C                        # MAGEMin_C
```

To compute a phase equilibrium, first leave the package manager (using backspace) and enter the following commands:

```
julia> using MAGEMin_C                    # load MAGEMin_C package
julia> gv, DB      = init_MAGEMin();      # initializes MAGEMin
julia> P_kbar,T_C  = 8.0, 800.0;
julia> bulk_rock   = get_bulk_rock(gv, 0);# bulk-rock composition for test 0 (KLB-1 peridotite)
julia> gv.verbose  = -1;                  # switch off run-time verbose
julia> out         = point_wise_minimization(P_kbar,T_C, bulk_rock, gv, DB);
julia> print_info(out);                   # full display of the minimized point
```

A complete guide of the Julia interface is provided on the MAGEMin webpage.

A.5.5 Current limitations and known problems

Currently, only the thermodynamic dataset for igneous systems (Holland et al., 2018) has been implemented in MAGEMin. Yet, our approach is generally applicable and should thus in principle work with any thermodynamic dataset. In order to account for other petrological systems, additional datasets could be implemented for example relevant to metapelitic (White et al., 2014) or metabasitic systems (Green et al., 2016). We expect the performance of those cases to be at least as good, as the equations of state for solution phases are somewhat simpler.

To be successful, our implementation of the Partitioning Gibbs Energy method heavily relies on having a good initial guesses, here provided by the levelling stage. At present, our approach tends to have difficulties to converge in some cases, mainly at sub-solidus conditions and for water-bearing bulk-rock compositions (< 650 °C). When divergence is observed, it usually occurs very fast and several methods are being tested to remedy that issue. One potential cause of divergence can be attributed to the current discretization approach employed during the levelling stage. Indeed, for complex solution phases, such as amphibole, the large discretization step used to keep the number of pseudocompounds relatively low (< 6000) can be a source of uneven sampling of the solution phase space, which may lead to minimization failure (likely because the minimization gets stuck in an unfeasible local minimum). A possible workaround would be to add the complete list of end-members bounding the space of valid site-occupancies, following the procedure described in Myhill and Connolly (2021). A complementary option could be to pre-compute over a given P-T range the local minima of each solution phase and add them to the pseudocompound list.

Finally, magemin does not presently account for bulk-rock compositions that are in a different system from the set of solution phase models (equations of state) provided in Holland et al. (2018). While TiO_2, Fe_2O_3, Cr_2O_3 and H_2O can somewhat be set to 0.0, other system components cannot be ignored without reformulating some of solution phase model. However, being able to obtain stable phase equilibria in restricted chemical system is crucial to model magmatic differentiation. As a consequence we are actively working on producing a generalized set of solution phase models accounting for reduced chemical systems.

A.6 Conclusions

We present a new parallel Gibbs energy minimizer that allows us to compute stable equilibria in complex multicomponent multiphase systems. We successfully extended the Partitioning Gibbs Energy approach to Gibbs energy functions that model mixing-on-sites, and applied it to the most recent thermodynamic igneous dataset. Pseudosection computation shows very consistent results with THERMOCALC and improved performance with respect to other software such as the current Perple_X version. The parallel design of MAGEMin makes it highly scalable on multicore machines. While in this contribution we computed pseudosections using a MATLAB-based interface, MAGEMin has been developed with the objective to provide the community with a minimization package easily callable from any geodynamic codes. Such tool can also potentially provide a robust framework for thermodynamic database inversions.

A.7 Software availability

A complete guide on how to download, install and run MAGEMin is given in the git repository https://github.com/ComputationalThermodynamics/MAGEMin.git. The version of the code is also made available on Zenodo, doi:10.5281/zenodo.6347567

A.8 Acknowledgement

This study was funded by the European Research Council through the MAGMA project, ERC Consolidator Grant #771143. We greatly thank Roger Powell for help with producing the THERMOCALC pseudosections presented in this study. We thank Markus Bachmayr for help with consistent discretization of the G-surfaces of solution phases and James Connolly for comments on the manuscript. We also thank the anonymous reviewer for suggestions and Robert Myhill for his review which greatly helped to clarify the manuscript and for valuable github contributions to MAGEMin.

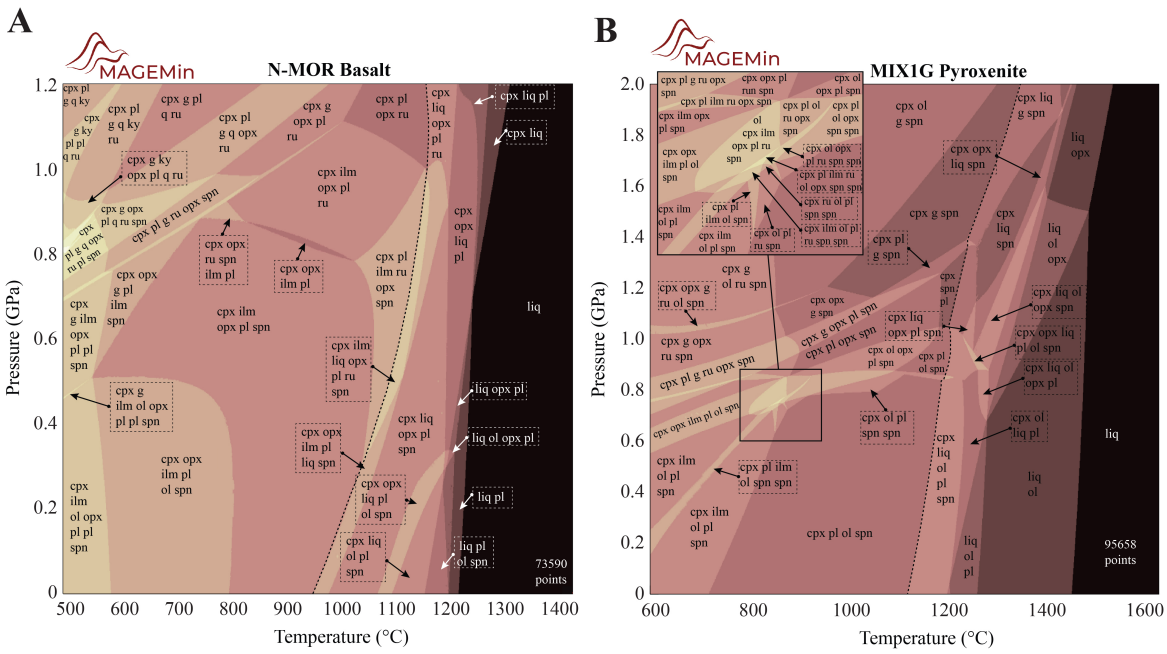

FIGURE A.4.4: Pseudosections for N-MOR basalt and MIX1G pyroxenite.

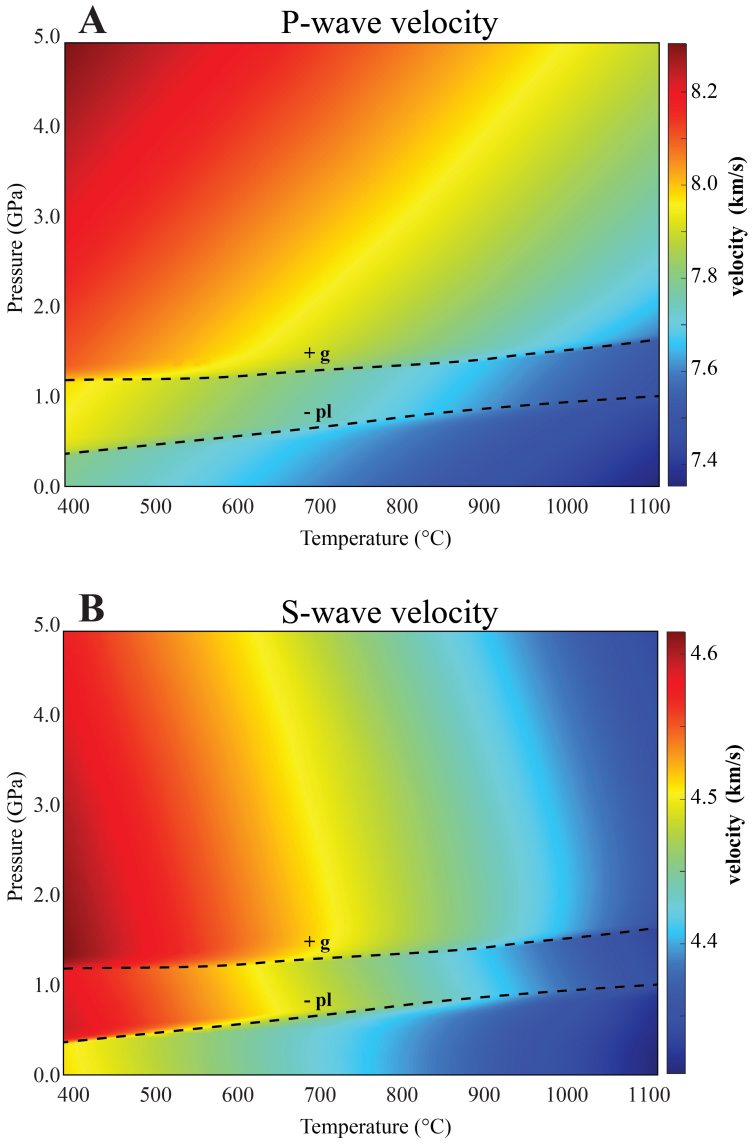

FIGURE A.4.5: Example of seismic velocity computation for KLB-1 peridotite. A, P-wave velocity. B, S-wave velocity.

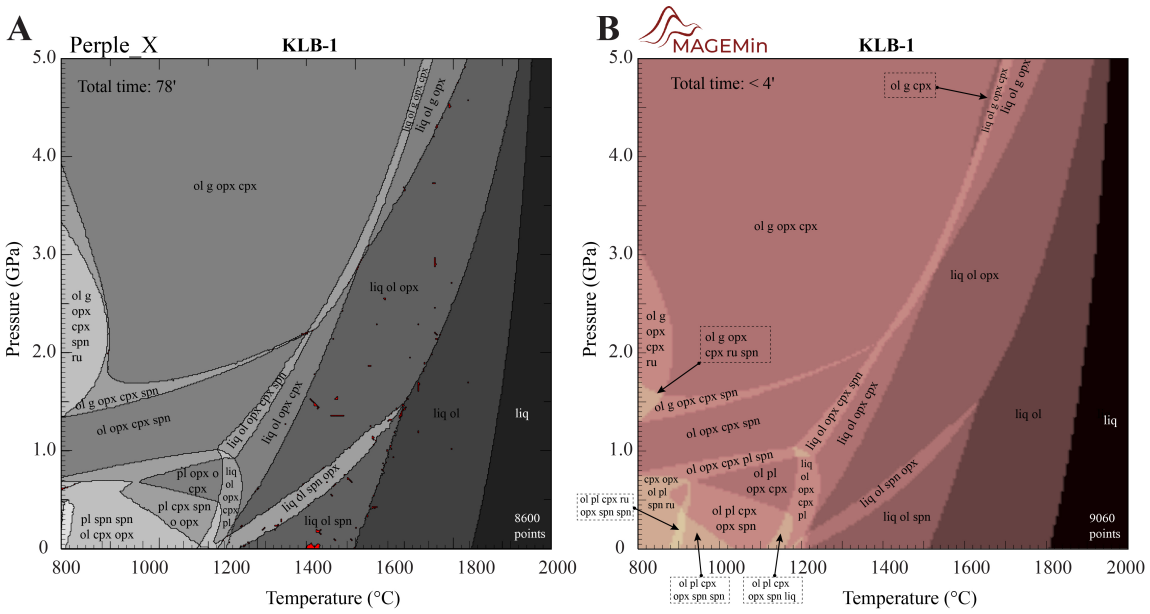

FIGURE A.5.1: Comparison of KLB-1 pseudosections produced by Perple_X and MAGEMin. For the Perple_X pseudosection, we used version 6.9.1, the database file hp633ver.dat and the solution models Sp(HGP), Gt(HGP), Cpx(HGP), melt(HGP), O(HGP), Opx(HGP), feldspar and excluding "enL" and "fo8L". In order to have a better resolution of the reaction lines, we increased the exploratory and autorefine parameters to 60 and 200, respectively. For MAGEMin, we employed four levels of grid refinement in order to reach a similar number of minimization points as displayed in the Perple_X log.

Supplementary

A.A Equations of state in the example thermodynamic dataset

Here we summarize how the equations of state are formulated in our example thermodynamic dataset, that of Holland et al. (2018). We detail the information passed as input to both THERMOCALC and MAGEMin, using the Holland et al. (2018) equation of state for the olivine solid solution as an example. In Appendix B, we show how MAGEMin sets up the minimization step for the model olivine solid solution.

In Holland et al. (2018), and related thermodynamic datasets such as White et al. (2014) and Green et al. (2016), the equation of state of a mineral is assembled from up to four components (for a pure phase, consisting of a single end-member, only aspects 2 or 3 apply):

1. A choice about what composition space the model solution phase should encompass, which discrete mixing sites should be distinguished, and which ions should be considered to mix on each site; e.g. Table A.A.1. These choices determine which end-members will be required.

2. The $G(P,T)$ relations for those model end-members that are found in the appropriate version of the Holland and Powell (2011) internally-consistent dataset of thermodynamic properties of end-members (IDE).

3. $G(P,T)$ relations for those model end-members that are not in the IDE. For non-IDE end-member i, this is constructed from the $G(P,T)$ curves of a subset of Λ IDE end-members, as $G_i(P,T) = \Sigma_{\lambda=1}^{\Lambda} \nu_\lambda G_\lambda(P,T) + a + bT + cP$, where a, b and c are constants, and the net composition of the combination of end-members Λ yields the composition of i. The IDE end-members Λ do not necessarily appear anywhere else in the thermodynamic dataset.

4. Activity–composition (a–x) relations, which describe the thermodynamic contributions of mixing among the end-members. In general these follow the asymmetric formalism of Holland and Powell (2003). In the asymmetric formalism, the configurational entropy is formulated in terms of mixing on sites, potentially with a non-unity scaling factor applied to each site as described below. The non-ideal mixing contribution from each end-member is defined in terms of a single interaction energy (Margules parameter, W) between each pair of end-members (equation A.62), which may be asymmetric, and may be linearly dependent on P

and/or T (thereby potentially contributing excess volume and/or entropy terms in addition to excess enthalpy).

In the Holland et al. (2018) model for the olivine solution, the end-members and mixing site occupancies are as shown in Table A.A.1. The end-members forsterite, fayalite and monticellite are taken directly from the IDE. End-member cfm represents full ordering of Mg and Fe on the M1 and M2 sites; it is not in the IDE, but the $G_{\rm cfm}(P,T)$ curve is formed from

$$G_{\rm cfm}(P,T) = 1/2(G_{\rm fo}(P,T) + G_{\rm fa}(P,T)) + \Delta G^{od}_{\rm cfm} \tag{A.43}$$

where $\Delta G^{od}_{\rm cfm}$ is the Gibbs energy of ordering in the cfm composition, and has the form $a + bT + cP$.

Compositional and order variability within the solid solution are defined in terms of site fractions:

$$\begin{aligned} x &= (x\text{FeM1} + x\text{FeM2})/(x\text{FeM1} + x\text{FeM2} + x\text{MgM1} + x\text{MgM2}) && \text{(A.44)}\\ c &= x\text{CaM2} && \text{(A.45)}\\ Q &= x - x\text{FeM1}/(x\text{FeM1} + x\text{MgM1}) && \text{(A.46)} \end{aligned}$$

where, for example, xFeM1 is the fraction of Fe on the M1 site. Compositional and order variables are subject to bounds, which for x, c and Q, as in most cases, are [0.0 1.0]. The variables are chosen so as to ensure that the fraction of mixing ions on each site are normalised to a constant total, and, if relevant, that charge balance is obeyed within the mineral.

Written in these variables, the site fractions are expressed as

$$x\text{MgM1} = 1 + Q - x, \tag{A.47}$$

$$x\text{FeM1} = -Q + x, \tag{A.48}$$

$$x\text{MgM2} = 1 - c - Q - x + cx, \tag{A.49}$$

$$x\text{FeM2} = Q + x + (-c)x, \tag{A.50}$$

$$x\text{CaM2} = c, \tag{A.51}$$

The site fraction expressions are required to express the ideal activity, and hence the configurational entropy, of the model end-members in the solution. For some minerals, though not in olivine, the entropic contribution of a particular site is reduced by a scaling factor (see e.g. Holland et al., 2021), to simulate the effects of short-range order in the crystal structure. Thus, the ideal activity of end-member i can be expressed as

$$a^{id}_{i(\lambda)} = c_i \prod_s (X^s_{e_{s,i}})^{\nu_s f_s} \tag{A.52}$$

where $X^s_{e_{s,i}}$ is the site fraction of the element $e_{s,i}$ that appears on site s, ν_s is the number of atoms mixing on s, c_i the normalisation constant to give $a^{id}_{i(\lambda)} = 1$ for pure i, and f the scaling factor for the site. For olivine ($f = 1$ for all sites), the ideal activities are

$$a^{id}_{\text{mont}} = x\text{MgM1} \cdot x\text{CaM2}, \tag{A.53}$$

$$a^{id}_{\text{fa}} = x\text{FeM1} \cdot x\text{FeM2}, \tag{A.54}$$

$$a^{id}_{\text{fo}} = x\text{MgM1} \cdot x\text{MgM2}, \tag{A.55}$$

$$a^{id}_{\text{cfm}} = x\text{MgM1} \cdot x\text{FeM2}. \tag{A.56}$$

The proportions of the end-members present at a given composition and state of order can be expressed as:

$$p_{\text{mont}} = c, \tag{A.57}$$

$$p_{\text{fa}} = -Q + x, \tag{A.58}$$

$$p_{\text{fo}} = 1 - c - Q - x + cx, \tag{A.59}$$

$$p_{\text{cfm}} = 2Q + (-c)x. \tag{A.60}$$

The equation of state is conveniently assembled in terms of the $\mu_i(P, T, \mathbf{x}, \mathbf{Q})$, where μ_i is the chemical potential of end-member i, and $\mu_i = \frac{\partial G_i}{\partial p_i}$. μ_i can be written as

$$\mu_i = \mu^0_i + RT \log(a^{id}_i) + \mu^{ex}_i, \tag{A.61}$$

where μ^0_i is the chemical potential of pure i, with $\mu^0_i(P, T) = G_i(P, T)$, as described above. In the asymmetric formalism, μ^{ex}_i is given by

$$\mu^{ex}_i = -\sum_{m=1}^{N_{ol}-1} \sum_{n>m}^{N_{ol}} (\phi'_m - \phi_m)(\phi'_n - \phi_n) W_{m,n} \left(\frac{2v_i}{v_m + v_n} \right). \tag{A.62}$$

Here, ϕ_i is the proportion of end-member i weighted by the asymmetry parameters, as $\phi_i = (p_i v_i)/(\sum_{m=1}^{N_{ol}} p_m v_m)$, with v_i the asymmetry parameter for end-member i. ϕ'_m is the value of ϕ_m in end-member i, such that $\phi'_m = 1$ where $m = i$ and $\phi'_m = 0$ where $m \neq i$. $W_{m,n}$ is the interaction energy between end-members m and n in the solution. The values of model parameters in the olivine solid solution are given in Table A.A.2.

A.B Implementation in MAGEMin

MAGEMin uses the input outlined in Appendix A to assemble the Gibbs energy of olivine at pressure P and temperature T:

$$G_{ol}(\mathbf{x}, \mathbf{Q})|_{P,T} = \sum_{i=1}^{N_{ol}} \left(\mu_{i(ol)}(\mathbf{x}, \mathbf{Q}) \cdot p_{i(ol)}(\mathbf{x}, \mathbf{Q}) \right)|_{P,T}, \tag{A.63}$$

TABLE A.A.1: End-members and mixing site occupancies of olivine in the Holland et al. (2018) thermodynamic dataset.

End-member	Abbreviation	Formula	Mixing sites				
			M1		M2		
			Mg	Fe	Mg	Fe	Ca
forsterite	fo	Mg_2SiO_4	1	0	1	0	0
fayalite	fa	Fe_2SiO_4	0	1	0	1	0
ordered intermediate	cfm	$MgFeSiO_4$	1	0	0	1	0
monticellite	mont	$CaMgSiO_4$	1	0	0	0	1

TABLE A.A.2: Values of parameters in the model olivine solid solution of Holland et al. (2018)

$W_{m,n}$ binary	value
W(mont,fa)	24 kJ
W(mont,fo)	38 kJ
W(mont,cfm)	24 kJ
W(fa,fo)	9 kJ
W(fa,cfm)	4.5 kJ
W(fo,cfm)	4.5 kJ
v_{fo}	1
v_{fa}	1
v_{cfm}	1
v_{mont}	1
$\Delta G^{od,a}_{\mathrm{cfm}}$	0 kJ
$\Delta G^{od,b}_{\mathrm{cfm}}$	0 kJ/K
$\Delta G^{od,c}_{\mathrm{cfm}}$	0 kJ/kbar

where $\mu_{i(ol)}$ is obtained as in equation A.62. Equation A.63 constitutes the objective function for the minimization step. The gradient of the objective function is the derivative of the Gibbs from energy of olivine with respect to the compositional variables:

$$\frac{\partial G_{ol}}{\partial x_k} = \sum_{i=1}^{N_{ol}} \mu_{i(ol)} \frac{\partial p_{i(ol)}}{\partial x_k}, \tag{A.64}$$

where $\frac{\partial p_{i(ol)}}{\partial x_k}$ is given in Table A.B.1. During the minimization, the value of all site fractions is required to be ≥ 0 via a set of non-linear inequality constraints (derived from Eqs. A.47 to A.51) that is passed to the local minimizer. The gradients of the site-fractions with respect to the compositional and order variables are given in Table A.B.2.

The above expressions are passed to NLopt (Johnson, 2021) together with an initial guess for the compositional variables. Subsequently, the objective function is minimized using the CCSAQ algorithm (Svanberg, 2002).

TABLE A.B.1: Partial derivatives of end-member proportions as function of compositional variables

	$\frac{\partial p_i}{\partial x}$	$\frac{\partial p_i}{\partial c}$	$\frac{\partial p_i}{\partial Q}$
$\frac{\partial p_{fo}}{\partial x_k}$	c-1	x-1	-1
$\frac{\partial p_{fa}}{\partial x_k}$	1	0	-1
$\frac{\partial p_{cfm}}{\partial x_k}$	-c	-x	2
$\frac{\partial p_{mont}}{\partial x_k}$	0	1	0

TABLE A.B.2: Partial derivatives of site-fractions as function of compositional variables

	$\frac{\partial sf_i}{\partial x}$	$\frac{\partial sf_i}{\partial c}$	$\frac{\partial sf_i}{\partial Q}$
$\frac{\partial xMgM1}{\partial x_k}$	-1	0	1
$\frac{\partial xFeM1}{\partial x_k}$	1	0	-1
$\frac{\partial xMgM2}{\partial x_k}$	c-1	x-1	-1
$\frac{\partial xFeM2}{\partial x_k}$	$1-c$	x	1
$\frac{\partial xCaM2}{\partial x_k}$	0	1	0

Acknowledgements

This study was funded by the European Research Council through the MAGMA project, ERC Consolidator Grant #771143.

Eidesstattliche Erklärung

Ich versichere hiermit gemäß §10 Abs. 3d der Promotionsordnung des Fachbereichs 09 (Chemie, Pharmazie und Geowissenschaften) der Johannes Gutenberg-Universität Mainz vom 24.07.2007, die als Dissertation vorgelegte Arbeit selbständig und nur unter Verwendung der in der Arbeit angegebenen Hilfsmittel verfasst zu haben. Ich habe oder hatte die hier als Dissertation vorgelegte Arbeit nicht als Prüfungsarbeit für eine staatliche oder andere wissenschaftliche Prüfung eingereicht. Ich hatte weder die jetzt als Dissertation vorgelegte Arbeit noch Teile davon bei einer anderen Fakultät bzw. einem anderen Fachbereich als Dissertation eingereicht.

Nicolas Berlie
Mainz, 2023

Bibliography

Acocella, V., R. Funiciello, E. Marotta, G. Orsi, and S. de Vita (2004). "The role of extensional structures on experimental calderas and resurgence". In: *Journal of Volcanology and Geothermal Research* 129.1-3, pp. 199–217. ISSN: 03770273. DOI: 10.1016/S0377-0273(03)00240-3.

Acocella, V. and M. Neri (2009). "Dike propagation in volcanic edifices: Overview and possible developments". In: *Tectonophysics* 471.1-2, pp. 67–77. ISSN: 00401951. DOI: 10.1016/j.tecto.2008.10.002. URL: http://dx.doi.org/10.1016/j.tecto.2008.10.002.

Anderson, Ernest Masson (1951). *The dynamics of faulting and dyke formation with applications to Britain*. 2nd ed., rev. Oliver. URL: https://cir.nii.ac.jp/crid/1130282272687106688.

Andrić-Tomašević, Nevena, Alexander Koptev, Giridas Maiti, Taras Gerya, and Todd A. Ehlers (2023). "Slab tearing in non-collisional settings: Insights from thermo-mechanical modelling of oblique subduction". In: *Earth and Planetary Science Letters* 610. ISSN: 0012821X. DOI: 10.1016/j.epsl.2023.118097.

Annen, Catherine, Michel Pichavant, Olivier Bachmann, and Alain Burgisser (2008). "Conditions for the growth of a long-lived shallow crustal magma chamber below Mount Pelee volcano (Martinique, Lesser Antilles Arc)". In: *Journal of Geophysical Research: Solid Earth* 113.7, pp. 1–16. ISSN: 21699356. DOI: 10.1029/2007JB005049.

Armijo, Larry (1966). "Minimization of functions having Lipschitz continuous first partial derivatives." In: *Pacific Journal of Mathematics* 16.1, pp. 1 –3.

Arthur, J. R.F., T. Dunstan, Q. A.J.L. Al-Ani, and A. Assadi (1978). "Plastic Deformation and Failure in Granular Media". In: *Geotechnique* 28.1, pp. 125–128. ISSN: 17517656. DOI: 10.1680/geot.1978.28.1.125.

Asimow, Paul D. and Mark S. Ghiorso (1998). "Algorithmic modifications extending MELTS to calculate subsolidus phase relations". In: *American Mineralogist* 83.9-10, pp. 1127–1132. DOI: doi:10.2138/am-1998-9-1022.

Bachmann, Olivier and George W. Bergantz (Aug. 2004). "On the origin of crystal-poor rhyolites: Extracted from batholithic crystal mushes". In: *Journal of Petrology* 45 (8), pp. 1565–1582. ISSN: 00223530. DOI: 10.1093/petrology/egh019.

Bachmann, Olivier and Christian Huber (2016). "Silicic magma reservoirs in the Earth's crust". In: *American Mineralogist* 101 (11), pp. 2377–2404. ISSN: 19453027. DOI: 10.2138/am-2016-5675.

Badia, Santiago and Francesc Verdugo (2020). "Gridap: An extensible Finite Element toolbox in Julia". In: *Journal of Open Source Software* 5.52, p. 2520. DOI: 10.21105/joss.02520. URL: https://doi.org/10.21105/joss.02520.

Bailey, Edward and John R Holloway (2000). "Experimental determination of elastic properties of talc to 800 C, 0.5 GPa; calculations of the effect on hydrated peridotite, and implications for cold subduction zones". In: *Earth and Planetary Science Letters* 183.3-4, pp. 487–498.

Bass, Jay D et al. (1995). "Elasticity of minerals, glasses, and melts". In: *Mineral physics and crystallography: A handbook of physical constants* 2, pp. 45–63.

Baumann, Tobias S, Boris J P Kaus, and Anton A Popov (2018). "insights from 3D numerical models". In: pp. 597–609.

Berman, Robert G (1991). "Thermobarometry using multi-equilibrium calculations; a new technique, with petrological applications". In: *The Canadian Mineralogist* 29.4, pp. 833–855.

Bezanson, Jeff, Alan Edelman, Stefan Karpinski, and Viral B Shah (2017). "Julia: A fresh approach to numerical computing". In: *SIAM review* 59.1, pp. 65–98.

Biot, Maurice A and Maurice A Blot (1941). "General theory of three dimensional consolidation general theory of three-dimensional consolidation". In: *J. Appl. Phys. Additional information on J. Appl. Phys. Journal Homepage* 12.155, pp. 155–164.

Borst, René and Thibault Duretz (2020). "On viscoplastic regularisation of strain-softening rocks and soils". In: *International Journal for Numerical and Analytical Methods in Geomechanics* I.August 2019, nag.3046. ISSN: 0363-9061. DOI: 10.1002/nag.3046. URL: https://onlinelibrary.wiley.com/doi/abs/10.1002/nag.3046.

Burgos-Solórzano, Gabriela I., Joan F. Brennecke, and Mark A. Stadtherr (2004). "Validated computing approach for high-pressure chemical and multiphase equilibrium". In: *Fluid Phase Equilibria* 219.2, pp. 245–255. ISSN: 0378-3812. DOI: https://doi.org/10.1016/j.fluid.2003.12.013.

Caggiano, Antonio, Guillermo Etse, and Enzo Martinelli (2012). "Zero-thickness interface model formulation for failure behavior of fiber-reinforced cementitious composites". In: *Computers and Structures* 98-99, pp. 23–32. ISSN: 00457949. DOI: 10.1016/j.compstruc.2012.01.013. URL: http://dx.doi.org/10.1016/j.compstruc.2012.01.013.

Candioti, Lorenzo G., Thibault Duretz, and Stefan M. Schmalholz (2022). "Horizontal Force Required for Subduction Initiation at Passive Margins With Constraints From Slab Detachment". In: *Frontiers in Earth Science* 10.May, pp. 1–19. ISSN: 22966463. DOI: 10.3389/feart.2022.785418.

Capitani, Christian de and Konstantin Petrakakis (2010). "The computation of equilibrium assemblage diagrams with Theriak/Domino software". In: *American Mineralogist* 95.7, pp. 1006–1016. DOI: doi:10.2138/am.2010.3354.

Carslaw, H. S. and J. C. Jaeger (1959). *Conduction of Heat in Solids*. 2nd. Oxford: Clarendon Press. ISBN: 0198533039.

Cashman, Katharine V., R. Stephen J. Sparks, and Jonathan D. Blundy (2017). "Vertically extensive and unstable magmatic systems: A unified view of igneous processes". In: *Science* 355.6331. ISSN: 10959203. DOI: 10.1126/science.aag3055.

Castro, Jonathan M. and Yves Feisel (2022). "Eruption of ultralow-viscosity basanite magma at Cumbre Vieja, La Palma, Canary Islands". In: *Nature Communications* 13.1. ISSN: 20411723. DOI: 10.1038/s41467-022-30905-4.

Çetin, Gürcan and Ali Keçebaş (2021). "Optimization of thermodynamic performance with simulated annealing algorithm: A geothermal power plant". In: *Renewable Energy* 172, pp. 968–982. ISSN: 0960-1481. DOI: https://doi.org/10.1016/j.renene.2021.03.101.

Civico, Riccardo, Tullio Ricci, Piergiorgio Scarlato, Jacopo Taddeucci, Daniele Andronico, Elisabetta Del Bello, Luca D'Auria, Pedro A. Hernández, and Nemesio M. Pérez (2022). "High-resolution Digital Surface Model of the 2021 eruption deposit of Cumbre Vieja volcano, La Palma, Spain". In: *Scientific Data* 9.1, pp. 1–7. ISSN: 20524463. DOI: 10.1038/s41597-022-01551-8.

Coleman, Drew S., Walt Gray, and Allen F. Glazner (2004). "Rethinking the emplacement and evolution of zoned plutons: Geochronologic evidence for incremental assembly of the Tuolumne Intrusive Suite, California". In: *Geology* 32.5, pp. 433–436. ISSN: 00917613. DOI: 10.1130/G20220.1.

Connolly, J. A. D. (1990). "Multivariable phase diagrams; an algorithm based on generalized thermodynamics". In: *American Journal of Science* 290.6, pp. 666–718. DOI: 10.2475/ajs.290.6.666.

Connolly, JAD and DM Kerrick (2002). "Metamorphic controls on seismic velocity of subducted oceanic crust at 100–250 km depth". In: *Earth and Planetary Science Letters* 204.1-2, pp. 61–74.

Connolly, James A. D. (2005). "Computation of phase equilibria by linear programming: A tool for geodynamic modeling and its application to subduction zone decarbonation". In: *Earth and Planetary Science Letters* 236, pp. 524–541.

— (2017). "A primer in gibbs energy minimization for geophysicists". In: *Petrology* 25, pp. 526–534.

Crouzeix, M. and P.-A. Raviart (1973). "Conforming and nonconforming finite element methods for solving the stationary Stokes equations I". en. In: *Revue française d'automatique, informatique, recherche opérationnelle. Analyse numérique* 7.R3, pp. 33–75. URL: http://www.numdam.org/item/M2AN_1973__7_3_33_0/.

Dantzig, George B. (1963). *Linear programming and extensions*. Princeton, N.J.: Princeton University Press, pp. xvi+625.

D'Auria, Luca et al. (2022). "Rapid magma ascent beneath La Palma revealed by seismic tomography". In: *Scientific Reports* 12.1, pp. 1–13. ISSN: 20452322. DOI: 10.1038/s41598-022-21818-9. URL: https://doi.org/10.1038/s41598-022-21818-9.

de Capitani, Christian and Thomas H. Brown (1987). "The computation of chemical equilibrium in complex systems containing non-ideal solutions". In: *Geochimica et*

Cosmochimica Acta 51.10, pp. 2639–2652. ISSN: 0016-7037. DOI: https://doi.org/10.1016/0016-7037(87)90145-1.

De Siena, L., C. Thomas, G. P. Waite, S. C. Moran, and S. Klemme (2014). "Attenuation and scattering tomography of the deep plumbing system of Mount St. Helens". In: *Journal of Geophysical Research: Solid Earth* 119.11, pp. 8223–8238. ISSN: 21699356. DOI: 10.1002/2014JB011372.

Duretz, Thibault, René Borst, and Philippe Yamato (2021). "Modeling Lithospheric Deformation Using a Compressible Visco-Elasto-Viscoplastic Rheology and the Effective Viscosity Approach". In: *Geochemistry, Geophysics, Geosystems* 22.8, pp. 1–28. ISSN: 1525-2027. DOI: 10.1029/2021gc009675.

Duretz, Thibault, René de Borst, and Laetitia Le Pourhiet (2019). "Finite Thickness of Shear Bands in Frictional Viscoplasticity and Implications for Lithosphere Dynamics". In: *Geochemistry, Geophysics, Geosystems* 20.11, pp. 5598–5616. ISSN: 15252027. DOI: 10.1029/2019GC008531.

Duretz, Thibault, René de Borst, Philippe Yamato, and Laetitia Le Pourhiet (2020). "Toward Robust and Predictive Geodynamic Modeling: The Way Forward in Frictional Plasticity". In: *Geophysical Research Letters* 47.5, pp. 1–9. ISSN: 19448007. DOI: 10.1029/2019GL086027.

Duretz, Thibault, Ludovic Räss, René de Borst, and Tim Hageman (2023). "A Comparison of Plasticity Regularization Approaches for Geodynamic Modeling". In: *Geochemistry, Geophysics, Geosystems* 24.7, e2022GC010675. ISSN: 1525-2027. DOI: 10.1029/2022GC010675. URL: https://onlinelibrary.wiley.com/doi/full/10.1029/2022GC010675%0Ahttps://onlinelibrary.wiley.com/doi/abs/10.1029/2022GC010675%0Ahttps://agupubs.onlinelibrary.wiley.com/doi/10.1029/2022GC010675.

Duvaut, G. and J. L. Lions (1972). "Inéquations en thermoélasticité et magnétohydrodynamique". In: *Archive for Rational Mechanics and Analysis* 46.4, pp. 241–279. ISSN: 1432-0673. DOI: 10.1007/BF00250512. URL: https://doi.org/10.1007/BF00250512.

Fateen, Seif-Eddeen K. (2016). "Unconstrained Gibbs Minimization for Solving Multireaction Chemical Equilibria Using a Stochastic Global Optimizer". In: *Comput. Appl. Eng. Educ.* 24.6, pp. 899–904. ISSN: 1061-3773. DOI: 10.1002/cae.21759.

Feppon, F., G. Allaire, and C. Dapogny (2020). "Null space gradient flows for constrained optimization with applications to shape optimization". In: *ESAIM: COCV* 26, p. 90. DOI: 10.1051/cocv/2020015.

Fresno, Carmen del et al. (2023). "Magmatic plumbing and dynamic evolution of the 2021 La Palma eruption". In: *Nature Communications* 14.1, pp. 1–11. ISSN: 20411723. DOI: 10.1038/s41467-023-35953-y.

Fullsack, Philippe (1995). "An arbitrary Lagrangian-Eulerian formulation for creeping flows and its application in tectonic models". In: *Geophysical Journal International* 120.1, pp. 1–23. ISSN: 1365246X. DOI: 10.1111/j.1365-246X.1995.tb05908.x.

Gale, Allison, Colleen A. Dalton, Charles H. Langmuir, Yongjun Su, and Jean-Guy Schilling (2013). "The mean composition of ocean ridge basalts". In: *Geochemistry, Geophysics, Geosystems* 14.3, pp. 489–518. DOI: https://doi.org/10.1029/2012GC004334.

Ganguly, Jibamitra (2001). "Thermodynamic modelling of solid solutions". In: *EMU Notes in Mineralogy* 3.3, pp. 37–69.

Gasparik, Tibor (2014). "System CaO–MgO–SiO 2". In: *Phase Diagrams for Geoscientists*. Springer, pp. 81–129.

Gerya, Taras (2019). *Introduction to Numerical Geodynamic Modelling*. 2nd ed. Cambridge University Press. DOI: 10.1017/9781316534243.

Ghiorso, M. S. and Richard O. Sack (1995). "Chemical mass transfer in magmatic processes IV. A revised and internally consistent thermodynamic model for the interpolation and extrapolation of liquid-solid equilibria in magmatic systems at elevated temperatures and pressures". Undetermined. In: *Contributions to Mineralogy and Petrology* 119.2/3, pp. 197–212.

Ghiorso, Mark S. (1983). "LSEQIEQ: a FORTRAN IV subroutine package for the analysis of multiple linear regression problems with possibly deficient pseudorank and linear equality and inequality constraints". In: *Computers & Geosciences* 9, pp. 391–416.

— (1985). "Chemical mass transfer in magmatic processes". In: *Contributions to Mineralogy and Petrology* 90, pp. 107–120.

Gibbs, Josiah Willard (1878). "On the equilibrium of heterogeneous substances". In: *American Journal of Science* 3.96, pp. 441–458.

Green, E. C. R., R. W. White, J. F. A. Diener, R. Powell, T. J. B. Holland, and R. M. Palin (2016). "Activity–composition relations for the calculation of partial melting equilibria in metabasic rocks". In: *Journal of Metamorphic Geology* 34.9, pp. 845–869. DOI: https://doi.org/10.1111/jmg.12211.

Gregg, P. M., S. L. De Silva, E. B. Grosfils, and J. P. Parmigiani (2012). "Catastrophic caldera-forming eruptions: Thermomechanics and implications for eruption triggering and maximum caldera dimensions on Earth". In: *Journal of Volcanology and Geothermal Research* 241-242, pp. 1–12. ISSN: 03770273. DOI: 10.1016/j.jvolgeores.2012.06.009.

Gregg, Patricia M., Eric B. Grosfils, and Shanaka L. de Silva (2015). "Catastrophic caldera-forming eruptions II: The subordinate role of magma buoyancy as an eruption trigger". In: *Journal of Volcanology and Geothermal Research* 305, pp. 100–113. ISSN: 03770273. DOI: 10.1016/j.jvolgeores.2015.09.022.

Heeres, Otto M., Akke S.J. Suiker, and René De Borst (2002). "A comparison between the Perzyna viscoplastic model and the consistency viscoplastic model". In: *European Journal of Mechanics, A/Solids* 21.1, pp. 1–12. ISSN: 09977538. DOI: 10.1016/S0997-7538(01)01188-3.

Helffrich, George (1996). "Subducted lithospheric slab velocity structure: Observations and mineralogical inferences". In: *Washington DC American Geophysical Union Geophysical Monograph Series* 96, pp. 215–222.

Helgeson, Harold C (1978). "Summary and critique of the thermodynamic properties of rock-forming minerals". In: *American Journal of Science* 278, pp. 1–229.

Hildreth, Wes (Sept. 2004). "Volcanological perspectives on Long Valley, Mammoth Mountain, and Mono Craters: Several contiguous but discrete systems". In: *Journal of Volcanology and Geothermal Research* 136 (3-4), pp. 169–198. ISSN: 03770273. DOI: 10.1016/j.jvolgeores.2004.05.019.

Hildreth, Wes and Colin J.N. Wilson (2007). "Compositional zoning of the bishop tuff". In: *Journal of Petrology* 48.5, pp. 951–999. ISSN: 00223530. DOI: 10.1093/petrology/egm007.

Hirschmann, Marc M., Tetsu Kogiso, Michael B. Baker, and Edward M. Stolper (June 2003). "Alkalic magmas generated by partial melting of garnet pyroxenite". In: *Geology* 31.6, pp. 481–484. ISSN: 0091-7613. DOI: 10.1130/0091-7613(2003)031<0481:AMGBPM>2.0.CO;2.

Holland, T. J. B., E. C. R. Green, and R. Powell (2018). "Melting of peridotites through to granites: a simple thermodynamic model in the system KNCFMASHTOCr". In: *Journal of Petrology* 59.5, pp. 881–900.

Holland, T. J. B. and R. Powell (1998). "An internally consistent thermodynamic data set for phases of petrological interest". In: *Journal of Metamorphic Geology* 16.3, pp. 309–343. DOI: https://doi.org/10.1111/j.1525-1314.1998.00140.x.

Holland, Tim and Roger Powell (2003). "Activity–composition relations for phases in petrological calculations: an asymmetric multicomponent formulation". In: *Contributions to Mineralogy and Petrology* 145.4, pp. 492–501.

Holland, Tim J. B., Eleanor C. R. Green, and Roger Powell (2021). "A thermodynamic model for feldspars in KAlSi3O8-NaAlSi3O8-CaAl2Si2O8 for mineral equilibrium calculations". In: *Journal of Metamorphic Geology* n/a.n/a. DOI: https://doi.org/10.1111/jmg.12639.

Holland, TJB and R Powell (2011). "An improved and extended internally consistent thermodynamic dataset for phases of petrological interest, involving a new equation of state for solids". In: *Journal of metamorphic Geology* 29.3, pp. 333–383.

Hou, Tong, Roman Botcharnikov, Evangelos Moulas, Tobias Just, Jasper Berndt, Jürgen Koepke, Zhaochong Zhang, Meng Wang, Zongpeng Yang, and François Holtz (Jan. 2021). "Kinetics of Fe–Ti Oxide Re-equilibration in Magmatic Systems: Implications for Thermo-oxybarometry". In: *Journal of Petrology* 61.11-12. egaa116. ISSN: 0022-3530. DOI: 10.1093/petrology/egaa116.

Jacquey, Antoine B. and Mauro Cacace (2020a). "Multiphysics Modeling of a Brittle-Ductile Lithosphere: 1. Explicit Visco-Elasto-Plastic Formulation and Its Numerical Implementation". In: *Journal of Geophysical Research: Solid Earth* 125.1. ISSN: 21699356. DOI: 10.1029/2019JB018474.

— (2020b). "Multiphysics Modeling of a Brittle-Ductile Lithosphere: 2. Semi-brittle, Semi-ductile Deformation and Damage Rheology". In: *Journal of Geophysical Research: Solid Earth* 125.1. ISSN: 21699356. DOI: 10.1029/2019JB018475.

Jiang, Hua and Yongli Xie (2011). "A note on the Mohr-Coulomb and Drucker-Prager strength criteria". In: *Mechanics Research Communications* 38.4, pp. 309–314. ISSN: 00936413. DOI: 10.1016/j.mechrescom.2011.04.001.

Johnson, Steven G. (2021). *The NLopt nonlinear-optimization package*. Software. Version 2.7.2. DOI: 10.7283/633E-1497. URL: http://github.com/stevengj/nlopt.

Karki, Bijaya B, Lars Stixrude, and Renata M Wentzcovitch (2001). "High-pressure elastic properties of major materials of Earth's mantle from first principles". In: *Reviews of Geophysics* 39.4, pp. 507–534.

Katz, Richard F, David W Rees Jones, John F Rudge, and Tobias Keller (2022). "Physics of Melt Extraction from the Mantle: Speed and Style". In: *Annual Review of Earth and Planetary Sciences* 50.

Kaus, B. J. P., A. A. Popov, T. S. Baumann, A. E. Pusok, A. Bauville, N. Fernandez, and M. Collignon (2016). "Forward and Inverse Modelling of Lithospheric Deformation on Geological Timescales". In: *NIC Series* 48, pp. 978–3.

Kaus, Boris J.P. (2010). "Factors that control the angle of shear bands in geodynamic numerical models of brittle deformation". In: *Tectonophysics* 484.1-4, pp. 36–47. ISSN: 00401951. DOI: 10.1016/j.tecto.2009.08.042. URL: http://dx.doi.org/10.1016/j.tecto.2009.08.042.

Keller, Tobias and Richard F. Katz (2016). "The Role of Volatiles in Reactive Melt Transport in the Asthenosphere". In: *Journal of Petrology* 57.6, pp. 1073–1108. ISSN: 0022-3530. DOI: 10.1093/petrology/egw030.

Keller, Tobias, Richard F Katz, and Marc M Hirschmann (2017). "Volatiles beneath mid-ocean ridges: Deep melting, channelised transport, focusing, and metasomatism". In: *Earth and Planetary Science Letters* 464, pp. 55–68.

Keller, Tobias, Dave A. May, and Boris J.P. Kaus (2013). "Numerical modelling of magma dynamics coupled to tectonic deformation of lithosphere and crust". In: *Geophysical Journal International* 195.3, pp. 1406–1442. ISSN: 0956540X. DOI: 10.1093/gji/ggt306.

Keller, Tobias and Jenny Suckale (2019). "A continuum model of multi-phase reactive transport in igneous systems". In: *Geophysical Journal International* 219.1, pp. 185–222. ISSN: 0956-540X. DOI: 10.1093/gji/ggz287.

Kennedy, Ben M., A. Mark Jellinek, and John Stix (2008). "Coupled caldera subsidence and stirring inferred from analogue models". In: *Nature Geoscience* 1.6, pp. 385–389. ISSN: 17520894. DOI: 10.1038/ngeo206.

Khan, Kamil A. and Paul I. Barton (2015). "A vector forward mode of automatic differentiation for generalized derivative evaluation". In: *Optimization Methods and Software* 30.6, pp. 1185–1212. ISSN: 10294937. DOI: 10.1080/10556788.2015.1025400.

Kiss, D., E. Moulas, B. J.P. Kaus, and A. Spang (2023). "Decompression and Fracturing Caused by Magmatically Induced Thermal Stresses". In: *Journal of Geophysical Research: Solid Earth* 128.3, pp. 1–25. ISSN: 21699356. DOI: 10.1029/2022JB025341.

Kloeckner, Andreas et al. (Nov. 2022). *MeshPy*. Version 2022.1.1. DOI: 10.5281/zenodo.7296572. URL: https://github.com/inducer/meshpy.

Klügel, Andreas, Thor H. Hansteen, and Karsten Galipp (2005). "Magma storage and underplating beneath Cumbre Vieja volcano, La Palma (Canary Islands)". In: *Earth and Planetary Science Letters* 236.1-2, pp. 211–226. ISSN: 0012821X. DOI: 10.1016/j.epsl.2005.04.006.

Klügel, Andreas, Kaj A. Hoernle, Hans-Ulrich Schmincke, and James D. L. White (2000). "The chemically zoned 1949 eruption on La Palma (Canary Islands): Petrologic evolution and magma supply dynamics of a rift zone eruption". In: 105, pp. 5997–6016.

Kruskopf, Ari and Ville-Valtteri Visuri (2017). "A Gibbs Energy Minimization Approach for Modeling of Chemical Reactions in a Basic Oxygen Furnace". In: *Metallurgical and Materials Transactions B* 48.6. ISSN: 1073-5615. DOI: 10.1007/S11663-017-1074-X.

Lade, P. V. and R. De Boer (1997). "The concept of effective stress for soil, concrete and rock". In: *Geotechnique* 47.1, pp. 61–78. ISSN: 00168505. DOI: 10.1680/geot.1997.47.1.61.

Lade, Poul V. and James M. Duncan (1975). "Elastoplastic Stress-Strain Theory for Cohesionless Soil". In: *ASCE J Geotech Eng Div* 101.10, pp. 1037–1053. ISSN: 01489062. DOI: 10.1016/0148-9062(76)90242-4.

Lanari, Pierre and Erik Duesterhoeft (Nov. 2018). "Modeling Metamorphic Rocks Using Equilibrium Thermodynamics and Internally Consistent Databases: Past Achievements, Problems and Perspectives". In: *Journal of Petrology* 60.1, pp. 19–56. ISSN: 0022-3530. DOI: 10.1093/petrology/egy105.

Lasaga, Antonio C. (1986). "Metamorphic reaction rate laws and development of isograds". In: *Mineralogical Magazine* 50.357, pp. 359–373. DOI: 10.1180/minmag.1986.050.357.02.

Lees, Jonathan M. (2007). "Seismic tomography of magmatic systems". In: *Journal of Volcanology and Geothermal Research* 167.1-4, pp. 37–56. ISSN: 03770273. DOI: 10.1016/j.jvolgeores.2007.06.008.

Li, Yuan, Adina E Pusok, Timothy Davis, Dave A May, and Richard F Katz (2023). "Continuum approximation of dyking with a theory for poro-viscoelastic–viscoplastic deformation". In: *Geophysical Journal International* 234.3, pp. 2007–2031. ISSN: 1365246X. DOI: 10.1093/gji/ggad173.

Lothenbach, Barbara, Dmitrii A. Kulik, Thomas Matschei, Magdalena Balonis, Luis Baquerizo, Belay Dilnesa, George D. Miron, and Rupert J. Myers (2019). "Cemdata18: A chemical thermodynamic database for hydrated Portland cements and

alkali-activated materials". In: *Cement and Concrete Research* 115, pp. 472–506. ISSN: 0008-8846. DOI: https://doi.org/10.1016/j.cemconres.2018.04.018.

Maccaferri, F., M. Bonafede, and Eleonora Rivalta (2011). "A quantitative study of the mechanisms governing dike propagation, dike arrest and sill formation". en. In: *Journal of Volcanology and Geothermal Research* 208.1-2, pp. 39–50. ISSN: 03770273. DOI: 10.1016/j.jvolgeores.2011.09.001. URL: http://linkinghub.elsevier.com/retrieve/pii/S037702731100237X.

Maccaferri, Francesco, Eleonora Rivalta, Derek Keir, and Valerio Acocella (2014). "Off-rift volcanism in rift zones determined by crustal unloading". English. In: *Nature Geoscience* 7.4, pp. 297–300. ISSN: 1752-0894. DOI: 10.1038/ngeo2110.

Mantiloni, L., E. Rivalta, and T. Davis (2023). "Mechanical Modeling of Pre-Eruptive Magma Propagation Scenarios at Calderas". In: *Journal of Geophysical Research: Solid Earth* 128.3. ISSN: 21699356. DOI: 10.1029/2022JB025956.

Mark Jellinek, A. and D. DePaolo (2003). "A model for the origin of large silicic magma chambers: precursors of caldera-forming eruptions". In: *Bulletin of Volcanology* 65.5, pp. 363–381. ISSN: 0258-8900, 1432-0819. DOI: 10.1007/s00445-003-0277-y. URL: http://link.springer.com/10.1007/s00445-003-0277-y.

Menand, Thierry (2011). "Physical controls and depth of emplacement of igneous bodies: A review". In: *Tectonophysics* 500.1-4, pp. 11–19. ISSN: 00401951. DOI: 10.1016/j.tecto.2009.10.016. URL: http://dx.doi.org/10.1016/j.tecto.2009.10.016.

Michel, Jürgen, Lukas Baumgartner, Benita Putlitz, Urs Schaltegger, and Maria Ovtcharova (2008). "Incremental growth of the Patagonian Torres del Paine laccolith over 90 k.y". In: *Geology* 36.6, pp. 459–462. ISSN: 00917613. DOI: 10.1130/G24546A.1.

Murrell, S A F (1964a). "The theory of the propagation of elliptical Griffith cracks under various conditions of plane strain or plane stress: Parts II and III". In: *British Journal of Applied Physics* 15.10, p. 1211. DOI: 10.1088/0508-3443/15/10/309. URL: https://dx.doi.org/10.1088/0508-3443/15/10/309.

Murrell, S. A.F. (1964b). "The theory of the propagation of elliptical Griffith cracks under various conditions of plane strain or plane stress: Part I". In: *British Journal of Applied Physics* 15.10, pp. 1195–1210. ISSN: 05083443. DOI: 10.1088/0508-3443/15/10/308.

Myhill, Robert and James AD Connolly (2021). "Notes on the creation and manipulation of solid solution models". In: *Contributions to Mineralogy and Petrology* 176.10, pp. 1–19.

Novoa, C. et al. (2022). "The 2011 Cordón Caulle eruption triggered by slip on the Liquiñe-Ofqui fault system". In: *Earth and Planetary Science Letters* 583, p. 117386. ISSN: 0012-821X. DOI: https://doi.org/10.1016/j.epsl.2022.117386. URL: https://www.sciencedirect.com/science/article/pii/S0012821X22000022X.

Papale, Paolo, Chiara P. Montagna, and Antonella Longo (2017). "Pressure evolution in shallow magma chambers upon buoyancy-driven replenishment". In: *Geochemistry Geophysics Geosystems* 18.3, pp. 1214–1224. DOI: 10.1002/2016GC006731.Received.

Pauken, Mike (2011). *Thermodynamics for dummies*. John Wiley & Sons.

Perić, Dunja (2006). "Analytical solutions for a three-invariant Cam clay model subjected to drained loading histories". In: *International Journal for Numerical and Analytical Methods in Geomechanics* 30.5, pp. 363–387. ISSN: 03639061. DOI: 10.1002/nag.482.

Perzyna, Piotr (1966). "Fundamental Problems in Viscoplasticity". In: *Advances in Applied Mechanics* 9.C, pp. 243–377. ISSN: 00652156. DOI: 10.1016/S0065-2156(08)70009-7.

Piccolo, Andrea, Richard M. Palin, Boris J.P. Kaus, and Richard W. White (2019). "Generation of Earth's Early Continents From a Relatively Cool Archean Mantle". In: *Geochemistry, Geophysics, Geosystems* 20.4, pp. 1679–1697. ISSN: 15252027. DOI: 10.1029/2018GC008079.

Piro, M. H. A., S. Simunovic, T. M. Besmann, B. J. Lewis, and W. T. Thompson (2013a). "The thermochemistry library Thermochimica". In: *Computational Materials Science* 67. ISSN: 0927-0256.

Piro, Markus Hans Alexander (Jan. 2011). "Computation of Thermodynamic Equilibria Pertinent to Nuclear Materials in Multi-Physics Codes". PhD thesis. Royal Military College of Canada (Canada).

Piro, M.H.A., J. Banfield, K.T. Clarno, S. Simunovic, T.M. Besmann, B.J. Lewis, and W.T. Thompson (2013b). "Coupled thermochemical, isotopic evolution and heat transfer simulations in highly irradiated UO2 nuclear fuel". In: *Journal of Nuclear Materials* 441.1, pp. 240–251. ISSN: 0022-3115. DOI: https://doi.org/10.1016/j.jnucmat.2013.05.060.

Piro, M.H.A. and S. Simunovic (2016). "Global optimization algorithms to compute thermodynamic equilibria in large complex systems with performance considerations". In: *Computational Materials Science* 118, pp. 87–96. ISSN: 0927-0256. DOI: https://doi.org/10.1016/j.commatsci.2016.02.043.

Piwinskii, A. J. (1968). "Experimental Studies of Igneous Rock Series Central Sierra Nevada Batholith, California". In: *The Journal of Geology* 76.5, pp. 548–570. DOI: 10.1086/627359.

Pons, Michaël, Stephan V. Sobolev, Sibiao Liu, and Derek Neuharth (2022). "Hindered Trench Migration Due To Slab Steepening Controls the Formation of the Central Andes". In: *Journal of Geophysical Research: Solid Earth* 127.12, pp. 1–21. ISSN: 21699356. DOI: 10.1029/2022JB025229.

Popov, A. A. and S. V. Sobolev (2008). "SLIM3D: A tool for three-dimensional thermomechanical modeling of lithospheric deformation with elasto-visco-plastic rheology". In: *Physics of the Earth and Planetary Interiors* 171.1-4, pp. 55–75. ISSN: 00319201. DOI: 10.1016/j.pepi.2008.03.007.

Powell, Roger (1978). *Equilibrium thermodynamics in petrology: an introduction*. Harper & Row.

Powell, Roger and Tim Holland (1993). "On the formulation of simple mixing models for complex phases". In: *American Mineralogist* 78.11-12, pp. 1174–1180.

Powell, Roger and TJB Holland (1988). "An internally consistent dataset with uncertainties and correlations: 3. Applications to geobarometry, worked examples and a computer program". In: *Journal of metamorphic Geology* 6.2, pp. 173–204.

Räss, Ludovic, Ivan Utkin, Thibault Duretz, Samuel Omlin, and Yuri Y. Podladchikov (2022). "Assessing the robustness and scalability of the accelerated pseudo-transient method". In: *Geoscientific Model Development* 15.14, pp. 5757–5786. ISSN: 19919603. DOI: 10.5194/gmd-15-5757-2022.

Remacle, JF, J Lambrechts, and B Seny (2012). "Blossom-Quad: A non-uniform quadrilateral mesh generator using a minimum-cost perfect-matching algorithm". In: *International* February, pp. 1102–1119. DOI: 10.1002/nme. URL: http://onlinelibrary.wiley.com/doi/10.1002/nme.3279/full.

Revels, J., M. Lubin, and T. Papamarkou (2016). "Forward-Mode Automatic Differentiation in Julia". In: *arXiv:1607.07892 [cs.MS]*. URL: https://arxiv.org/abs/1607.07892.

Riel, Nicolas, João C. Duarte, Jaime Almeida, Boris J.P. Kaus, Filipe Rosas, Yamirka Rojas-Agramonte, and Anton Popov (2023). "Subduction initiation triggered the Caribbean large igneous province". In: *Nature Communications* 14.1. ISSN: 20411723. DOI: 10.1038/s41467-023-36419-x.

Rivalta, Eleonora, B. Taisne, A. P. Bunger, and R. F. Katz (2015). "A review of mechanical models of dike propagation: Schools of thought, results and future directions". en. In: *Tectonophysics* 638, pp. 1–42. ISSN: 00401951. DOI: 10.1016/j.tecto.2014.10.003. URL: http://linkinghub.elsevier.com/retrieve/pii/S0040195114005174.

Rozhko, Alexander Y., Y. Y. Podladchikov, and F. Renard (2007). "Failure patterns caused by localized rise in pore-fluid overpressure and effective strength of rocks". In: *Geophysical Research Letters* 34.22, pp. 1–5. ISSN: 00948276. DOI: 10.1029/2007GL031696.

Rubin, Allan M (1995). "Propagation of magma-filled cracks". In: Annual Review Earth and Planetary Sciences.23, pp. 287–336.

Rummel, Lisa, Boris J P Kaus, Tobias S Baumann, Richard W White, and Nicolas Riel (2020). "Insights into the Compositional Evolution of Crustal Magmatic Systems from Coupled Petrological-Geodynamical Models". In: *Journal of Petrology* 61.2. ISSN: 0022-3530. DOI: 10.1093/petrology/egaa029.

Ruz-Ginouves, Javiera, Muriel Gerbault, José Cembrano, Pablo Iturrieta, Felipe Sáez Leiva, Camila Novoa, and Riad Hassani (2021). "The interplay of a fault zone and a volcanic reservoir from 3D elasto-plastic models: Rheological conditions for mutual trigger based on a field case from the Andean Southern Volcanic Zone".

In: *Journal of Volcanology and Geothermal Research* 418, p. 107317. ISSN: 0377-0273. DOI: https://doi.org/10.1016/j.jvolgeores.2021.107317. URL: https://www.sciencedirect.com/science/article/pii/S0377027321001463.

Schmitt, A K, J Sliwinski, L Caricchi, O Bachmann, N Riel, B J P Kaus, A Cisneros De Léon, J Cornet, B Friedrichs, and O Lovera (2023). "Zircon age spectra to quantify magma evolution". In: *Geosphere* 19.4, pp. 1006–1031.

Shewchuk, Jonathan Richard (May 1996). "Triangle: Engineering a 2D Quality Mesh Generator and Delaunay Triangulator". In: *Applied Computational Geometry: Towards Geometric Engineering*. Ed. by Ming C. Lin and Dinesh Manocha. Vol. 1148. Lecture Notes in Computer Science. From the First ACM Workshop on Applied Computational Geometry. Springer-Verlag, pp. 203–222.

Sinogeikin, Stanislav V, Frank R Schilling, and Jay D Bass (2000). "Single crystal elasticity of lawsonite". In: *American Mineralogist* 85.11-12, pp. 1834–1837.

Sparks, R. Stephen J. and Katharine V. Cashman (2017). "Dynamic magma systems: Implications for forecasting volcanic activity". In: *Elements* 13.1, pp. 35–40. ISSN: 18115217. DOI: 10.2113/gselements.13.1.35.

Spear, Frank S. (1988). "The Gibbs method and Duhem's theorem: The quantitative relationships among P, T, chemical potential, phase composition and reaction progress in igneous and metamorphic systems". In: *Contributions to Mineralogy and Petrology* 99.2, pp. 249–256. DOI: 10.1007/BF00371465.

Spear, Frank S (1993). "Metamorphic phase equilibria and pressure-temperature-time paths". In: *Mineralogical Society of America Monograph*, pp. 352–356.

Spiegelman, Marc, Dave A. May, and Cian R. Wilson (2016). "On the solvability of incompressible Stokes with viscoplastic rheologies in geodynamic". In: *Geochemistry Geophysics Geosystems* 17, pp. 2213–2238. DOI: 10.1002/2015GC006228.

Stixrude, Lars and Carolina Lithgow-Bertelloni (2011). "Thermodynamics of mantle minerals - II. Phase equilibria". In: *Geophysical Journal International* 184.3, pp. 1180–1213. ISSN: 0956-540X. DOI: 10.1111/j.1365-246X.2010.04890.x.

— (Sept. 2021). "Thermal expansivity, heat capacity and bulk modulus of the mantle". In: *Geophysical Journal International* 228.2, pp. 1119–1149. ISSN: 0956-540X. DOI: 10.1093/gji/ggab394. URL: https://doi.org/10.1093/gji/ggab394.

Svanberg, Krister (2002). "A class of globally convergent optimization methods based on conservative convex separable approximations". In: *SIAM Journal on Optimization*, pp. 555–573.

Takahashi, Eiichi (1986). "Melting of a dry peridotite KLB-1 up to 14 GPa: Implications on the Origin of peridotitic upper mantle". In: *Journal of Geophysical Research: Solid Earth* 91.B9, pp. 9367–9382. DOI: https://doi.org/10.1029/JB091iB09p09367.

Taylor-West, Jesse and Richard F Katz (2015). "Melt-preferred orientation, anisotropic permeability and melt-band formation in a deforming, partially molten aggregate". In: *Geophysical Journal International* 203.2, pp. 1253–1262.

Teh, Y.S. and G.P. Rangaiah (2002). "A Study of Equation-Solving and Gibbs Free Energy Minimization Methods for Phase Equilibrium Calculations". In: *Chemical Engineering Research and Design* 80.7, pp. 745–759. ISSN: 0263-8762. DOI: https://doi.org/10.1205/026387602320776821.

Thielmann, M., B. J.P. Kaus, and A. A. Popov (2015). "Lithospheric stresses in Rayleigh-Bénard convection: Effects of a free surface and a viscoelastic Maxwell rheology". In: *Geophysical Journal International* 203.3, pp. 2200–2219. ISSN: 1365246X. DOI: 10.1093/gji/ggv436.

Tomlinson, Emma L and Tim JB Holland (2021). "A thermodynamic model for the subsolidus evolution and melting of peridotite". In: *Journal of Petrology* 62.1, egab012.

Turner, Andrew J, Richard F Katz, Mark D Behn, and Tobias Keller (2017). "Magmatic focusing to mid-ocean ridges: The role of grain-size variability and non-newtonian viscosity". In: *Geochemistry, Geophysics, Geosystems* 18.12, pp. 4342–4355.

Verdugo, Francesc and Santiago Badia (July 2022). "The software design of Gridap: A Finite Element package based on the Julia JIT compiler". In: *Computer Physics Communications* 276, p. 108341. DOI: 10.1016/j.cpc.2022.108341. URL: https://doi.org/10.1016/j.cpc.2022.108341.

Wang, Huan (2019). "Viscous and second gradient regularization techniques for the description of the behavior of geomaterials". PhD thesis. École centrale de Nantes.

Wang, W. M., L. J. Sluys, and R. De Borst (1997). "Viscoplasticity for instabilities due to strain softening and strain-rate softening". In: *International Journal for Numerical Methods in Engineering* 40.20, pp. 3839–3864. ISSN: 00295981. DOI: 10.1002/(SICI)1097-0207(19971030)40:20<3839::AID-NME245>3.0.CO;2-6.

White, R. W., R. Powell, T. J. B. Holland, T. E. Johnson, and E. C. R. Green (2014). "New mineral activity–composition relations for thermodynamic calculations in metapelitic systems". In: *Journal of Metamorphic Geology* 32.3, pp. 261–286. DOI: https://doi.org/10.1111/jmg.12071.

White, W.B., Johnson S.M., and Dantzig G.B. (1958). "Chemical Equilibrium in Complex Mixtures". In: *Journal of Chemical Physics* 28, pp. 751–755.

Xiang, Hua and James A. D. Connolly (2021). "GeoPS: An interactive visual computing tool for thermodynamic modelling of phase equilibria". In: *Journal of Metamorphic Geology* n/a.n/a. DOI: https://doi.org/10.1111/jmg.12626.

Yang, Huai-Jen, Rosamond Joyce Kinzler, and Timothy L. Grove (1996). "Experiments and models of anhydrous, basaltic olivine-plagioclase-augite saturated melts from 0.001 to 10 kbar". In: *Contributions to Mineralogy and Petrology* 124, pp. 1–18.